Radar and Radar Imaging of Cooperative and Uncooperative Modulated Targets

Xiaojie Fu

A dissertation
submitted in partial fulfillment of the
requirements for the degree of

Doctor of Philosophy

University of Washington

2019

Reading Committee:

Matthew S. Reynolds, Chair

Joshua R. Smith

Pavel V. Nikitin

Arka Majumdar

Program Authorized to Offer Degree:
Department of Electrical & Computer Engineering

University of Washington

Abstract

Radar and Radar Imaging of Cooperative and Uncooperative Modulated Targets

Xiaojie Fu

Chair of the Supervisory Committee:
Associate Professor Matthew S. Reynolds
Electrical & Computer Engineering Department

Radar and radar imaging technologies are widely used in the exploration of: (1) cooperative modulated targets that intentionally change their reflectivity to backscatter encoded signals, (2) uncooperative modulated targets that unintentionally modulate radar signals due to micro-motions, and (3) unmodulated targets that only reflect but do not modulate radar signals. In this work, a general model is proposed to encompass all three types of targets. This model unmasks the system frequency response when a general modulated target is included in the channel. It treats this target as a group of hypothesized point scatterers that modulate the radar signal with time-variant reflection coefficient values and time-variant point scatterer distribution. Additionally, the model accounts for stationary or moving radar platforms. This allows backscatter signals from different targets to be modeled and processed using the same framework.

To use the model on cooperative targets, we first develop a low-cost X-band backscatter testbed and fabricate sensor tags used as cooperative targets. The system shows a good agreement between measured and simulated free-space path loss at up to 4.1 m and demonstrates a BPSK backscatter modulation at 10 Mbps. Then an extension of synthetic aperture radar (SAR) techniques is proposed to enable simultaneous imaging of reflective objects (unmodulated targets), sensor tag (cooperative target) localization, and backscatter data uplink from multiple tags in a cluttered environment. SAR measurements are implemented at $10 - 13$ GHz with unmodulated targets and two sensor tags that monitor temperature changes and encode data with balanced orthogonal SAR code words in each packet. The resulting point-spread functions (PSFs) of tags at ranges of 4.4 m and 4.7 m demonstrate a range resolution of 4.7 cm, a cross-range resolution of 9.1 cm, and a maximum localization error of 9 mm. In addition, 1-bounce multipath ghosts (from a large reflective plane) of the tags are predicted by using virtual point scatterers with a maximum error of 1.4 cm.

To apply the model on uncooperative targets, backscatter signal features of an off-the-shelf quadcopter UAV are extracted to characterize the reflectivity, static and dynamic radar cross sections, and the micro-

Doppler signatures of the quadcopter using a custom K-band (15 – 26.5 GHz) laboratory radar system. The exploration of micro-Doppler signatures includes interference analysis between multiple spinning propellers and Doppler spectra analysis based on controlled rotation rate measurements. The magnitude of Doppler frequencies and Doppler bandwidth differ, even for a fixed rotation rate, and depend on the propeller orientations relative to the radar unit. In the modeling of a single propeller, such differences are explained by correlations between the simulated backscatter signals and the measured receive signals in different orientations. With only twelve point scatterers modeling the propeller, several sets of reflection coefficient values are found to reconstruct the measurement results with a maximum root mean square (RMS) error of 8 dB across all harmonic components in the asymmetric upper and lower sidebands.

ACKNOWLEDGMENTS

Joining a Ph.D. program in a foreign country is the best decision I have ever made. It takes years of preparation and planning before starting, self-challenge and creativity during the application process, and perseverance and tenacity when completing the degree. I was fortunate and blessed to work, interact, and become friends with many people in this amazing journey.

First and foremost, I want to thank my advisor Prof. Matthew Reynolds. Matt, you won't believe how much my life has changed since we had the interview conversation during my campus visit on March 5, 2015. Thank you for always setting achievable goals on research, providing the simplest problem-solving instructions, understanding my difficulties, and supporting me under all conditions. Thank you more for all the advice on important career decisions and the grant money you secured for me and the rest of the lab. I have also learned so much from the way you build and manage our team, how you collaborate us with other teams on major government projects that are not normally seen in grad schools, how you demonstrate our work and bring visitors to the lab almost every week, and how fast you found a new start-up from only ideas. You are the best advisor, researcher, mentor, and team leader I could ever have imagined.

Thank you to everyone I have worked with in lab at the University of Washington - Dr. Daniel Arnitz, Dr. Andreas Pedross-Engel, Dr. Claire Watts, Eleftherios Kampianakis, Dr. Joshua Ensworth, James Rosenthal, Apoorva Sharma, Alexander Hoang, Dr. Kris Spaeth, Thang Phu, and Sandamali Devadithya. Thank you for forming a powerful team and creating a healthy and friendly work environment. I think that we did wonderful things together and I am excited for what the future holds for all of you. I would like to especially thank our post-docs Daniel, Andreas, and Claire for the direct help in my research projects. Thanks for bringing the high-level of sophistication to the lab. I am so lucky to work on all my projects with you. A special thanks to Lefteris for the hundreds of hours of constructive conversations, inviting me to your world, and carrying me through all my difficult times. And also, a huge thanks to Josh for all the help you offered in my research and job hunting.

Thank you to my professors, labmates, and friends in China. Especially, I want to thank my Master degree advisor Prof. Xiaoxing Yin for your care and support in every possible way. Thank you to Dr. Li Xie, founder of Harogic Inc., for helping me start in this area and inspiring me with all your expertise and high standards. Thank you to Dr. Xin Jiang, founder of Milliway Inc., and Dr. Xiong Wang at ShanghaiTech

University for sharing your oversea experiences. I would not have been admitted to UW without your help. Thank you to Tingting (Emma) Yuan at Huawei Inc. for being a sister to me. We met in grad school in China, and after so many years the long distance never stops us from caring for and supporting each other every day!

I would also like to express my gratitude to all the friends I made in Seattle and Bay Area - Dianmu Zhang, Fan Zhang, Dr. Tong Zhang, Aili Wang, Robin Walker, Sree Surendran, Mark Sun, Jinze Zheng, Qin Feng, Jin Liu, Tim Johnson, Nilay Jani, Rob Parnell, Dr. Xinhao Wang, Dr. Ben Peng, Dr. Vishal Gupta, Dr. Istvan Szini, Candace Zeng, Dr. Xiaoyu Wang, Dr. Weitian Sheng, Yue Guo and anyone I accidentally forgotten. I moved to this new country to pursue a Ph.D. without knowing anyone, thanks for becoming such important parts of my life.

Thank you to the members of my dissertation committee - Prof. Joshua Smith, Prof. Pavel Nikitin, Prof. Arka Majumdar, Prof. John Sahr and Prof. Sawyer Fuller. This work is better because of the insightful and helpful questions and comments from all of you.

Finally and most importantly, I would like to thank my mom and dad. Everything I am today is all for the sacrifices you made for me. Thanks for making lifelong efforts to ensure that I get the best in life. Thank you for not only being parents to me but also my best friends. I am sure life will be easier and we have a bright future ahead!

To my parents,

Hong Xu and Qingcheng Fu,

for their ever-present love and support.

TABLE OF CONTENTS

Page

List of Figures . . . iv

List of Tables . . . vii

Chapter 1: Introduction . . . 1
- 1.1 Basic Radar Principles . . . 1
- 1.2 Cooperative and Uncooperative Modulated Targets . . . 3
  - 1.2.1 Cooperative Modulated Targets . . . 4
  - 1.2.2 Uncooperative Modulated Targets . . . 5
- 1.3 Research Questions and Original Contributions . . . 7
- 1.4 Thesis Organization . . . 9
- 1.5 Publications . . . 10

Chapter 2: Microwave Backscatter Communication: A Typical Radar-Target Cooperation . . . 12
- 2.1 Introduction to Microwave Backscatter Communication . . . 13
- 2.2 Modulated Backscatter . . . 14
  - 2.2.1 Modulation Factor and Differential Radar Cross Section . . . 14
  - 2.2.2 Forward Link and Backscatter Link . . . 15
- 2.3 Design of a Low-Cost X-Band Backscatter Testbed and Cooperative Targets . . . 16
  - 2.3.1 Wideband Bow-tie Antenna . . . 18
  - 2.3.2 Transmitter Front-End . . . 20
  - 2.3.3 Receiver Front-End . . . 21
  - 2.3.4 Proof-of-Concept X-Band BPSK Tag . . . 22
- 2.4 System-Level Measurements . . . 23
  - 2.4.1 Simulated Free-Space Model and Measured Path Loss . . . 23
  - 2.4.2 X-Band BPSK Backscatter Communication at 10 Mbps . . . 25
- 2.5 Chapter Conclusion . . . 27

Chapter 3: Synthetic Aperture Radar (SAR) Imaging: an Application Based on Radar Motion . . . 28
- 3.1 Introduction to SAR Imaging Technology . . . 29
- 3.2 SAR Principles and Important Terminologies . . . 29
  - 3.2.1 Basic SAR Mechanism . . . 29
  - 3.2.2 Stripmap SAR and Spotlight SAR . . . 30

3.2.3 2-D and 3-D SAR Selection . . . 30
3.2.4 Range and Cross-Range Resolution . . . 31
3.3 SAR Image Reconstruction . . . 32
3.3.1 Adaption of the General Frequency Response Model . . . 32
3.3.2 Reconstruction and Computational Complexity . . . 33
3.4 Chapter Conclusion . . . 35

Chapter 4: Simultaneous SAR imaging, Localization, and Backscatter Uplink with Cooperative Modulated Targets . . . 36
4.1 Introduction and Related Work . . . 37
4.2 Model of Simultaneous Imaging, Localization, and Backscatter Uplink . . . 38
4.2.1 Single Tag Localization . . . 40
4.2.2 Simultaneous Multi-tag Localization . . . 41
4.2.3 Imaging of the Unmodulated Environment . . . 41
4.2.4 Imaging All Scattering Objects . . . 41
4.3 Indoor Measurements . . . 42
4.3.1 Sensor Tag Hardware . . . 42
4.3.2 Data Packet Structure and Multiple Access Encoding . . . 43
4.3.3 Measurement Setup and Implementation . . . 45
4.4 Phase Center Calibration for Imaging and Localization . . . 46
4.4.1 TX-RX Phase Center Correction . . . 46
4.4.2 Tag Phase Center Correction . . . 46
4.5 Imaging, Localization, and Backscatter Uplink Results . . . 48
4.5.1 Imaging Results . . . 48
4.5.2 Localization Results . . . 48
4.5.3 Backscatter Data Uplink Results . . . 50
4.6 Chapter Conclusion . . . 51

Chapter 5: Multipath Exploration in Simultaneous Radar Imaging and Cooperative Target Localization . . . 52
5.1 Introduction and Related Work . . . 53
5.2 Virtual Targets in Simultaneous Imaging and Cooperative Target Localiaztion . . . 54
5.2.1 Mirrored and Projected Point Scatterers . . . 54
5.2.2 Multipath Frequency Response . . . 55
5.2.3 Imaging and Localization of Virtual Modulated Targets . . . 56
5.3 Reconstruction of Virtual Targets in Simultaneous Imaging and Localization . . . 58
5.3.1 Measurement and Phase Center Correction . . . 58
5.3.2 Imaging Results . . . 58
5.3.3 Localization Results . . . 59
5.4 Chapter Conclusion . . . 61

Chapter 6: Quadcopter UAV: an Example of Uncooperative Modulated Targets 62
6.1 Overview on the Research of UAVs 63
6.1.1 Research Background 63
6.1.2 Prior Art 63
6.1.3 Quadcopter Hardware Selection and Characterization Methods 64
6.2 Quadcopter Characterized as an Unmodulated Target 67
6.2.1 Distribution of Point Scatterers in a Quadcopter Based on 3-D SAR Imaging 67
6.2.2 Radar Cross Section of a Quadcopter 70
6.3 Quadcopter Characterized as an Uncooperative Target 72
6.3.1 Implementation of K-Band Measurements in the Chamber 72
6.3.2 Micro-Doppler Signatures of Continuously Varying Rotating Rates 76
6.3.3 Micro-Doppler Signatures of Fixed Rotation Rates 77
6.4 Chapter Conclusion 83

Chapter 7: Micro-Doppler Signature of a Spinning Propeller Modeled with Point Scatterers . . . 84
7.1 The Modulation Nature of Micro-Doppler Signature 85
7.1.1 Amplitude Modulation and Angle Modulation by a Sinusoidal Signal 85
7.1.2 Modulation Induced by Micro-Motions 86
7.1.3 Two Special Cases of Rotation 88
7.2 The Nonuniform Distribution of Point Scatterers in a Single Propeller 89
7.3 The Modeling of Rotating Propellers 91
7.3.1 Selection of Point Scatterers 91
7.3.2 Simulation and Correlation to Measurement Results 92
7.4 Chapter Conclusion 97

Chapter 8: Conclusion and Future Work 98
8.1 Conclusion 98
8.2 Future Work 99
8.2.1 Massive-MIMO Imaging of Modulated Targets 99
8.2.2 Asymmetry in the Upper and Lower Doppler Sidebands 100

Bibliography 101

LIST OF FIGURES

Figure Number — Page

1.1 Basic monostatic radar systems with different targets. (a) A conventional radar system receives a scattered signal from a target that is moving at a constant speed; (b) a moving target has micro-motions (propeller rotations) in addition to its constant-speed body translation; (c) a radar system receives backscatter signals from a target that modulates the radar carrier signal with sensor data. 2

1.2 A cooperative phase modulated target with two modulation states: (a) block diagram of a backscatter tag; (b) impedance of two modulation states measured at antenna load termination; (c) sub-carriers in the received backscatter signal frequency spectrum when the switching frequency is fixed. 4

1.3 Example of an uncooperative target. (a) A propeller approaching the radar with a fixed motion speed and a fixed rotation rate. (b) The micro-Doppler time-frequency analysis. (c) The micro-Doppler frequency spectrum. 6

2.1 Relation between load impedance and reflection coefficient on the Smith Chart. 15

2.2 Schematics showing the relations between the power received and the power transmitted. (a) A radio wave from a transmitter directly incident on the receiver. (b) An unmodulated target or an uncooperative target scatters a signal from transmitter to the receiver. (c) A cooperative target backscatters an electromagnetic wave from the transmitter to the receiver. 17

2.3 Block diagram of the low-cost X-band backscatter testbed and a low-cost backscatter tag as an example of cooperative modulated targets. 18

2.4 Layouts of (a) TX component side, (b) antenna side of TX and RX, and (c) RX component side. 19

2.5 Photos of (a) transmitter PCB and holder, (b) receiver PCB and holder, and (c) BPSK backscatter tag. 19

2.6 Simulated and measured $|S_{11}|$ of the bow-tie antenna. 20

2.7 Simulated radiation pattern of bow-tie antenna. 20

2.8 Measured S_{11} of the X-Band tag from 10 to 11.1 GHz. 23

2.9 Backscatter power measurement setup: (a) photo (b) block diagram. 24

2.10 Friis model vs. measured backscatter power. 25

2.11 BPSK Backscatter communication setup. 26

2.12 Demodulated backscatter data vs. original data sequence in the tag (only a part of one data packet is shown). 26

2.13 Eye diagram of one packet demodulated data. 26

3.1 Basic operation schematics of 2-D SAR systems. (a) Stripmap SAR has a fixed antenna look angle α. (b) Spotlight SAR steers the antenna beam to constantly illuminate a single area. . . 30

3.2 Basic operation schematic of a 3-D SAR system. 31

3.3 SAR image reconstruction process. 34

4.1 Conceptual backscatter-based sensor system using a synthetic aperture radar for imaging, tag localization, and sensor data uplink. The Backscatter nodes are cooperative targets to the radar system, and the scattering objects are unmodulated targets. 37
4.2 Signal processing pipeline for simultaneous radar imaging, sensor tag localization, and backscatter uplink. 39
4.3 Schematic of the experimental SAR setup with two sensor tags. 42
4.4 The (a) front side, (b) back side, and (c) schematic of the sensor tag. 43
4.5 Measured reflection coefficients of the PIN switch over 10-11 GHz. 44
4.6 Format of the tag data packets showing sub-frames for SAR imaging, sensor data, and CRC. 44
4.7 Photo of (a) the imaging region of interest (ROI) and (b) the cluttered measurement environment. Sub-figure (c) shows the geometry of the imaging area and the linear stage motion. . . 45
4.8 Experimental setups and measured data used for calibration of TX-RX phase center and tag phase center. 47
4.9 SAR images reconstructed with different processing approaches, showing the ability to separate tags from each other and from the un-tagged scatterers. 49
4.10 Measured time series of room temperature (Tag 1) and coffee cup temperature (Tag 2). . . . 50

5.1 An example of first-order virtual point scatterers generated in an indoor SAR measurement. The three reflective walls create three mirrored and three projected point scatterers in addition to the one actual point scatterer. 54
5.2 Rerun the measurements in Chapter 4.3 with the same setup except that a large reflective plane is placed behind the Styrofoam. 59
5.3 (a) Imaging result showing all reflective objects and virtual tags. (b) Ground truth of the tags, nuts, and the reflective plane. Localization results show the actual, mirrored, and projected cooperative targets: (c) Tag 1 only; (d) Tag 2 only; (e) Tag 1 and Tag 2 together. 60

6.1 System Diagram of a typical quadcopter. 64
6.2 Turnigy SK450 quadcopter, with the original flight controller unit highlighted. 65
6.3 Top-view 3-D SAR imaging characterization of a quadcopter. The antennas look at the quadcopter in the pitch direction. 68
6.4 Edge-view 3-D SAR imaging characterization of a quadcopter. The antennas look at the quadcopter from the edges. 68
6.5 3-D SAR images of a Turnigy SK450 quadcopter (a) looking from the top and (b) looking from the edges. (c) and (d) show the mean reflectivity in range direction (averaging the absolute reflectivity values over $y = [0.582, 0.728]$ m for top-view characterization and over $y = [0.518, 0.938]$ m for edge-view characterization). All the reflectivity values are normalized to the maximum reflection of each configuration. Different scales are used in different figures for clearly showing the profile and detail structures. *Courtesy of Dr. Claire M. Watts at University of Washington.* 69
6.6 Mean RCS of a Turnigy SK450 quadcopter over 15 – 26.5 GHz when the radar looks at the quadcopter from the (a) top and (b) edges. 71
6.7 Schematic of the hardware connections in the micro-Doppler measurements. The custom-designed flight controller unit uses WiFi to interface with the computer. 73

6.8 A photo of the custom-designed K-band radar front-end. 74
6.9 A photo of the custom-designed flight controller unit mounted on the quadcopter. 74
6.10 K-band micro-Doppler measurements in the chamber. (a) A schematic of the chamber measurement setup. (b) A Photo showing the measurement environment. 75
6.11 Spectrograms of the radar received signals. By using the stock remote control to continuously vary the rotation rate of all propellers, the maximum rotation rate at which the quadcopter can handle is found at 6500 rpm (corresponding to 108 Hz in the spectrogram). (a) Throttle varied from idle to max for four time in 40s. (b) Constant Throttle level over 40s. 76
6.12 The Doppler power spectrum of dynamic radar cross sections measured with a radar carrier signal at 20 GHz when all four propellers are set to rotate at a rate of 4200 rpm. 78
6.13 Dynamic RCS results in top-view configuration (rotation rate is approximately 5000 rpm): (a) displays two micro-Doppler power spectra of the two propellers when they are measured separately; (c) is the power spectrum when the two propellers are rotating simultaneously. Dynamic RCS results in edge-view configuration (rotation rate is approximately 5100 rpm): (b) separate rotations; (d) simultaneous rotation. 79
6.14 The Doppler power spectra of dynamic radar cross sections measured with a radar carrier signal at 20 GHz when one propeller is rotating in top-view configuration at a rate of (a) 3000 rpm; (b) 5000 rpm; (c) 6500 rpm. 81
6.15 The Doppler power spectra of dynamic radar cross sections measured with a radar carrier signal at 20 GHz when one propeller is rotating in edge-view configuration at a rate of (a) 3000 rpm; (b) 5000 rpm; (c) 6500 rpm. 82
7.1 A point scatterer rotating about an axis in direction of $\hat{\mathbf{n}}$. 87
7.2 Two special cases of rotating point scatterers. In both cases, the rotation centers are stationary and fixed to the same height as the antenna center. (a) The rotation plane is vertical to the ground and parallel to the antenna aperture. (b) The rotation is in a horizontal plane. . . . 88
7.3 (a) The composition of a 8045R CCW propeller. (b) An image of the CCW propeller extracted from the top-view image of the quadcopter. (c) The CCW propeller is placed in a horizontal plane with face side directing upward. The photo is taken from the viewpoint of antenna. (d) A SAR image of the CCW propeller in edge-view configuration when face side is upward. (e) The CCW propeller is placed with the back side directing upward. (f) A SAR image of the upside down propeller. *Courtesy of Dr. Claire M. Watts at University of Washington.* 90
7.4 The point scatterers selected to represent the CCW propeller. 91
7.5 Re-plot the dynamic RCS results of one spinning propeller in top-view configuration to just show the harmonic Doppler frequencies. The rotation rates are: (a) 3000 rpm; (b) 5000 rpm; and (c) 6500 rpm. Both side bands are zoomed to 8 kHz to show the significant spectral lines at harmonic Doppler frequencies. 93
7.6 A comparison between simulated and measured dynamic RCS results of one propeller in top-view configuration when the rotation rates are: (a) 3000 rpm; (b) 5000 rpm; and (c) 6500 rpm. 94
7.7 Re-plot the dynamic RCS results of one spinning propeller in edge-view configuration to just show the harmonic Doppler frequencies. The rotation rates are: (a) 3000 rpm; (b) 5000 rpm; and (c) 6500 rpm. 95
7.8 A comparison between simulated and measured dynamic RCS results of one propeller in edge-view configuration when the rotation rates are: (a) 3000 rpm; (b) 5000 rpm; and (c) 6500 rpm. 96

LIST OF TABLES

Table Number Page

2.1 Measured TX front-end Performance 21
2.2 Measured RX front-end performance 22

4.1 Comparison of measurement results with the ground truths 50

5.1 Comparison of reconstructed virtual targets with their predicted positions 59

6.1 Characterization measurements of the quadcopter 66
6.2 Ratio of the backscatter signal power from different components in the quadcopter 70
6.3 Typical radar cross section values 72

7.1 Starting angle, radius, and reflectivity magnitude of each point scatterer in one simulation run 92

Chapter 1
INTRODUCTION

1.1 Basic Radar Principles

Radar is an electromagnetic system for the detection and ranging of reflective objects such as aircraft, ships, vehicles, people, and the natural environment. And the reflective objects are referred as **targets**. By radiating a radio-frequency (RF) or microwave signal into space and processing the echoed signal from targets, a radar system can determine the presence of targets and their locations based on signal strength, phase delay, time of arrival, and etc [1]. It augments optical systems by overcoming the limitations to measure long ranges in adverse weather.

A radar system using a same antenna for both transmit and receive is a monostatic radar. While a system using two separate antennas for transmit and receive is a bistatic radar system [2]. The basic operation principles of a monostatic radar are shown in Fig. 1.1 with three different type of targets. The transmitter (TX) generates a transmit signal $s(t)$, amplifies, and radiates it into space through an antenna. Then the receiver (RX) fetches the backscatter signal $r(t)$ from the field, downconverts, and processes the signal to extract certain features of targets. The time domain and frequency domain expressions of the received signal can be written as

$$\begin{aligned} r(t) &= s(t) * h(t) \\ R(e^{j\omega}) &= S(e^{j\omega}) H(e^{j\omega}) \end{aligned}, \tag{1.1}$$

where $h(t)$ and $H(e^{j\omega})$ are the **impulse response** and the **frequency response** of the system.

One important concept in radar technologies is range. If it takes the radar signal a time of τ to travel to the target and return back to the radar, then the range R of the target can be calculated as

$$R = \frac{c_0 \tau}{2}, \tag{1.2}$$

where c_0 is the speed of light.

If the target is moving as illustrated in Fig. 1.1a, it also induces a frequency shift to the backscatter signal due to the **Doppler effect**. This feature is widely used in radar technologies to separate moving targets from the stationary environment that has an unchanging backscatter response. The Doppler frequency f_{D}, proportional to the target radial speed v_{radial}, can be calculated with

$$f_{\mathrm{D}} = \frac{-2 v_{\text{radial}}}{c_0} f_{\mathrm{c}}, \tag{1.3}$$

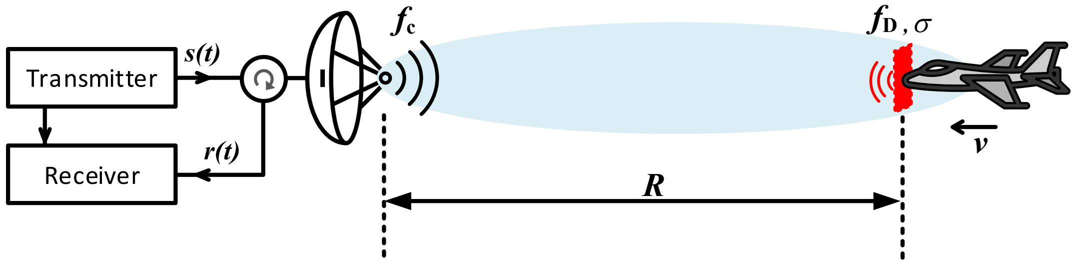

(a)

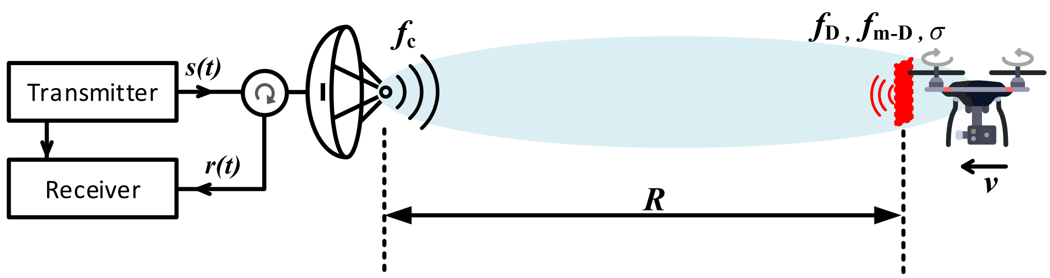

(b)

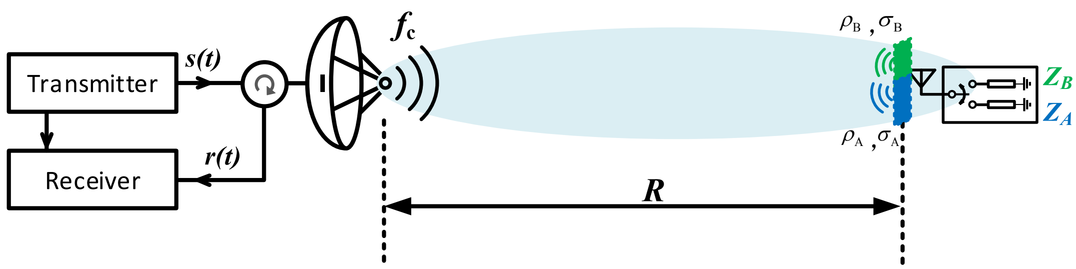

(c)

Figure 1.1: Basic monostatic radar systems with different targets. (a) A conventional radar system receives a scattered signal from a target that is moving at a constant speed; (b) a moving target has micro-motions (propeller rotations) in addition to its constant-speed body translation; (c) a radar system receives backscatter signals from a target that modulates the radar carrier signal with sensor data.

where f_c is the radio carrier frequency.

When the transmitting electromagnetic wave is incident on the target, only a portion of the propagating wave is intercepted and reflected by the target depending on the antenna beam direction, beam width, and the size of targets. It looks to the radar systems that each target has an effective reflective area which is a scalar indicator of the target's ability to reflect electromagnetic energy. This effective reflective area is defined as radar cross section σ and can be seen as a projected cross section of the target that is left on the antenna radiation beam.

The intercepted wave is then scattered back to the field in many directions. Due to the diffraction and scattering of other objects in the environment, the backscatter signal may reach the receiver through a countless number of paths. This multi-path propagation can cause constructive or destructive interference to the direct or line of sight (LOS) backscatter signal. At microwave frequencies, it is usually more convenient to extract signal features and characterize electrical properties of the target using system frequency response. To derive the frequency response of system shown in Fig. 1.1a, we assume the target consists of M hypothesized, constant reflective point scatterers, and the radar frequency response at angular frequency ω_l (or frequency f_l) can be represented as

$$\begin{aligned} y_l = H(e^{j\omega_l}) &= \overbrace{\sum_{m=1}^{M} \tilde{\rho}_m \tilde{\alpha}_{l,m}^2 e^{-j2\pi f_l \frac{2\left\|\overrightarrow{\mathbf{R}}+\overrightarrow{\mathbf{r}_m}\right\|}{c_0}}}^{\text{target scatterer response}} + \text{Multipath} + \nu_l, \\ \tilde{\alpha}_{l,m} &\propto \frac{1}{\left\|\overrightarrow{\mathbf{R}}+\overrightarrow{\mathbf{r}_m}\right\|} \end{aligned} \tag{1.4}$$

where $\tilde{\rho}_m$ is the complex reflection coefficient of the m-th point scatterer in the target, $\tilde{\alpha}_{l,m}$, including one-way LOS path loss and antenna gain, is inversely proportional to the distance from the monostatic antenna to the m-th point scatter, $\overrightarrow{\mathbf{R}}$ is range vector from the antenna to the target center, $\overrightarrow{\mathbf{r}_m}$ is the vector from target center to the m-th point scatterer, $||\cdot||$ denotes the norm of a vector, and ν_l denotes the sum of clutter response and measurement noise.

1.2 Cooperative and Uncooperative Modulated Targets

While the ultimate goals of many conventional radars are the measurement of target range and velocity, modern radar systems have demonstrated great potentials in exploring other properties and subtle variations of targets. One example, shown in Fig. 1.1b, can be the use of radar systems in identifying potential hazardous unmanned aerial vehicles (UAVs) for aerial safety monitoring. When the quadcopter is approaching the radar system at a speed of v, in addition to the Doppler shift caused by body translation, a modulation on the carrier frequency is also induced by the rotations of quadcopter propellers. This modulation can be studied by processing the received signal $r(t)$. Another example, as shown in Fig. 1.1c, is found in wireless sensor

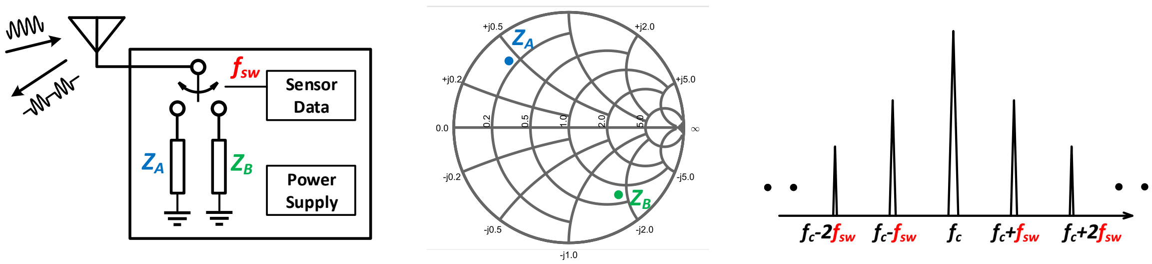

(a) (b) (c)

Figure 1.2: A cooperative phase modulated target with two modulation states: (a) block diagram of a backscatter tag; (b) impedance of two modulation states measured at antenna load termination; (c) sub-carriers in the received backscatter signal frequency spectrum when the switching frequency is fixed.

network applications when a radar system reads modulated backscatter signal from a sensor tag. As the sensor data drives an RF switch to alter the antenna termination between two impedance loads, a phase modulation is added on the radar carrier signal. The sensor tag shows a specific reflectivity and radar cross section under each modulation state. By demodulating the received signal $r(t)$, a bit stream containing sensor data can be obtained.

Both types of targets mentioned above modulate radar carrier signals due to changes in certain properties. From the perspective of targets, the sensor tag actively or cooperatively changes its electrical property to communicate with the radar system, while the quadcopter has no intention to be detected but fails to hide from the radar system because of the changing mechanical properties. **In this work, targets that modulate radar carrier signals are defined as modulated targets. And they are categorized into cooperative targets and uncooperative targets according to their "cooperativeness" to be found and characterized by a radar system**.

1.2.1 Cooperative Modulated Targets

Cooperative targets **intentionally change their reflectivity** (the complex reflection coefficient of each point scatterer) in order to exchange information with the radar. A typical active cooperation can be the backscatter communication between a radar reader and backscatter tags, and the communicated information is the identification data of a radio-frequency identification (RFID) tag or the sensing data of a wireless sensor tag. The change of tag reflectivity can be simply implemented with an RF switch (e.g. a single PIN diode) that alternates the tag antenna termination between two or more impedance loads.

Fig. 1.2 shows the principle of a typical backscatter tag under a binary phase modulation scheme. The tag consists of an antenna, an RF switch driven by the ID/sensor data to switch between the impedance Z_{A} and Z_{B}, and a power supply module that obtains power from the incident radar signal. When the antenna is terminated with different loads, it shows different reflectivity to the radar. And by changing the reflectivity following the data sequence, the radar signal is modulated with sensor data information. If the RF switch alters the antenna termination with frequency f_{sw} when a continuous wave (CW) radar signal at frequency f_{c} is incident on the antenna, subcarriers at frequencies $f_{\mathrm{c}} \pm f_{\mathrm{sw}},\ f_{\mathrm{c}} \pm 2f_{\mathrm{sw}},\ \ldots$, will be observed in the spectrum of the received backscatter signal as shown in Fig. 1.2c [3]. In order to have easily detectable subcarriers (significantly different modulation states), especially over a long communication range, we want Z_{A} and Z_{B} to be as distinctive as possible on the Smith chart shown in Fig. 1.2b. The frequency response expression resulting from **a stationary cooperative target that has N time-variant point scatterers which are static to target center**, similar to Eq. 1.4, can be written as

$$y_l[i] = \overbrace{\sum_{n=1}^{N} \boxed{\rho_{n,l}[i]}\, \alpha_{l,n}^2 e^{-j2\pi f_l \frac{2\left\|\vec{\mathbf{R}}+\vec{\mathbf{r}_n}\right\|}{c_0}}}^{\text{cooperative target response}} + \text{ Multipath} + \nu_l[i], \qquad \alpha_{l,n} \propto \frac{1}{\left\|\vec{\mathbf{R}}+\vec{\mathbf{r}_n}\right\|} \tag{1.5}$$

where i is the sampling index, $\rho_{n,l}[i]$ being the time-variant complex reflection coefficient of the n-th point scatterer, while the one-way path loss $\alpha_{l,n}$ and range vectors are independent of time. The parameter that induces modulation to the carrier signal is highlighted in green.

1.2.2 Uncooperative Modulated Targets

The uncooperative modulated targets do not change the reflection coefficient of point scatterers, however, they still show different reflectivity values to the radar. The **unintentional** changes in the reflectivity is caused by **a variation in the distribution of point scatterers**. One typical uncooperative modulation discussed in the thesis is the micro-Doppler signature caused by a micro-motion of the target [4, 5].

A micro-motion is a secondary motion in addition to the body translation of a target, such as vibration, rotation, and toning motions of the whole body or body parts. For instance, the rotating blades of a helicopter, the spinning tires of a car, the flapping wings of birds, and the swinging arms and legs of a walking person are all seen as micro-motions. They can induce frequency modulation around carrier frequencies.

An example of the generation of micro-Doppler signature is shown in Fig. 1.3. When a propeller is moving towards the radar at a speed of v with a fixed rotation rate of f_{rotate}, the point scatterers existing in the propeller have radial speeds in a sinusoidal like pattern depending on the angle ϕ and hence are their Doppler frequency shifts. The Doppler frequencies of three key positions in Fig 1.3a are mapped to certain points the time-frequency representation [6] (Fig. 1.3b). At position "1", point scatterers have the highest and lowest

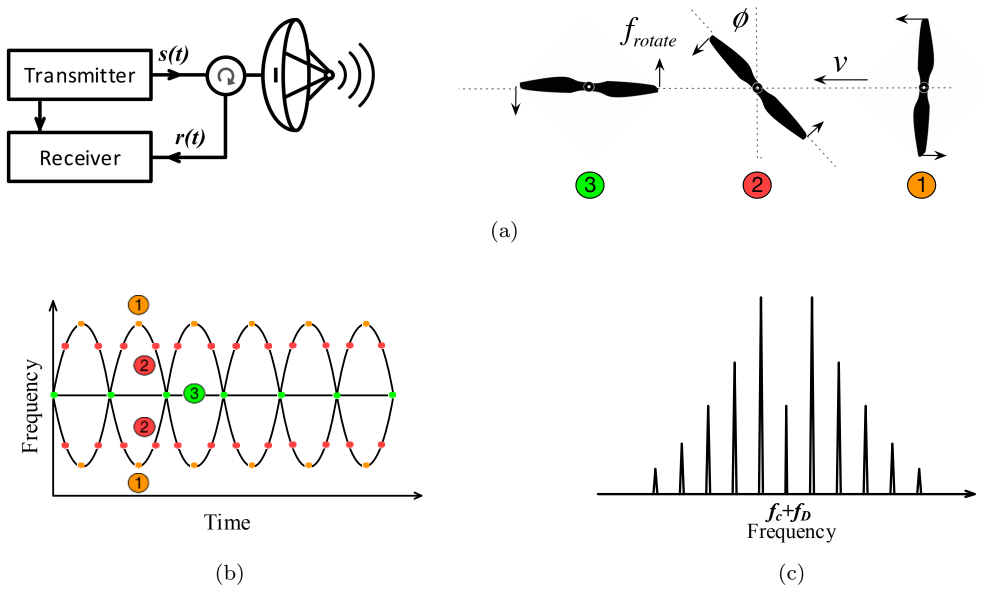

Figure 1.3: Example of an uncooperative target. (a) A propeller approaching the radar with a fixed motion speed and a fixed rotation rate. (b) The micro-Doppler time-frequency analysis. (c) The micro-Doppler frequency spectrum.

radial speed, so in the time-frequency analysis, they are mapped to the peaks and valleys. While at position "3", the radial velocity of all point scatterers are same with the body motion speed. The most widely used time-frequency representation is a spectrogram, defined as the square modulus of the short-time Fourier transform (STFT), which is used in the characterization of uncooperative targets in Chapter 6. Another way to observe the micro-Doppler signature is in the frequency spectrum. By applying a Fourier transform directly to the received signals, sidebands containing Doppler frequencies can be depicted as Fig. 1.3c, which are similar to the tag backscattered subcarriers. The micro-Doppler frequency shifts and spectral envelopes are determined by the radar carrier frequency, antenna polarization, target vibration or rotation rate, and the angle between the micro-motion direction and the radar line of sight. Therefore, the i-th system frequency response sample from **an uncooperative target that consists of N point scatterers with constant reflection coefficient values but are in relative motion to target center** can be written as

$$y_l[i] = \overbrace{\sum_{n=1}^{N} \rho_{n,l}\, \alpha_{l,n}^2[i]\, e^{-j2\pi f_l \frac{2\left\|\vec{\mathbf{R}}[i]+\vec{\mathbf{r}_n}[i]\right\|}{c_0}}}^{\text{uncooperative target response}} + \text{ Multipath} + \nu_l[i], \qquad (1.6)$$

$$\alpha_{l,n}[i] \propto \frac{1}{\left\|\vec{\mathbf{R}}[i]+\vec{\mathbf{r}_n}[i]\right\|}$$

where $\overrightarrow{\mathbf{R}}[i]$, the i-th sampling range vector, $\overrightarrow{\mathbf{r}_n}[i]$, the i-th sampling vector from target center to the n-th target point scatterer, and $\alpha_{l,n}[i]$, the one-way path loss, all vary with time as body motion and micro-motions occur. Complex reflection coefficient $\rho_{n,l}$ is now time-invariant. The rest notations are same with Eq. 1.5. The parts that induce miro-Doppler modulation are highlighted in red.

Although an operating quadcopter and a walking person both have micro-Doppler signatures, their micro-motion patterns are not exactly same. For example, in a quadcopter UAV, the distances between distinguishable points on each propeller remains constant throughout the rotation. This type of targets is defined as rigid body target [5]. In the case of a walking person, however, the distance between an arm and the torso is never constant. Any object with this feature is called a nonrigid body target. There is extensive literature on the classification of nonrigid body targets [7–12]. In this thesis, we only focus on the analysis and modeling of micro-Doppler signatures introduced by micro-motions of rigid body targets.

1.3 Research Questions and Original Contributions

In the previous section, typical applications in the exploration of unmodulated and modulated targets are given to obtain certain signal features. Consequently, the following **research questions** are raised:

1) Is there a unified model/framework that can be used to process different backscatter signals from unmodulated, cooperative, and uncooperative targets?

2) What is the impact of radar configuration on system frequency response? E.g. how does radar motion affect the frequency response?

To answer the first question, the concept of **general modulated target** is proposed and a frequency response model is given based on combining backscatter responses from all point scatterers in this target. The general modulated target can change both the reflection coefficient and the distribution of its point scatterers that are either stationary or in motion (with or without micro-motions) to modulate radar carrier signal. Therefore, the aforementioned unmodulated targets, cooperative targets, and uncooperative targets can all be seen as special cases of general modulated targets. The monostatic radar frequency response with the presence of a general modulated target in the channel is then a combination of Eq. 1.5 and 1.6, thus be written as

$$\begin{aligned} y_l[i] &= \overbrace{\sum_{n=1}^{N} \rho_{n,l}[i]\, \alpha_{l,n}^2[i]\, e^{-j2\pi f_l \frac{2\left\|\overrightarrow{\mathbf{R}}[i]+\overrightarrow{\mathbf{r}_n}[i]\right\|}{c_0}}}^{\text{general modulated target response}} + \text{Multipath} + \nu_l[i], \\ \alpha_{l,n}[i] &\propto \frac{1}{\left\|\overrightarrow{\mathbf{R}} + \overrightarrow{\mathbf{r}_n}[i]\right\|} \end{aligned} \tag{1.7}$$

where $\overrightarrow{\mathbf{r}_n}[i]$ and $\alpha_{l,n}[i]$ change with micro-motions, and $\rho_n[i]$ varies due to the backscatter communication.

To also include the motion of radar systems into consideration, the point scatterer expression in Eq. 1.7 can be further revised to add radar position index k ($k \in \{1, \ldots, K\}$) to the loss factor, target range vector, multipath propagation, and measurement noise. Finally, the full frequency response model accounting for the modulation of a general modulated target and the motion of radar system is:

$$\boxed{\begin{aligned} y_{k,l}[i] &= \overbrace{\sum_{n=1}^{N} \rho_{n,l}[i]\, \alpha^2_{k,l,n}[i]\, e^{-j2\pi f_l \frac{2\left\| \vec{\mathbf{R}}_k[i] + \vec{\mathbf{r}}_n[i] \right\|}{c_0}}}^{\text{general modulated target response}} + \text{Multipath}_k + \nu_{k,l}[i], \\ \alpha_{k,l,n}[i] &\propto \frac{1}{\left\| \vec{\mathbf{R}}_k[i] + \vec{\mathbf{r}}_n[i] \right\|}. \end{aligned}} \tag{1.8}$$

It is noted that this math model is based on a monostatic radar configuration for ease of explanation. It will be easily changed to fit bistatic or multi-static radar systems when necessary. To have even less confusion, we should say collocated or dislocated radar systems when referring to these configurations, since the equation indicates that radar system are sometimes not "static".

In this thesis, the frequency response model that accounts for different types of modulations and the radar motion is used in radar and radar imaging applications to extract various signal features from cooperative and uncooperative targets. The original contributions are:

- For the first time proposed and compared the concepts of cooperative and uncooperative modulated targets from the perspective of reflectivity. Proposed the general frequency response model so that backscatter signals from the cooperative, uncooperative, and unmodulated targets can be modeled and processed using a same framework.

- Develop a first-of-a-kind low-cost X-band backscatter testbed and fabricate sensor tags used as cooperative targets to explore the radar-target cooperation. The X-band testbed system effectively shows a good agreement between measured and simulated free-space path loss at up to 4.1 m and demonstrates a BPSK backscatter modulation configuration at a rate of 10 Mbps.

- Presented an extension of synthetic aperture radar (SAR) techniques to enable simultaneous radar imaging of the reflective objects (unmodulated targets), sensor tag (cooperative target) localization, and backscatter-based data uplink (radar-target cooperation) from multiple sensor tags in a cluttered environment by applying the general modulated target model.

- Utilized balanced orthogonal encoded SAR code words in sensor data packets to enable straightforward tag-vs-clutter discrimination, tag-vs-tag discrimination, multiple access among tags, and improve the signal-to-noise ratio during localization.

- Modeled the 1-bounce multipath propagation effects in simultaneous radar imaging and localization application with first-order virtual point scatterers that are mirrored from targets. Verified the model with SAR measurements in an environment that contains a large reflective plane.

- Comprehensively characterized a quadcopter as a whole modulated target by SAR imaging and radar measurements in different polarimetry for its reflectivity, point scatterer distribution, static and dynamic radar cross sections, and the micro-Doppler frequency shifts while operating. The exploration of micro-Doppler signatures includes interference analysis between multiple rotating propellers and spectral characterization of Doppler frequencies induced by a single propeller rotating at any given rate. The speed-control is realized by a custom-designed flight controller unit that uses a WiFi UDP connection.

- For the first time modeled rotation-induced modulation with point scatterers. Correlated the simulated backscatter signals from a rotating propeller with the measured receive signals at different rotation rates and directions.

1.4 *Thesis Organization*

$$y_{k,l}[i] = \overbrace{\underbrace{\sum_{n=1}^{N} \rho_{n,l}[i]}_{\text{Chapter 2 \& 4}} \underbrace{\alpha^2_{k,l,n}[i]\, e^{-j2\pi f_l \frac{2\left\|\vec{\mathbf{R}}_{k}[i] + \vec{\mathbf{r}}_n[i]\right\|}{c_0}}}_{\text{Chapter 6 \& 7}}}^{\text{modulated target response}} + \underbrace{\text{Multipath}_{k}}_{\text{Chapter 5}} + \nu_{k,l}[i]$$

Chapter 1 introduces basic radar principles and important parameters, proposes the concepts of cooperative and uncooperative modulated targets, derives a point scatterer model for general modulated targets that accounts for radar motion, and provides the motivation to explore modulated targets with radar and radar imaging technologies.

Chapter 2 gives a typical “cooperation” between a radar system and targets which is the microwave backscatter communication. The chapter begins with highlighting the advantages of backscatter communication in the microwave spectrum. Then the design of a custom low-cost X-band backscatter testbed and a cooperative backscatter are given with system-level path loss measurements and a demonstration of BPSK backscatter commutation.

Chapter 3 has an emphasis on the radar motion in the point scatterer model. The chapter overviews conventional and innovative applications of synthetic aperture radar (SAR) technologies, introduces the mechanisms and important characteristics of SAR imaging, and proposes a SAR image reconstruction algorithm which is applied in the following chapters.

Chapter 4, based on the contents in Chapter 2 and Chapter 3, combines the applications of SAR imaging and backscatter up-link at X-band using one radar system. In Chapter 4.1 & 4.2, the math is given and an encoding method is proposed to enable straightforward tag-vs-clutter discrimination, tag-vs-tag discrimination, and multiple access among tags. From Chapter 4.3 to 4.6, an indoor experiment is discussed to validate the model, and a simple phase center calibration method is used to lower the localization errors to millimeter level and imaging resolution to centimeter level when the tags are around 5 m to the radar.

Chapter 5 models the 1-bounce multipath propagation in the simultaneous SAR imaging and localization application with first-order virtual point scatterers mirrored from modulated targets. The same measurement from Chapter 4 is implemented again after adding a large reflective surface into the environment. Chapter 5.3 shows the reconstruction results where virtual targets coexist with their actual targets in both imaging and localization scenarios.

Chapter 6 starts with an introduction of the current research on uncooperative UAV targets. Then the hardware composition of a quadcopter, illustrated as an uncooperative target, and characterization methods of the scattering properties are given based on the point scatterer model. In chapter 6.2, the quadcopter is mainly characterized as an unmodulated target in 3-D SAR measurements and static RCS measurements. In chapter 6.3, the micro-Doppler signature of the quadcopter is explored when different propellers are rotating at different rates and in different directions using a custom K-band radio to collect the backscatter signals and a flight controller unit to control propeller rotations.

Chapter 7 continues the work on micro-Doppler signature characterization but only models the rotation of a single propeller that operates at different rates and directions with limited number of point scatterers. Chapter 7.1 finds the math of how each point scatterer modulates the amplitude and frequency of the carrier signal. Chapter 7.2 uses SAR imaging to learn the distribution of point scatterers on different surfaces and edges of a propeller. In Chapter 7.3, a number of point scatterers are selected based on the SAR images and then used in simulations to match the micro-Doppler measurement results at different rotation rates and in different directions.

Finally, research conclusions and a discussion of future work are provided in Chapter 8.

1.5 Publications

All publications to date are listed below:

[1] **X. Fu**, A. Pedross-Engel, D. Arnitz, C. M. Watts, A. Sharma, and M. S. Reynolds, “Simultaneous Imaging, Sensor Tag Localization, and Backscatter Uplink Via Synthetic Aperture Radar,” IEEE Transactions

on Microwave Theory and Techniques, vol. 66, no. 3, pp. 1570 - 1578, 2018.

[2] A. Pedross-Engel, D. Arnitz, J. N. Gollub, O. Yurduseven, K. P. Trofatter, M. F. Imani, T. Sleasman, M. Boyarsky, **X. Fu**, D. L. Marks, D. R. Smith, and M. S. Reynolds, "Orthogonal Coded Active Illumination for Millimeter Wave, Massive-MIMO Computational Imaging with Metasurface Antennas," IEEE Transactions on Computational Imaging, vol: 4, no. 2 , pp. 84 - 193, 2018.

[3] **X. Fu**, A. Pedross-Engel, D. Arnitz, and M. S. Reynolds, "Simultaneous Sensor Localization via Synthetic Aperture Radar (SAR) Imaging," in 2016 IEEE SENSORS, Orlando, FL, USA, Sept. 2016, pp. 1 - 3.

[4] **X. Fu**, A. Sharma, E. Kampianakis, A. Pedross-Engel, D. Arnitz, and M. S. Reynolds, "A Low Cost 10.0 - 11.1 GHz X-Band Microwave Backscatter Communication Testbed with Integrated Planar Wideband Antennas," in 2016 IEEE International Conference on RFID, Orlando, FL, May 2016, pp. 1 - 4.

Chapter 2

MICROWAVE BACKSCATTER COMMUNICATION: A TYPICAL RADAR-TARGET COOPERATION

This chapter is a modified version of [13]:

- **X. Fu**, A. Sharma, E. Kampianakis, A. Pedross-Engel, D. Arnitz, and M. S. Reynolds, "A Low Cost 10.0 - 11.1 GHz X-Band Microwave Backscatter Communication Testbed with Integrated Planar Wideband Antennas," in 2016 IEEE International Conference on RFID (RFID 2016), Orlando, FL, May 2016, pp. 1 - 4.

In this chapter, the microwave backscatter communication, which is a typical "cooperation" between a radar system and targets, is discussed based on the point scatter expression of the general modulated targets. To just focus on the cooperation at high microwave frequencies and the path loss of communication channel, only stationary cooperative targets and radar systems are discussed. The full frequency response model

$$\boxed{y_{k,l}[i] = \overbrace{\sum_{n=1}^{N} \rho_{n,l}[i]\, \alpha^2_{k,l,n}[i]\, e^{-j2\pi f_l \frac{2\left\|\vec{\mathbf{R}}_k[i] + \vec{\mathbf{r}_n}[i]\right\|}{c_0}}}^{\text{general modulated target response}} + \text{ Multipath}_k + \nu_{k,l}[i]}$$

is simplified by leaving out the radar motion index, the micro-motion vectors, and multipath propagation components, and the math for this chapter is given as

$$y_l[i] = \overbrace{\sum_{n=1}^{N} \rho_{n,l}[i] \alpha^2_{l,n} e^{-j2\pi f_l \frac{2\left\|\vec{\mathbf{R}} + \vec{\mathbf{r}_n}\right\|}{c_0}}}^{\text{cooperative target response}} + \nu_l[i]. \tag{2.1}$$

A custom-designed low-cost testbed and a backscatter tag, used as a cooperative target, are fabricated at X-band to validate the model. A good agreement is found between the measured and simulated free-space path loss at ranges of up to 4.1 m in a laboratory environment indicating the multipath propagation is not a significant contributor to path loss at this frequency, and backscatter data at a rate of 10 Mbps under a BPSK modulation scheme is successfully demodulated with the testbed.

2.1 Introduction to Microwave Backscatter Communication

Microwave backscatter communication has a long history; indeed the first experiments in backscatter communication were conducted by Harry Stockman in 1948 with an X-band (3 cm wavelength) radar and mechanical microwave backscatter modulator structures [14]. Then commercial applications of backscatter communication were widely seen in automated tolling systems and inventory management at much lower radio frequencies where cars and goods were assigned RFID tags that can be interrogated by a reader infrastructure [15, 16]. Despite the success of Stockman's early work in the microwave regime, microwave backscatter communication has received less attention, due in part to the low cost and pervasiveness of the billions of passive RFID tags operating under EPC standards at $850-950$ MHz (in the UHF spectrum).

Some recent research on backscatter communication includes the exploration of new reader systems and applications that do not adhere to preexisting RFID standards. Kellogg et al. [17] and Ishizaki et al. [18] showed it is possible to decode backscatter messages with WiFi access points. Ensworth et al. in [19, 20] demonstrated backscatter data uplinks between backscatter devices and unmodified standard wireless devices that use a Bluetooth Low Energy standard. Kampianakis et al. [21,22] demodulated backscatter signals from implantable devices showing the capability of real-time neural signal processing at 6.25 Mbps. There is also interesting work using Wireless Identification and Sensing Platform (WISP) to demonstrate battery free cameras and sensors [23–26]. Most of the work mentioned above are in the UHF spectrum because there are existing communication protocols, the path loss at these frequencies is lower compared to systems at microwave frequencies, and a good read range is easily reachable with an operation frequency of several hundreds of megahertz.

Compared to the above systems, the high frequencies and short wavelengths of microwave signals make the design and mass-production of microwave backscatter systems much more difficult. But cheerfully, some new development of backscatter systems and transponders at high microwave frequencies are coming back in sight lately. Tabesh et al. proposed a 60 GHz 65 nm CMOS UWB RFID transponder with a data rate higher than 12 Mbps [27]. In [28], multi-antenna testbeds were designed to reduce multipath fading in backscatter channel at 5.8 GHz. Besides, active tags at 34.3-34.8 GHz, passive tags at 61 GHz and 76 GHz of high data speed, interrogated by FMCW radar modules to extract range and data information, are seen in [29–31] respectively. The following aspects of microwave backscatter systems provide unique opportunities that merit attention in the research community:

- **Small electrical size.** Since the gain of antenna is proportional to its electrical size, at higher frequencies, more gain can be obtained for a given size. Very small (few cm^2) full-sized microwave antennas can be very efficient and exhibit significant gain and narrow beam width.
- **More bandwidth.** The wider bandwidths in the microwave range allow for much higher data rates

than can be achieved in UHF bands. A 1% bandwidth at 9 GHz is 90 MHz, providing a maximum data rate of 90 Mbps. While at 900 MHz, a 1% bandwidth only allows for a 9 Mbps data rate.

- **Short wavelength**. The shorter wavelengths in the microwave and millimeter wave bands allow for interesting combinations of RFID-like backscatter sensor data uplinks integrated with high resolution coherent imaging to be simultaneously realized using a same system.

Given the above advantages, we choose to experiment backscatter communication in X-band. First, we would like to see if a prototype system can be easily developed to effectively demodulate real-time backscatter data. Then, in future chapters, we will combine the application of backscatter communication with the application of radar imaging using a same radar system. In this chapter, we managed to develop a low-cost X-band backscatter testbed and some sensor tags used as cooperative targets to explore the cooperation between radar systems and cooperative targets. The testbed system effectively shows a good agreement between measured and simulated free-space path loss at a range of up to 4.1 m and demonstrates a BPSK backscatter modulation configuration a rate of 10 Mbps.

2.2 Modulated Backscatter

2.2.1 Modulation Factor and Differential Radar Cross Section

Fig. 2.1 shows the principle of a typical tag in backscatter communication. It modulates the field by switching the antenna termination between two impedance loads, which effectively changes its reflectivity or radar cross section to the radar. The complex reflection coefficient of the varying load looks to the antenna is

$$\rho_{A,B} = \frac{Z_{A,B} - Z_{\text{ant}}^*}{Z_{A,B} + Z_{\text{ant}}}, \tag{2.2}$$

where $Z_{A,B}$ is the complex impedance of either state A or B, Z_{ant} is the complex impedance of the antenna, and (-)* is the complex-conjugate operator. The radar cross section corresponding to either state is

$$\sigma_{A,B} = \frac{\lambda^2 G_t G_r}{4\pi} |\rho_{A,B}|^2, \tag{2.3}$$

where λ is the wavelength, and G_t and G_r are the gain of transmit and receive antennas [32].

In the backscatter communication link, the reflected power is dependent on this difference in load states and proportional to the modulation factor defined as [33]:

$$\text{MF} = \frac{1}{4} \left|\rho_A - \rho_B\right|^2. \tag{2.4}$$

An alternative method for characterizing the power scattered from the tag is to use the differential radar cross section given as

$$\Delta\sigma = \frac{\lambda^2 G_t G_r}{4\pi} |\rho_A - \rho_B|^2. \tag{2.5}$$

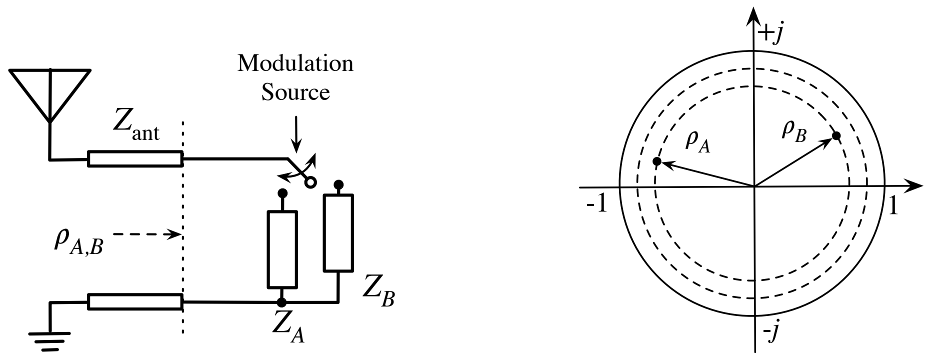

(a) Load Impedance

(b) Reflection Coefficient

Figure 2.1: Relation between load impedance and reflection coefficient on the Smith Chart.

2.2.2 Forward Link and Backscatter Link

Friis Transmission Equation

Before we start on the two power links in backscatter communication, it is necessary to go over the Friis transmission equation that relates the power received by one antenna to the power transmitted from another antenna. The two antennas are in the far field of each other (like shown in Fig. 2.2a). When the power density W_t of the transmit antenna is [34]

$$W_t = \frac{P_t G_t}{4\pi R^2}, \tag{2.6}$$

where P_t is the input power to the transmit antenna, G_t, as denoted before, is the gain of transmit antenna, and R is the one way distance between the two antennas. Along with the effective area of receive antenna

$$A_r = G_r \frac{\lambda^2}{4\pi}, \tag{2.7}$$

the power collected by the receiver is then

$$P_r = A_r W_t = \left(\frac{\lambda}{4\pi R}\right)^2 G_t G_r P_t, \tag{2.8}$$

where G_r is the gain of receive antenna.

Received Power Scattered from Unmodulated Targets

When the transmit power is incident on an unmodulated target as shown in Fig. 2.2b, the power captured by the target P_u is a multiplication of its effective antenna area (radar cross section) and the transmit power density, given as

$$P_u = \sigma W_t = \sigma \frac{P_t G_t}{4\pi R_1^2}, \tag{2.9}$$

where R_1 is the distance from transmit antenna to the target center. The power density of the scattered wave from the unmodulated target, revised from Eq. 2.6, is

$$W_s = \frac{P_u}{4\pi R_2^2} = \sigma \frac{P_t G_t}{(4\pi R_1 R_2)^2}, \tag{2.10}$$

where R_2 is the distance from the receive antenna to the target center. Thus, the received backscatter power from an unmodulating target is

$$P_r = A_r W_s = \sigma \left(\frac{\lambda}{4\pi R_1 R_2}\right)^2 \frac{P_t G_t G_r}{4\pi}, \tag{2.11}$$

base on which the 2-way E-field loss factor in the point scatterer model of the modulated targets can be derived as

$$\alpha_{l,n}^2 = \sqrt{\left(\frac{\lambda}{4\pi R_1 R_2}\right)^2 \frac{G_t G_r}{4\pi}} = \frac{\lambda}{4\pi R_1 R_2}\sqrt{\frac{G_t G_r}{4\pi}}. \tag{2.12}$$

Received Power Scattered from Cooperative Targets

When the transmit power is incident on an cooperative target which has its own antenna for backscatter modulation as shown in Fig. 2.2c, the forward link and backscatter link can each be applied with the Friis transmission equation for the transmission power. The signal power captured by the cooperative target P_c is then

$$P_c = \left(\frac{\lambda}{4\pi R_1}\right)^2 G_t G_c P_t, \tag{2.13}$$

where G_c is the gain of target antenna. Since the transmit power from the target is not exactly the power it captured but reduced by the modulation factor MF, the received backscatter signal power at the receiver is

$$P_r = \left(\frac{\lambda}{4\pi R_2}\right)^2 G_c G_r P_c \mathrm{MF} = \left(\frac{\lambda}{4\pi R_1}\right)^2 \left(\frac{\lambda}{4\pi R_2}\right)^2 G_t G_r G_c^2 \mathrm{MF}. \tag{2.14}$$

It is noted that all the above calculations do not account for antenna mismatch loss, polarization mismatch loss, and multipath propagation.

2.3 Design of a Low-Cost X-Band Backscatter Testbed and Cooperative Targets

We developed a low-cost X-band testbed (see Fig. 2.3) that consists of a transmitter (TX) front-end module, a receiver (RX) front-end module, and a Universal Software Radio Peripheral (USRP) providing a reference input to TX front-end and a baseband module for the RX. In addition, the backscatter tag illustrated in the figure is an example of low-cost cooperative targets that can be used in many different applications.

The low fabrication cost of the testbed is due to single-board integration of inexpensive silicon germanium (SiGe) integrated circuits intended for consumer satellite TV with an integrated planar wideband bow-tie antenna on a low cost substrate. The satellite TV ICs are produced in extremely high volume (millions of

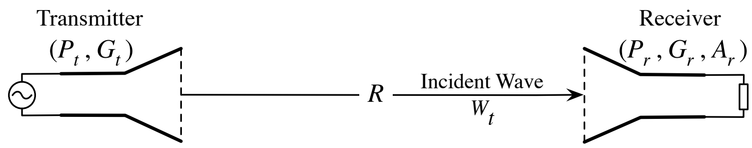

(a)

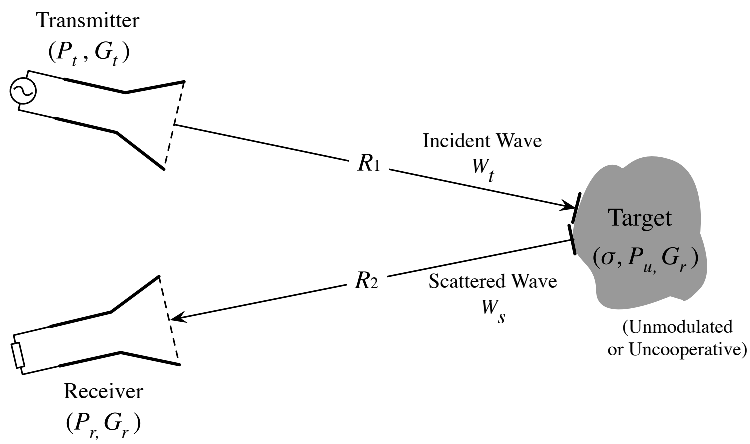

(b)

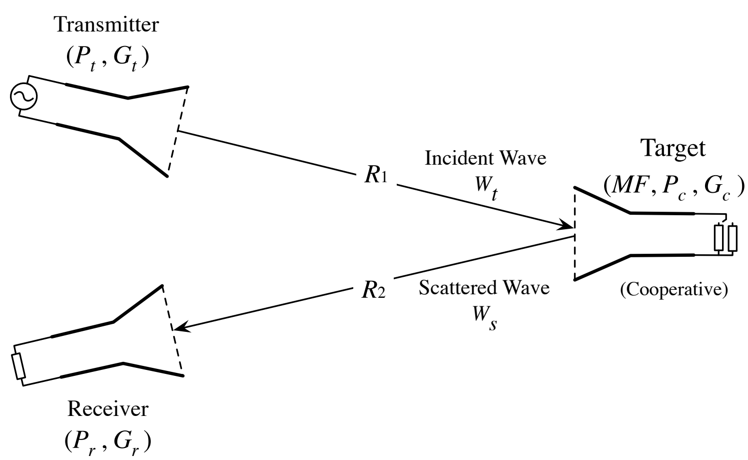

(c)

Figure 2.2: Schematics showing the relations between the power received and the power transmitted. (a) A radio wave from a transmitter directly incident on the receiver. (b) An unmodulated target or an uncooperative target scatters a signal from transmitter to the receiver. (c) A cooperative target backscatters an electromagnetic wave from the transmitter to the receiver.

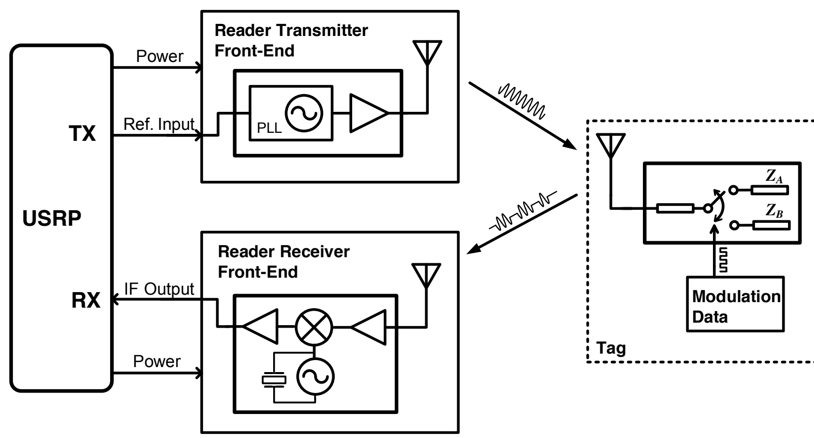

Figure 2.3: Block diagram of the low-cost X-band backscatter testbed and a low-cost backscatter tag as an example of cooperative modulated targets.

units) and consequently have a low unit price. In this testbed we leverage the NXP TFF11105HN integrated LO source (price \$9.23 each) in the TX front-end and the NXP TFF1018HN integrated downconverter (price \$0.55 each) in the RX front-end.

These components are integrated with the bow-tie antennas on a two-layer 0.5 mm thick Rogers RO4003 (1/2 oz. Cu, $\epsilon_r = 3.35$, $\tan\delta = 0.003$) substrate measuring only 6 cm $\times$ 3.5 cm. This design is simple and robust to manufacturing tolerances. The layout of transmitter and receiver antennas and front-end modules are shown in Fig. 2.4.

Furthermore, we present a proof-of-concept transponder consisting of a single Hittite HMC547LC3 SPDT switch and a stand-alone bow-tie antenna as a BPSK backscatter tag. For initial testing, the modulation source is an Agilent 33500B series arbitrary waveform generator. The fabricated PCB boards of TX and RX front-end modules and the tag fixed in 3D printed holders are shown in Fig. 2.5. In Chapter 4, an improved design of backscatter tag that modulates radar signal with real sensor data will be discussed.

2.3.1 Wideband Bow-tie Antenna

The wideband bow-tie topology was selected because it has high efficiency, a wide bandwidth, is easy to manufacture and has a low fabrication cost [35]. In this design, the top copper layer contains the bow-tie antenna and the coplanar waveguide (CPW) feed, and bottom layer contains a microstrip feed line. A microstrip to CPW transition was designed using an open-ended circular resonator and the microstrip feed line was connected to the RF input of the RFICs. The dimensions of the ring resonator transition were

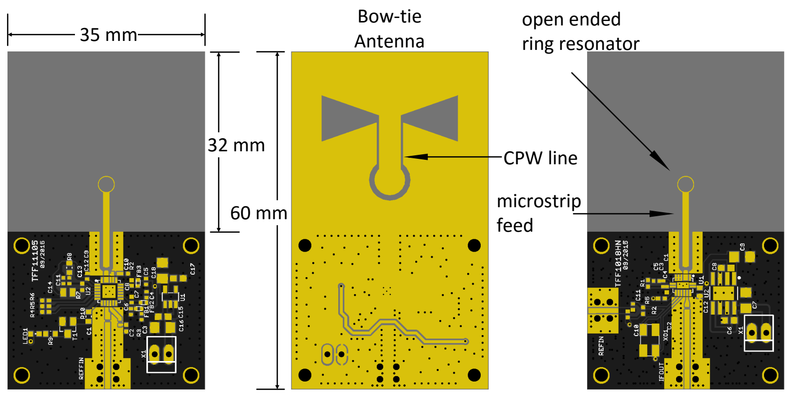

(a) (b) (c)

Figure 2.4: Layouts of (a) TX component side, (b) antenna side of TX and RX, and (c) RX component side.

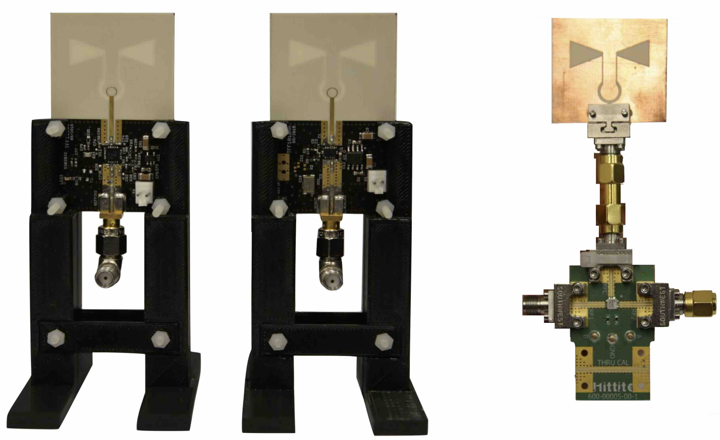

(a) (b) (c)

Figure 2.5: Photos of (a) transmitter PCB and holder, (b) receiver PCB and holder, and (c) BPSK backscatter tag.

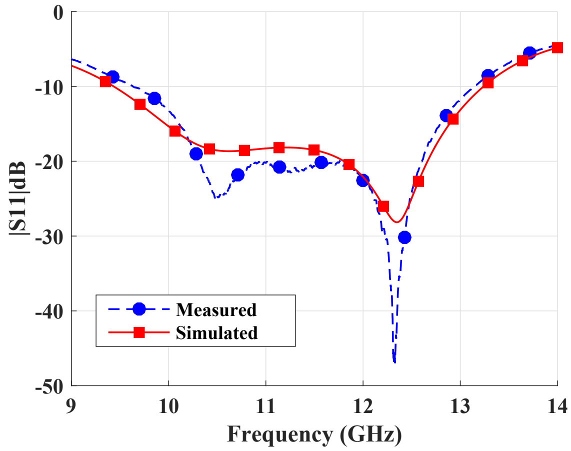

Figure 2.6: Simulated and measured $|S_{11}|$ of the bow-tie antenna.

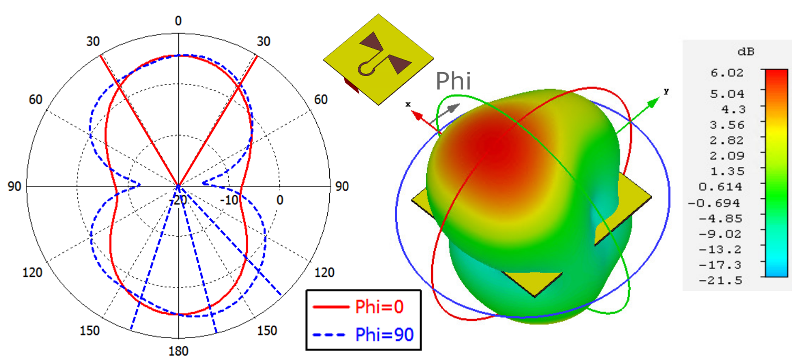

Figure 2.7: Simulated radiation pattern of bow-tie antenna.

optimized to maximize E-field coupling between the microstrip and the CPW [36].

Antenna parameters were optimized using CST Microwave Studio with the finite integral technique (FIT). Antenna performance was characterized using an Agilent N5227A vector network analyzer (VNA). The measured S-parameters were in good agreement with the simulation, as shown in Fig. 2.6. The measured -10 dB bandwidth of the bow-tie antenna is 3.51 GHz and the center frequency is 11.38 GHz. The simulated radiation pattern (Fig. 2.7) indicates a maximum gain of 6.02 dB at 10.75 GHz.

2.3.2 Transmitter Front-End

The transmitter front-end board is based on the NXP TFF11105HN, a low phase noise LO source intended for Ku band VSAT uplinks. It consists of an integrated PLL, VCO, output buffer, and lock detector. An

Table 2.1: Measured TX front-end Performance

Parameter	Value
Reference frequency range	156.25 MHz - 173.4375 MHz
RF output frequency	10.0 GHz - 11.1 GHz
Minimum input power	-30 dBm
Power output	-2 dBm @ 10.5 GHz -3 dBm @ 10.75 GHz
Phase noise	Measured at 10.75 GHz RF output -57.0 dBc/Hz @ 1 kHz -65.5 dBc/Hz @ 10 kHz -81.6 dBc/Hz @ 100 kHz -100.2 dBc/Hz @ 1 MHz
Power consumption	3.3 V, 100 mA, 330 mW

external power supply circuit, passive loop filter, and PLL lock indicator were designed to match this IC. The transmitter's PLL synthesizer multiplies an external HF or UHF reference signal up to an X-band carrier with a configurable multiplication ratio. The X-band carrier is amplified by the on-chip buffer and radiated from the bow-tie antenna. Final stage divider settings can be changed manually by pin strapping from 2^4-2^8. In the measurements of Section 2.4, the divider setting of 64 is chosen. A minimum reference power input of -30 dBm is required to yield an X-band carrier from 10.0 GHz to 11.1 GHz with an output power of -3 dBm to -2 dBm. The measured performance of the transmitter front-end is shown in Table 2.1.

2.3.3 Receiver Front-End

The receiver front-end leverages the high integration, low power consumption, and low price ($0.55 each) of NXP's TFF1018HN integrated satellite downconverter ICs. These ICs are produced in extremely high volume for consumer satellite receivers. The IC includes an integrated LNA, mixer, LO frequency synthesizer, and an IF gain stage. The only external components required are a 25 MHz reference crystal, a passive loop filter, and a biasing IC. The receiver board down-converts the X-band backscattered signal to UHF, and then amplifies the signal with the on-chip IF gain stage. The measured RF frequency range of the receiver front-end is 10.0 GHz to 13 GHz. With the 9.75 GHz LO frequency, the IF frequency range is 250 MHz to 3250 MHz. The measured conversion gain of the board is 36 dB at 1 GHz IF, with a flatness of ± 4 dB over the 3 GHz bandwidth. The measured receiver performance is shown in Table 2.2.

Table 2.2: Measured RX front-end performance

Parameter	Value
RF frequency range	10.0 GHz - 13.0 GHz
IF frequency range	250 MHz - 3250 MHz
Conversion gain	36 dB @ 1 GHz IF output 28 dB @ 250 MHz IF output
Input 1 dB compression	-16 dBm @ 1 GHz IF output
Noise Figure	7 dB (per NXP data sheet)
Power consumption	5 V, 55 mA, 275mW

2.3.4 Proof-of-Concept X-Band BPSK Tag

The proof-of-concept X-Band tag switches the tag antenna between two load impedances to form a BPSK backscatter modulation. We used the same bow-tie antenna as in the TX and RX boards, connected to a Hittite HMC547LC3 wideband MESFET switch. The HMC547LC3 is far over-specified for this application, having a DC to 28 GHz bandwidth with very high isolation between two RF ports and a switching speed up to 150 MHz. A lower cost PIN switch will be discussed in Chapter 4. In the experiments, an Agilent 33500B series arbitrary waveform generator served as the modulation source. The RF1 and RF2 ports of the HMC547LC3 switch are connected to a short and an open termination respectively. The switch is operated under single-ended negative control voltages of -5/0 V with no added bias requirement.

Fig. 2.8 shows the S_{11} (reflection coefficient) of the switch as measured in each of the two load states over 10.0 GHz-11.1 GHz using an Agilent VNA. Complex reflection coefficient values ρ_{A} and ρ_{B} were measured at the antenna termination (see the reference plane in Fig. 2.1a) for state A and state B. In this BPSK modulation scheme, the amount of modulated-backscatter power is proportional to the modulation factor MF. At 10.75 GHz, it is calculated as

$$\mathrm{MF} = \frac{1}{4}\left|\rho_{\mathrm{A}} - \rho_{\mathrm{B}}\right|^2 = 0.54.$$

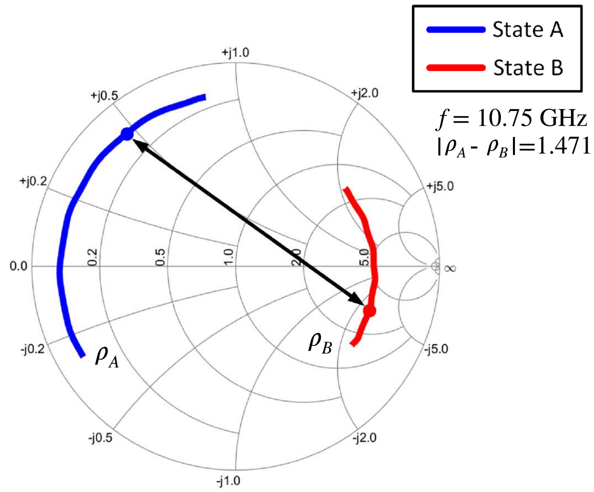

Figure 2.8: Measured S_{11} of the X-Band tag from 10 to 11.1 GHz.

2.4 System-Level Measurements

In addition to the presented component-level test results, several system-level testings using this infrastructure are also conducted. In this section, an indoor measurement is first designed to measure the received backscatter signal power and compare to the free-space backscatter link budget, then a BPSK backscatter communication is demonstrated with this testbed at a data rate of 10 Mbps. The system is characterized at a fixed mid-band frequency of 10.75 GHz. Similar measurement results are expected at any carrier frequency in the available band of 10.0 GHz-11.1 GHz.

2.4.1 Simulated Free-Space Model and Measured Path Loss

X-Band Backscatter Link Budget

The RF channel in which a backscatter-radio system operates is composed of two parts: the forward link and the backscatter link. By using the Friis free-space model for each link, the level of modulated-backscatter power received by the reader can be achieved in Eq. 2.14. In this setup, the tag has a same antenna as the transmitter and receiver, so the recieved power is

$$P_{\mathrm{r}} = \frac{P_{\mathrm{t}} G^4 \lambda^4 \mathrm{MF}}{(4\pi R)^4} \tag{2.15}$$

where G is the gain of bow-tie antenna, R represents the distance from either radar antenna to the tag antenna, and MF is the known modulation factor. Eq. 2.15 does not account for antenna mismatch loss and multipath propagation in the environment. The predicted backscatter carrier power is plotted in Fig. 2.10.

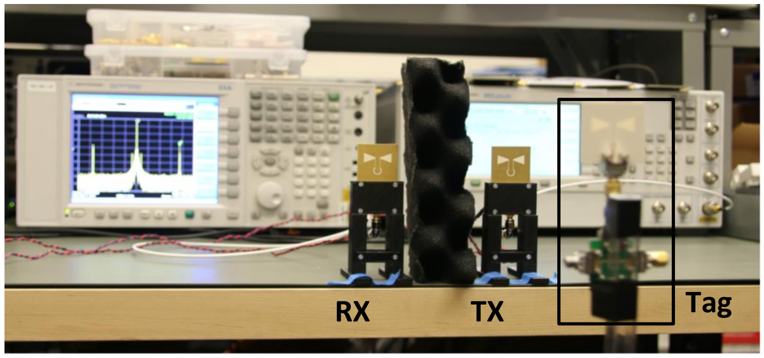

(a)

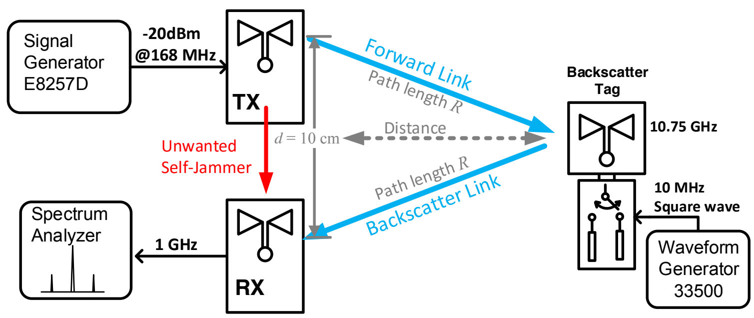

(b)

Figure 2.9: Backscatter power measurement setup: (a) photo (b) block diagram.

Measurement Setup and Results

The indoor laboratory measurement setup that is used to test the backscatter power received by reader is shown in Fig. 2.9. The transmitter board and receiver board are placed side by side on the bench with a distance of d = 10 cm. A piece of AEMI Inc. AEC-4-MM absorber was placed between them to reduce the unwanted self-jammer. The reader antennas and the tag antenna were 1 m above the floor. A CW reference signal with a frequency of 168 MHz and power of -20 dBm was generated by an Agilent E8257D signal generator and fed in to the transmitter board. The resulting 10.75 GHz CW carrier was radiated from the transmitter antenna, and backscattered by the tag into the receiver board.

After downconverting the backscatter signal, the expected 1 GHz IF frequency with the double-sided backscatter modulation was observed using an Agilent N9010A spectrum analyzer. During the measurement, the tag was moved along the line perpendicular to the bench, thus bisecting the angle between the transmitter and receiver antennas. The tag to reader distance was varied from 0.1 to 4.1 m in 0.05 m steps. Fig. 2.10

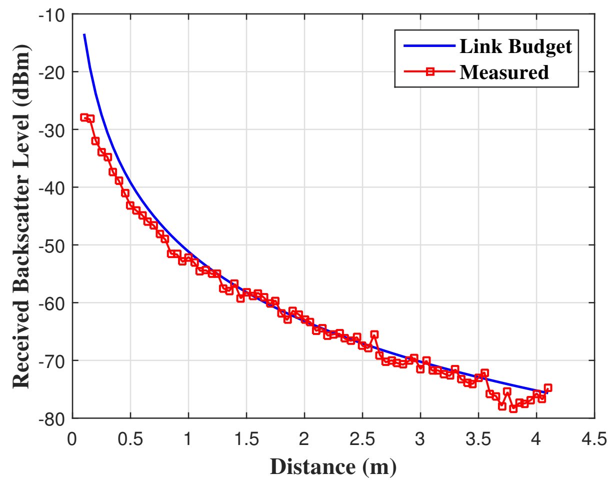

Figure 2.10: Friis model vs. measured backscatter power.

plots the observed backscatter power vs. the distance in comparison to the calculated results from the link budget.

The good agreement between the measured backscatter receiving power and the free-space Friis model indicates that this type of X-Band setup is operating in a line-of-sight environment where multipath from the ground, walls, and etc. (large non-reflective objects and clutters in the environment) is not a significant contributor to the signal path loss. This backscatter channel is likely a robust channel for a potential high data rate backscatter communication.

2.4.2 X-Band BPSK Backscatter Communication at 10 Mbps

Characterization of the system using a BPSK communication scheme was also realized with this testbed. The experiment setup is shown in Fig. 2.11, in which a USRP B-210 is connected to the TX and RX front-ends in place of the signal generator and the spectrum analyzer used in the previous backscatter power measurement. A binary data sequence of 128 random bits was generated at a rate of 10 Mbps using an Agilent 33500 waveform generator to drive the backscatter modulator. The switching tag was placed at a distance of 0.5 m from the TX-RX pair and the USRP B-210 with a maximum IF bandwidth of 50 MHz was utilized in order to downconvert the IF signal to baseband at a sampling frequency of 50 Msps. The resulting I/Q samples were post-processed in MATLAB. Fig. 2.12 shows a part of one packet demodulated data after resampling, carrier frequency offset compensation, symbol synchronization, and filtering. Fig. 2.13 shows the eye diagram of the resulting data packet.

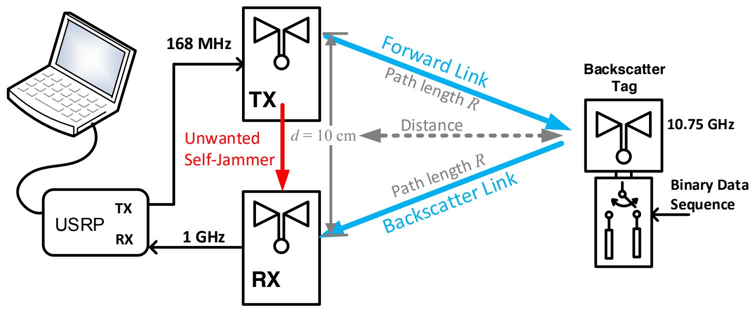

Figure 2.11: BPSK Backscatter communication setup.

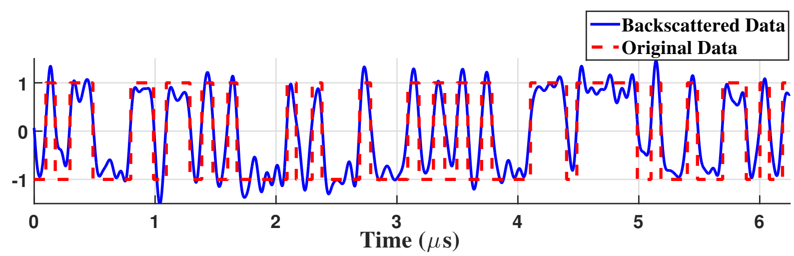

Figure 2.12: Demodulated backscatter data vs. original data sequence in the tag (only a part of one data packet is shown).

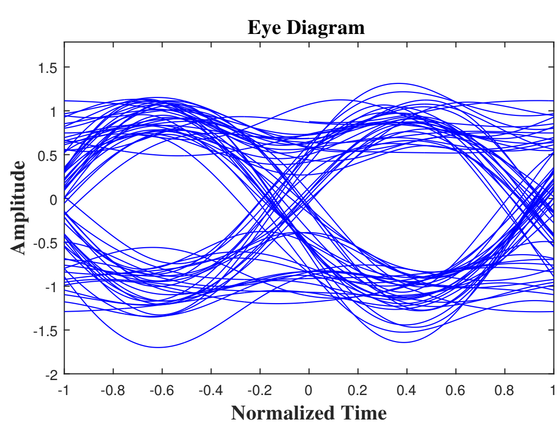

Figure 2.13: Eye diagram of one packet demodulated data.

2.5 Chapter Conclusion

In this chapter, a first-of-a-kind low-cost X-band backscatter testbed and a backscatter tag, as an example of cooperative targets, are fabricated to explore the radar-target cooperation. This system is first used in the characterization of the received backscatter signal power. Measurement results are collected over a range of up to 4.1 m and compared to the channel link budget derived from the free-space Friis model. The good agreement between measurements and link budget indicates that the multipath propagation is not a significant contributor to communication path loss in this setup. Then the testbed is used in the demonstration of a BPSK backscatter modulation configuration at a rate of 10 Mbps.

Next, we are going to research the combination of RFID-like backscatter sensor data uplinks and high resolution microwave imaging when these two functions are simultaneously realized using a same radar system.

Chapter 3

SYNTHETIC APERTURE RADAR (SAR) IMAGING: AN APPLICATION BASED ON RADAR MOTION

This chapter is a modified version of Section II in [37]:

- **X. Fu**, A. Pedross-Engel, D. Arnitz, C. M. Watts, A. Sharma, and M. S. Reynolds, "Simultaneous Imaging, Sensor Tag Localization, and Backscatter Uplink Via Synthetic Aperture Radar," IEEE Transactions on Microwave Theory and Techniques, vol. 66, no. 3, pp. 1570 - 1578, Mar 2018.

In this chapter, the frequency response model is exploited with a focus on radar motion under the preassumption that all targets are stationary. Usually, radar systems that utilize their own movements to explore scattering properties of a field are synthetic aperture radars (SARs). This chapter introduces the SAR platform and reconstruction algorithm the author has been working on. The infrastructure is used in future chapters on all types of targets.

The full point scatterer expression accounting for target modulation and radar motion

$$\boxed{y_{k,l}[i] = \overbrace{\sum_{n=1}^{N} \rho_{n,l}[i]\, \alpha^2_{k,l,n}[i]\, e^{-j2\pi f_l \frac{2\left\|\vec{\mathbf{R}}_k[i] + \vec{\mathbf{r}_n}[i]\right\|}{c_0}}}^{\text{general modulated target response}} + \text{ Multipath}_k + \nu_{k,l}[i]}$$

is simplified by leaving out the micro-motion and multipath propagation components to fit SAR imaging applications. The rest of the chapter is based on the frequency response model in this form

$$y_{k,l}[i] = \overbrace{\sum_{n=1}^{N} \rho_{n,l}[i] \alpha^2_{k,l,n} e^{-j2\pi f_l \frac{2\left\|\vec{\mathbf{R}}_k + \vec{\mathbf{r}_n}\right\|}{c_0}}}^{\substack{\text{cooperative modulated target and} \\ \text{unmodulated target response}}} + \nu_{k,l}[i]. \tag{3.1}$$

3.1 Introduction to SAR Imaging Technology

Traditionally, synthetic aperture radar imaging has been widely used for earth remote sensing and military surveillance to provide high-resolution images independent of daylight, cloud coverage and weather conditions [38]. After the discovery and initial developments of SAR systems in the 1950s by military research and use for reconnaissance purposes [39], several airborne SAR systems for civilian applications with a goal to retrieve large-scale geo-physical parameters from the Earth surface were developed in the 1970s and 1980s [40]. In the 1990s high quality polarimetric SAR data became widely available with a growing number of airborne systems [41] like the E-SAR [42], the Canadian CV580 system [43], and the NASA/JPL's AIRSAR [44]. The development of such systems also pioneered the way and provided technologies to the even more advanced spaceborne systems that have swath widths up to 500 km. As of now, more than 20 spaceborne SAR sensors have been launched including the famous TerraSAR-X/TanDEM-X [45, 46], Radarsat-2 [47], and etc.

In addition to the large-scale surveillance and geological applications, there are emerging innovative applications using SAR technologies, such as SAR-based security screening [48–51], robot navigation [52, 53], sensors for autonomous vehicles [54, 55], and etc. Interesting research on digital beamforming and MIMO-SAR system development is trying to maximize the imaging capabilities of the hardware systems and leaves the strenuous processing task on the software end [56, 57]. Apart from the above, SAR approaches have previously been suggested for holographic localization of UHF backscatter transponders [58, 59]. Based on a coherent superposition of phase values taken along a synthetic aperture, the calculated holographic image yields a spatial probability density function of possible tag positions. This provides us the motivation to combine backscatter communication and SAR imaging in the exploration of cooperative targets.

3.2 SAR Principles and Important Terminologies

3.2.1 Basic SAR Mechanism

A typical SAR system leverages a side-looking radar mounted on a moving platform to collect the backscattered signals from a region of interest (ROI). The collected data is used to reconstruct either two dimensional (2-D) or three dimensional (3-D) high resolution radar images depending on the trajectory of the SAR system. These SAR images, though look similar to optical images, show only the reflectivity of the ROI at a particular wavelength of the electromagnetic spectrum.

The motion of the radar antenna forms an increased synthetic aperture leading to a decreased synthetic beamwidth, overcoming the limited aperture available from a physically small antenna. Typical operation of a 2-D SAR systems are depicted in Fig. 3.1, where the radar systems transmit a wide band interrogating signal and obtains the impulse response of the ROI at K sampling points. These sampling points are equidistant with the spacing Δa chosen to meet the Nyquist criterion and avoid spatial aliasing.

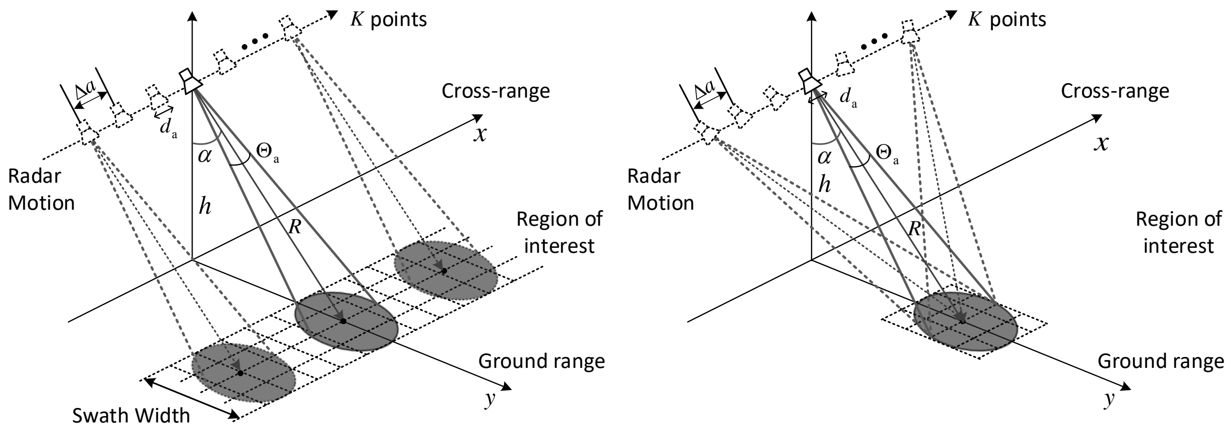

Figure 3.1: Basic operation schematics of 2-D SAR systems. (a) Stripmap SAR has a fixed antenna look angle α. (b) Spotlight SAR steers the antenna beam to constantly illuminate a single area.

3.2.2 Stripmap SAR and Spotlight SAR

There are many SAR imaging operation modes for different applications. Two conventional and most widely used modes are the Stripmap SAR and Spotlight SAR.

Stripmap SAR (see Fig. 3.1a) fixes the antenna orientation direction and look angle α when antenna moves. The antenna beam is fixed to one swath, and an image of a continuous strip will be reconstructed. In contrast, Spotlight SAR (see Fig. 3.1b) steers the antenna beam to the ROI center point and changes the look angle to always illuminate a single area when the radar platform moves along the trajectory. Because of the increased illumination time on the single area, the synthetic aperture length is also increased, hence improving the cross-range resolution compared to Stripmap SAR. But the drawback of Spotlight mode is that the ROI coverage size is much reduced.

The point scatterer model and image reconstruction algorithm discussed in this chapter can be applied in either mode. But experiments in the following chapters only demonstrate the use of Stripmap SAR.

3.2.3 2-D and 3-D SAR Selection

As shown in Fig. 3.1, a one-dimensional (1-D) scan of the swath produces a 2-D image with cross-range (along the x-axis) and ground range (along the y-axis) information. If the radar antennas also move in vertical direction (has 2-D motion) as illustrated in Fig. 3.2, then 3-D images of the ROI can be reconstructed to show cross-range, ground range, and elevation (along the z-axis) information [60, 61].

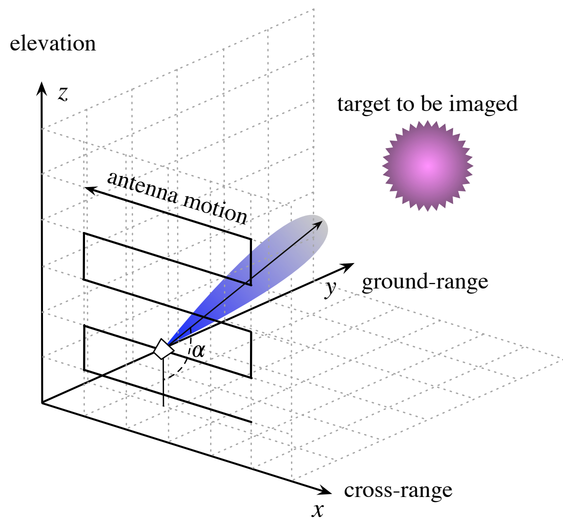

Figure 3.2: Basic operation schematic of a 3-D SAR system.

The SAR measurements implemented in Chapter 4 and Chapter 5 are 2-D stripmap SAR imaging of cooperative targets, while the SAR measurements of a quadcopter and its propellers in Chapter 6 and Chapter 7 are in 3-D stripmap mode.

3.2.4 Range and Cross-Range Resolution

Range is a measure of the LOS distance from the antenna to the target, and is determined by the time delay of the backscattered signal via cross-correlation of the radar transmit and receive signals. Thus, the range resolution δ_{r} is inversely proportional to the bandwidth B, and is given by

$$\delta_{\mathrm{r}} \approx \frac{c_0}{2B}, \tag{3.2}$$

where c_0 is the speed of light. And the ground range resolution δ_{gr} is

$$\delta_{\mathrm{gr}} = \frac{\delta_{\mathrm{r}}}{\sin\alpha}. \tag{3.3}$$

The cross-range (azimuth) resolution δ_{cr} denotes the ability of the SAR systems to resolve closely spaced scatterers in cross-range and is defined as the product of the synthetic beamwidth Θ_{SA} and range R. The synthetic beamwidth Θ_{SA} can be approximated by

$$\Theta_{\mathrm{SA}} \approx \frac{\lambda_0}{2L_{\mathrm{SA}}}, \tag{3.4}$$

with the length of synthetic aperture L_{SA} being the illumination length of the azimuth antenna beam, λ_0 being the wavelength of the signal center frequency, and the factor 2 representing the two-way path of transmission and reception. The illumination length L_{SA} can be calculated with the antenna beamwidth Θ_a or antenna aperture length d_a by

$$L_{\mathrm{SA}} = \Theta_a R = \frac{\lambda_0 R}{d_a}. \tag{3.5}$$

Therefore, the cross-range resolution δ_{cr} becomes [40]

$$\delta_{\mathrm{cr}} \approx \Theta_{\mathrm{SA}} R = \frac{\lambda_0 R}{2L_{\mathrm{SA}}} = \frac{d_a}{2}. \tag{3.6}$$

3.3 SAR Image Reconstruction

3.3.1 Adaption of the General Frequency Response Model

When reconstructing SAR images, it is assumed that the ROI can be approximated by a uniform grid of point scatterers each with a complex reflection coefficient. The discrete frequency response vector $\mathbf{y}_k$ obtained at radar position $k \in \{1, \ldots, K\}$ gives the backscatter response of these point scatterers. In many situations, the reflection coefficient of some point scatterers in the scene cannot always be time-invariant. Moreover, there can be cooperative targets, like backscatter tags, in the ROI trying to communicate with the radar system. For the backscatter tags, they usually have different modulation state combinations so the reflection coefficient of each point scatterer in the target has a limited set of complex values. Like it was proposed at the beginning of the chapter, the ROI can be seen as composing of many unmodulated targets (including the unchanging environment) and cooperative modulated targets depending on if their point scatterers are time-variant. The frequency response of ROI using the general frequency response model is then

$$y_{k,l}[i] = \overbrace{\sum_{n=1}^{N} \rho_{n,l}[i]\alpha_{k,l,n}^2 e^{-j2\pi f_l \frac{2\left\|\vec{\mathbf{R}}_k + \vec{\mathbf{r}_n}\right\|}{c_0}}}^{\substack{\text{cooperative modulated target and}\\ \text{unmodulated target response}}} + \nu_{k,l}[i].$$

To further adapt the model and generalize it for different SAR imaging systems, assume there are M point scatterers in the unmodulated targets that has constant reflectivity and N point scatterers in the cooperative targets of time-variant reflectivity, then the l-th discrete frequency sample of the k-th frequency response vector at the i-th modulation state (i being the sampling index) is given as

$$\begin{aligned} y_{k,l}[i] = &\overbrace{\sum_{m=1}^{M} \tilde{\rho}_m \tilde{\alpha}_{k,l,m}^{\mathrm{TX}} \tilde{\alpha}_{k,l,m}^{\mathrm{RX}} e^{-j2\pi f_l \frac{R\left(\mathbf{z}_k^{\mathrm{TX}}, \mathbf{z}_k^{\mathrm{RX}}, \tilde{\mathbf{z}}_m\right)}{c_0}}}^{\text{constant scatterer response}} \\ &+ \overbrace{\sum_{n=1}^{N} \rho_{n,l}[i] \alpha_{k,l,n}^{\mathrm{TX}} \alpha_{k,l,n}^{\mathrm{RX}} e^{-j2\pi f_l \frac{R\left(\mathbf{z}_k^{\mathrm{TX}}, \mathbf{z}_k^{\mathrm{RX}}, \mathbf{z}_n\right)}{c_0}}}^{\text{time-variant scatterer response}} + \nu_{k,l}[i], \end{aligned} \tag{3.7}$$

where $\tilde{\rho}_m$ is the complex reflection coefficient of the m-th constant scatterer, $\rho_{n,l}[i]$ is the frequency dependent complex reflection coefficient of the n-th time-variant scatterer, $\tilde{\alpha}^{\mathrm{TX}}_{k,l,m}$, $\tilde{\alpha}^{\mathrm{RX}}_{k,l,m}$, $\alpha^{\mathrm{TX}}_{k,l,m}$, $\alpha^{\mathrm{RX}}_{k,l,m}$ includes the one-way (transmit or receive) path loss and antenna gain, $R\left(\mathbf{z}^{\mathrm{TX}}_k, \mathbf{z}^{\mathrm{RX}}_k, \tilde{\mathbf{z}}_m\right)$ and $R\left(\mathbf{z}^{\mathrm{TX}}_k, \mathbf{z}^{\mathrm{RX}}_k, \mathbf{z}_n\right)$ are the two-way distance from radar position to that scatterer. The first part in the equation represents the entire constant scatterer response, the second part models tag backscatter, and $\nu_{k,l}[i]$ denotes the complex-valued measurement noise. This model works with both monostatic and bistatic radar configuration. The two-way distance from radar position to the scatterer can be calculated as

$$\begin{aligned} R\left(\mathbf{z}^{\mathrm{TX}}_k, \mathbf{z}^{\mathrm{RX}}_k, \tilde{\mathbf{z}}_m\right) &= ||\mathbf{z}^{\mathrm{TX}}_k - \tilde{\mathbf{z}}_m|| + ||\mathbf{z}^{\mathrm{RX}}_k - \tilde{\mathbf{z}}_m|| \\ R\left(\mathbf{z}^{\mathrm{TX}}_k, \mathbf{z}^{\mathrm{RX}}_k, \mathbf{z}_n\right) &= ||\mathbf{z}^{\mathrm{TX}}_k - \mathbf{z}_n|| + ||\mathbf{z}^{\mathrm{RX}}_k - \mathbf{z}_n|| \end{aligned}, \tag{3.8}$$

where $\mathbf{z}^{\mathrm{TX}}_k$ and $\mathbf{z}^{\mathrm{RX}}_k$ are the k-th positions of the TX and RX antenna phase centers respectively, $\tilde{\mathbf{z}}_m$ is the position of the m-th point scatterer, and $||\mathbf{z}||$ denotes the norm of the vector $\mathbf{z}$.

Concatenating all K frequency response samples with same sampling index but measured at different radar positions gives

$$\mathbf{y}[i] = \mathbf{H}\boldsymbol{\rho}[i] + \boldsymbol{\nu}[i], \tag{3.9}$$

where $\mathbf{y}[i] = \left[\mathbf{y}_1[i]^\dagger \dots \mathbf{y}_K[i]^\dagger\right]^\dagger$ with $(.)^\dagger$ being the complex conjugate transpose operator, $\boldsymbol{\rho}[i]$ consists of the reflection coefficients of all (constant and time-variant) point scatterers under the i-th modulation state, and $\boldsymbol{\nu}[i]$ is noise. The matrix $\mathbf{H}$ gives the dependence between the point scatterers and each measurement and can be calculated from the recorded radar positions, target positions, and measurement frequencies.

3.3.2 Reconstruction and Computational Complexity

The SAR reconstruction process finds an estimate of the reflection coefficient values $\hat{\boldsymbol{\rho}}[i]$ from the measurements $\mathbf{y}[i]$, hence

$$\hat{\boldsymbol{\rho}}[i] = \mathbf{A}\mathbf{y}[i], \tag{3.10}$$

where $\mathbf{A}$ is the reconstruction matrix.

As $\mathbf{H}$ is ill-conditioned in many cases (has a dimension of $K \times L \times (M+N)$), obtaining $\hat{\boldsymbol{\rho}}[i]$ by multiplying $\mathbf{y}[i]$ with e.g. the Moore-Penrose pseudo inverse $\mathbf{A} = \left(\mathbf{H}^\dagger\mathbf{H}\right)^{-1}\mathbf{H}^\dagger$, often does not give a stable solution. An alternative, which is used in this work, is to define $\mathbf{A} = \mathbf{H}^\dagger$ which gives the matched filter (or back-projection) reconstruction algorithm [53, 62].

The SAR image reconstruction process is shown in Fig. 3.3. The receiver collects the frequency response vectors of different sampling index for all measurement frequencies and at all radar positions, then saves all measurement vectors into a memory to form the measurement matrix $\mathbf{y}[i]$. On the other hand, the radar motion is recorded, along with the position coordinates of ROI point scatterers, the known antenna gain, and

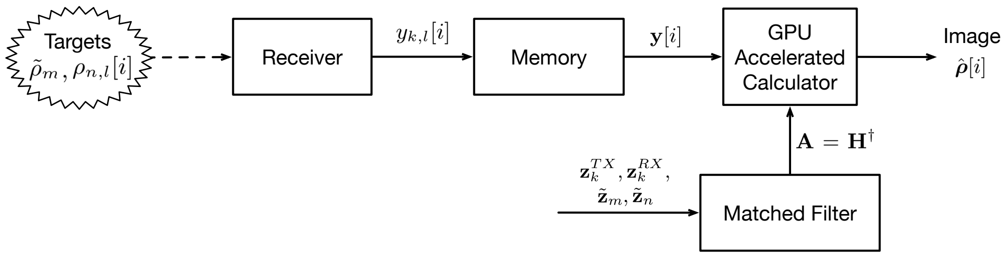

Figure 3.3: SAR image reconstruction process.

the operation frequencies to calculate the matched filer reconstruction matrix $\mathbf{A}$. Finally, the estimate of the reflection coefficient values $\hat{\boldsymbol{\rho}}[i]$ is calculated with a GPU accelerator in the computer. The reconstruction result $\hat{\boldsymbol{\rho}}[i]$ can be used for displaying the images of the ROI or can be used to demodulate the radar-target cooperation. A useful GPU acceleration algorithm can be found in [63].

By leveraging the Nvidia CUDA support of GPU in MATLAB, accelerated SAR reconstruction algorithms can be implemented for the matched filter reconstruction. We implement the GPU acclerated processing with a Nvidia GeForce GTX980 4GB graphics card. To minimize the GPU memory limitation, the following two block processing methods can be used:

1. Partitioning of the reconstruction output:

- Partitioning the matrix $\mathbf{H}$ in column-wise blocks:
  $\mathbf{H} = \left[\grave{\mathbf{H}}_1, \grave{\mathbf{H}}_2, \grave{\mathbf{H}}_3, \cdots\right]$,
  $\grave{\mathbf{A}}_j = \grave{\mathbf{H}}_j^\dagger$,
- Block-wise computing of the reconstruction output:
  $\hat{\boldsymbol{\rho}}_j[i] = \grave{\mathbf{A}}_j \mathbf{y}[i]$,
- Recomposing the output vector:
  $\hat{\boldsymbol{\rho}}[i] = \left[\hat{\boldsymbol{\rho}}_1^T[i], \hat{\boldsymbol{\rho}}_2^T[i], \hat{\boldsymbol{\rho}}_3^T[i], \cdots\right]^T$.

2. Partitioning the measurement input:

- Partitioning the measurement vector:
  $\mathbf{y}[i] = \left[\mathbf{y}_1^T[i], \mathbf{y}_2^T[i], \mathbf{y}_3^T[i], \cdots\right]^T$,
- Partitioning the measurement matrix in row-wise blocks:
  $\mathbf{H} = \left[\acute{\mathbf{H}}_1^T, \acute{\mathbf{H}}_2^T, \acute{\mathbf{H}}_3^T, \cdots\right]^T$,
- Block-wise computing of the reconstruction output:
  $\acute{\boldsymbol{\rho}}_j[i] = \acute{\mathbf{A}}_j^\dagger \mathbf{y}_j[i]$,

- Recomposing the output vector:
  $\hat{\boldsymbol{\rho}}[i] = [\hat{\boldsymbol{\rho}}_1[i]\hat{\boldsymbol{\rho}}_2[i]\hat{\boldsymbol{\rho}}_3[i]\cdots]$.

3.4 Chapter Conclusion

This Chapter adapts the point scatterer expression of a general modulated target to fit the application of synthetic aperture imaging. The frequency response from the imaging area of interest is fully studied with an emphasis on the motion of radar antennas. SAR image reconstruction methods and GPU accelerated calculation are discussed and they will be used in future chapters. When there are multiple samples collected at each radar position and each carrier frequency, the reconstruction results are a set of estimates of reflection coefficient values $\hat{\boldsymbol{\rho}}[i]$ ($i \in \{1, \ldots, I\}$). To just reconstruct an image of the ROI, any $\hat{\boldsymbol{\rho}}[i]$ can be equally used to get a reflectivity profile and it seems one sample at each radar position and each carrier frequency is enough. However, we will show how multiple sampling can help improve the signal noise ratio in Chapter 4. And other interest applications like cooperative target localization or discrimination and simultaneous backscatter communication can also benefit from the multiple sampling in SAR imaging.

Chapter 4

SIMULTANEOUS SAR IMAGING, LOCALIZATION, AND BACKSCATTER UPLINK WITH COOPERATIVE MODULATED TARGETS

This chapter is a modified version of [37]:

- **X. Fu**, A. Pedross-Engel, D. Arnitz, C. M. Watts, A. Sharma, and M. S. Reynolds, "Simultaneous Imaging, Sensor Tag Localization, and Backscatter Uplink Via Synthetic Aperture Radar," IEEE Transactions on Microwave Theory and Techniques, vol. 66, no. 3, pp. 1570 - 1578, Mar 2018.

This chapter, base on the preliminary work of microwave backscatter experimentation in Chapter 2 and SAR imaging infrastructure in Chapter 3, will combine them in one application and show even more functions could be realized using one microwave radio system. For this purpose, cooperative targets are designed to communicate room temperature information and their locations to a moving radar. An encoding scheme for the cooperative targets is proposed based on balanced orthogonal codes to avoid collisions among cooperative tags. It is seen that by applying the point scatterer model

$$\begin{aligned} y_{k,l}[i] = & \overbrace{\sum_{m=1}^{M} \tilde{\rho}_m \tilde{\alpha}^{\mathrm{TX}}_{k,l,m} \tilde{\alpha}^{\mathrm{RX}}_{k,l,m} e^{-j2\pi f_l \frac{R\left(\mathbf{z}^{\mathrm{TX}}_k, \mathbf{z}^{\mathrm{RX}}_k, \tilde{\mathbf{z}}_m\right)}{c_0}}}^{\text{constant scatterer response}} \\ & + \overbrace{\sum_{n=1}^{N} \rho_{n,l}[i] \alpha^{\mathrm{TX}}_{k,l,n} \alpha^{\mathrm{RX}}_{k,l,n} e^{-j2\pi f_l \frac{R\left(\mathbf{z}^{\mathrm{TX}}_k, \mathbf{z}^{\mathrm{RX}}_k, \mathbf{z}_n\right)}{c_0}}}^{\text{time-variant scatterer response}} + \nu_{k,l}[i], \end{aligned}$$

we are able to simultaneously achieve these goals:

- multiple access among tags;
- locating the positions of tags; tag-vs-tag and tag-vs-clutter discrimination;
- improving SNR during the localization due to noise averaging;
- high-resolution radar imaging of the unmodulated targets in the same environment.

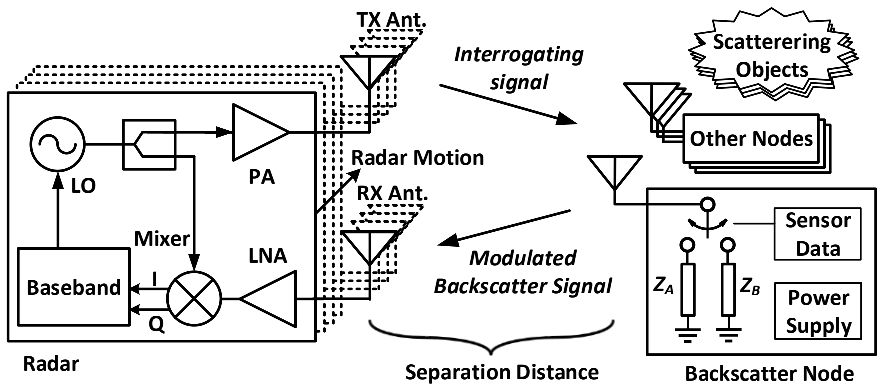

Figure 4.1: Conceptual backscatter-based sensor system using a synthetic aperture radar for imaging, tag localization, and sensor data uplink. The Backscatter nodes are cooperative targets to the radar system, and the scattering objects are unmodulated targets.

4.1 Introduction and Related Work

Modulated backscatter communication is already widely used in the billions of passive (battery-free) radio frequency identification (RFID) tags produced and sold every year. Backscatter devices do not need to generate their own radio frequency carrier. They communicate by reflecting an interrogating signal from an external device such as a radar. The carrier signal is modulated by switching the reflection coefficient presented by the tag to its antenna. Thus, backscatter tags do not contain power hungry frequency synthesizers or RF amplifiers, minimizing tag power consumption and complexity. As shown in Fig. 4.1, the simplest form of a backscatter data uplink can be achieved with only a single RF switch alternately connecting the tag antenna to one of two different impedances, Z_A and Z_B.

The pervasiveness of low cost passive RFID tags, and the increasing read-range of backscatter systems, give rise to a growing uncertainty of the spatial context of the system, including the locations of the tags (cooperative targets), as well as the un-tagged scattering objects (unmodulated targets) in the environment. This stimulates academic and commercial interest in localization techniques that can simultaneously locate both tagged and un-tagged objects.

In the literature, sensor tag localization has been achieved using various approaches, including received signal strength indicator (RSSI) based approaches [64–66], angle of arrival (AoA) [67, 68], time of arrival (ToA), and time difference of arrival (TDoA) measurements [69, 70]. Each of these approaches has an associated cost and complexity trade-off. For example, RSSI-based localization methods use easily-observed received signal magnitude from low cost off-the-shelf sensor tags, but RSSI methods are vulnerable to multipath effects. The AoA can be measured by antenna beam steering or arrays which require complex and expensive hardware. ToA and TDoA require highly accurate synchronized clocks, resulting in significant cost and complexity issues.

As introduced in Chapter 3, though SAR systems are most seen in earth remote sensing and military surveillance, they are also suggested for target positioning in some cases. For example, SAR approaches have previously been used for holographic localization of UHF backscatter transponders [58, 59]. Based on a coherent superposition of phase values taken along a synthetic aperture, the calculated holographic image yields a spatial probability density function of possible tag positions. The method shows accurate lateral locations, however, due to the limited bandwidth in the UHF spectrum, the distance error and holographic image resolution are at decimeter levels.

This chapter presents an extension of synthetic aperture radar (SAR) techniques, along with using the point scatterer expression of modulated targets to enable simultaneous radar imaging, sensor tag localization, and backscatter-based data uplink from multiple sensor tags in a cluttered environment. Potential applications of this work include interfacing backscatter-based sensor tags with radars on robots, unmanned vehicles, and handhold RFID readers.

By coherently processing both the phase and amplitude of backscatter signals over a much wider bandwidth (10 – 13 GHz) compared to the narrow band measurement in UHF, the reconstruction resolution and localization error are reduced to centimeter level. Sensor tag packets, containing balanced orthogonal codes to enable straightforward tag-vs-clutter and tag-vs-tag discrimination, are used for backscatter communication during the radar motion and help to improve signal-to-noise ratio (SNR) during localization. A SAR measurement collecting and processing real temperature data packets is implemented. The effects of antenna phase center offsets are considered when processing measurement results. With a phase center calibration of radar and tag antennas, the reconstructed images of scattering objects and localization maps of tags can be achieved with errors of less than 1 cm.

4.2 Model of Simultaneous Imaging, Localization, and Backscatter Uplink

As a cooperative target, the backscatter sensor tag encodes sensor data and uses it to drive an RF modulator, which is often as simple as an RF switch having two or more distinct impedances. Different modulation states are thus achieved when the termination of a tag antenna changes among different impedances. In this chapter, the cooperative tags are switching their antennas between a short and an open load to form a BPSK modulation scheme. The backscatter encoding scheme, the target frequency response model, and SAR reconstruction discussed in this section can also be applied to other modulation schemes using different multiple access techniques. A signal processing flow chart of the backscatter signal is shown in Fig. 4.2.

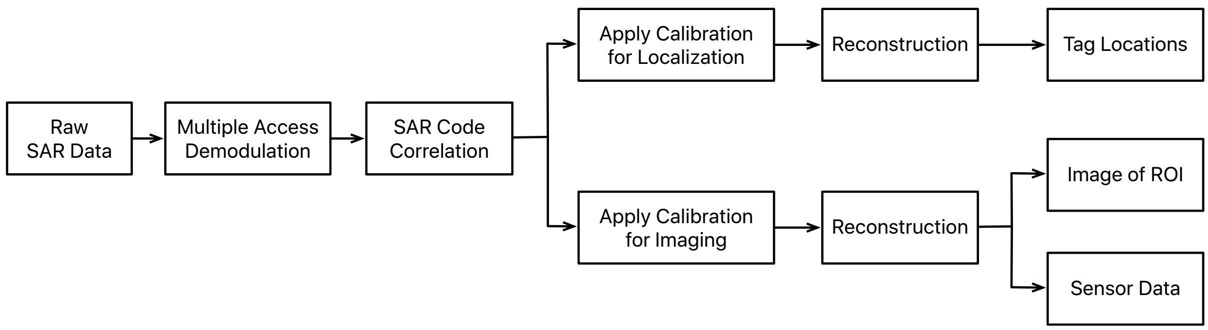

Figure 4.2: Signal processing pipeline for simultaneous radar imaging, sensor tag localization, and backscatter uplink.

For the proposed application, the SAR frequency response model (Eq. 3.7) and reconstruction algorithms derived in Chapter 3 are used. When there are multiple samples at each radar position and each carrier frequency, there is a set of reflections coefficient estimates $\hat{\boldsymbol{\rho}}[i]$ ($i \in \{1, \ldots, I\}$) obtained from the measurement vectors $\mathbf{y}[i] = \left[\mathbf{y}_1[i]^\dagger \, \ldots \, \mathbf{y}_K[i]^\dagger\right]^\dagger$, with $(.)^\dagger$ being the complex conjugate transpose operator.

To demodulate sensor data sequences and localize tags from the backscattered frequency responses of ROI, every tag packet contains an *a priori* known preamble consisting of several SAR code bits uniquely assigned for imaging and localization, in addition to the sensor data, which is usually unknown *a priori*. The SAR preamble codes $\{\mathbf{c}_n\}$ can be used to distinguish individual tags and separate them from the background. To do this efficiently, the code words should be mutually orthogonal and balanced, containing the same number of +1 and -1 symbols. In the simplest 2 tag (J=2) case, the SAR codes can be defined as

$$\mathbf{c}_j = \begin{cases} [+1, -1, +1, -1]^\dagger, & j = 1 \\ [+1, +1, -1, -1]^\dagger, & j = 2 \end{cases} \tag{4.1}$$

for the first four bits in the tag packets. Then each tag point scatterer can have only two different reflection coefficient values, $\rho_{\{-1,1\},n,l}$. The frequency response vector at k-th radar position becomes

$$\mathbf{y}_k[i] = \mathbf{y}_k^{\mathrm{UM}} + \mathbf{y}_{\{-1,+1\},k}^{j=1} + \mathbf{y}_{\{-1,+1\},k}^{j=2} + \nu_k[i], \tag{4.2}$$

where $\mathbf{y}_k^{\mathrm{UM}}$ is the response from the unmodulated targets, $\mathbf{y}_{\{-1,+1\},k}^{j=1}$ and $\mathbf{y}_{\{-1,+1\},k}^{j=2}$ are the frequency responses from Tag 1 and Tag 2 respectively. There are four combinations of them, each is called a modulation state combination. We can see that, for a 1 sample/bit measurement, four samples are enough to cover all the modulation states combinations at each radar position.

If the samples measured at different radar positions are synchronized to the SAR codes sequence, the two-tag measurement vectors can be constructed as

$$\begin{aligned}\mathbf{y}[1] =& \mathbf{y}^{\mathrm{UM}} + \mathbf{y}_{+1}^{j=1} + \mathbf{y}_{+1}^{j=2} + \nu[1] \\ \mathbf{y}[2] =& \mathbf{y}^{\mathrm{UM}} + \mathbf{y}_{-1}^{j=1} + \mathbf{y}_{+1}^{j=2} + \nu[2] \\ \mathbf{y}[3] =& \mathbf{y}^{\mathrm{UM}} + \mathbf{y}_{+1}^{j=1} + \mathbf{y}_{-1}^{j=2} + \nu[3] \\ \mathbf{y}[4] =& \mathbf{y}^{\mathrm{UM}} + \mathbf{y}_{-1}^{j=1} + \mathbf{y}_{-1}^{j=2} + \nu[4]\end{aligned}. \tag{4.3}$$

And it will be shown that, with such four samples in SAR measurements, single tag localization, simultaneous two-tag localization, images of all scattering objects, and an image for just the un-modulated targets can be achieved by applying different SAR code bits to the reconstruction process. And by using more bits of balanced orthogonal SAR codes, multiple-tag localization and discrimination, and simultaneous imaging of the scattering objects can be achieved in a same way. Next, the SAR reconstructions of the general multi-tag cases will be discussed. In localization application, the examples of two-tag case are also given.

4.2.1 Single Tag Localization

With this SAR reconstruction process given before

$$\hat{\boldsymbol{\rho}}[i] = \mathbf{A}\mathbf{y}[i],$$

the reconstruction of the j-th tag can be obtained by

$$\hat{\boldsymbol{\rho}}_j = \mathbf{A}\mathbf{Y}\mathbf{c}_j, \tag{4.4}$$

where

$$\mathbf{Y} = \left[\mathbf{y}[1],\, \mathbf{y}[2],\, \ldots,\, \mathbf{y}[I]\right], \tag{4.5}$$

and $\hat{\boldsymbol{\rho}}_j$ is the reflection coefficient estimate of the j-th tag. Due to the orthogonality property of the codes, the contributions of other tags are canceled. Constant scatterer responses from the environment are also canceled due to the balance property.

When there are only two tags, the reflection coefficient estimate of Tag 1 is

$$\begin{aligned}\hat{\boldsymbol{\rho}}_1 = \mathbf{A}\mathbf{Y}\mathbf{c}_1 &= \mathbf{A}[\mathbf{y}[1],\, \mathbf{y}[2],\, \mathbf{y}[3],\ \mathbf{y}[4]][+1, -1, +1, -1]' \\ &= \mathbf{A}[\mathbf{y}[1] - \mathbf{y}[2] + \mathbf{y}[3] - \mathbf{y}[4]] \\ &= \mathbf{A}[\mathbf{y}^{\mathrm{UM}} + \mathbf{y}_{+1}^{j=1} + \mathbf{y}_{+1}^{j=2} + \nu[1] \\ &\quad -\mathbf{y}^{\mathrm{UM}} - \mathbf{y}_{-1}^{j=1} - \mathbf{y}_{+1}^{j=2} - \nu[2] \\ &\quad +\mathbf{y}^{\mathrm{UM}} + \mathbf{y}_{+1}^{j=1} + \mathbf{y}_{-1}^{j=2} + \nu[3] \\ &\quad -\mathbf{y}^{\mathrm{UM}} - \mathbf{y}_{-1}^{j=1} - \mathbf{y}_{-1}^{j=2} - \nu[4]] \\ &= \mathbf{A}[2\mathbf{y}_{+1}^{j=1} - 2\mathbf{y}_{-1}^{j=1} + \nu[1] - \nu[2] + \nu[3] - \nu[4]],\end{aligned} \tag{4.6}$$

We can see that the responses from Tag 2 and the unmodulating environment sampled at different times are cancelled. It is also noted that signal-to-noise ratio (SNR) during the reconstruction is increased due to the inherent noise averaging. Similarly, the reflection coefficient estimate of Tag 2 is obtained as

$$\hat{\boldsymbol{\rho}}_2 = \mathbf{AYc}_2 = \mathbf{A}\left[2\mathbf{y}_{+1}^{j=2} - 2\mathbf{y}_{-1}^{j=2} + \nu[1] - \nu[2] + \nu[3] - \nu[4]\right]. \tag{4.7}$$

Therefore, by correlating the SAR code bits with the measurement samples, each single tag can be reconstructed separately.

4.2.2 Simultaneous Multi-tag Localization

By multiplying $\mathbf{Y}$ with the sum of multiple codes, e.g. $\mathbf{c}_j \in \mathcal{C}$, where $\mathcal{C}$ is the set of corresponding codes, a combined reconstruction of these tags can be obtained. Hence,

$$\hat{\boldsymbol{\rho}}_{\text{all}} = \mathbf{AY} \sum_{\mathbf{c}_j \in \mathcal{C}} \mathbf{c}_j, \tag{4.8}$$

where $\hat{\boldsymbol{\rho}}_{\text{all}}$ is the combined reflection coefficient estimate of these tags.

For the two-tag case, the reflection coefficient estimate of Tag 1 and Tag 2 together can be obtained by

$$\begin{aligned}\hat{\boldsymbol{\rho}}_{1 \text{ and } 2} &= \mathbf{A}\left[\mathbf{y}[1], \mathbf{y}[2], \mathbf{y}[3], \mathbf{y}[4]\right]([+1,-1,+1,-1]' + [+1,+1,+1,-1]') \\ &= \mathbf{A}\left[2\mathbf{y}[1] - 2\mathbf{y}[4]\right] \\ &= \mathbf{A}\left[2\mathbf{y}_{+1}^{j=1} + 2\mathbf{y}_{+1}^{j=2} - 2\mathbf{y}_{-1}^{j=1} - 2\mathbf{y}_{-1}^{j=2} + 2\nu[1] - 2\nu[4]\right].\end{aligned} \tag{4.9}$$

The signal-to-noise ratio (SNR) during the reconstruction is also increased due to noise averaging.

4.2.3 Imaging of the Unmodulated Environment

To cancel the reflection of tags under different states and only keep the measurements of time-invariant scatters corresponding to the unmodulating environment, the code $\mathbf{c}^{\text{UM}}$ where all elements are $+1$ can be used, hence

$$\hat{\boldsymbol{\rho}}_{\text{un-modulated}} = \mathbf{AYc}^{\text{UM}}, \tag{4.10}$$

where $\hat{\boldsymbol{\rho}}_{\text{un-modulated}}$ denotes the reflection coefficient estimates of all scattering objects in the measurement except any tags.

4.2.4 Imaging All Scattering Objects

With $\mathbf{c}^{\text{SO}}$ being a unit vector, an image containing all of the scattering objects in the ROI can be reconstructed, hence

$$\hat{\boldsymbol{\rho}}_{\text{obj}} = \mathbf{AYc}^{\text{SO}}, \tag{4.11}$$

where $\hat{\boldsymbol{\rho}}_{\text{obj}}$ denotes the reflection coefficient estimate of all scattering objects in the measurement.

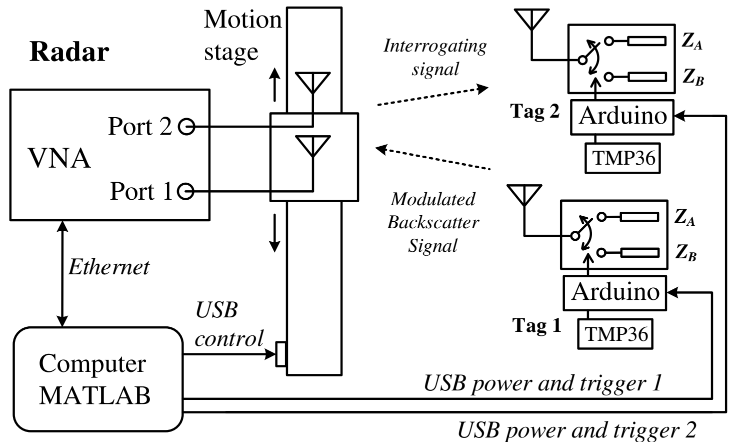

Figure 4.3: Schematic of the experimental SAR setup with two sensor tags.

4.3 Indoor Measurements

A proof-of-concept laboratory demonstration has been constructed using a combination of lab instrumentation with added custom hardware and firmware as shown in Fig. 4.3.

The SAR system consists of an Agilent N5222A vector network analyzer (VNA) providing transmitter and receiver functions. Two ultra-wideband planar bow-tie antennas, same as in Chapter 2, are mounted on a 3D-printed platform affixed to a Newport IMS600 motion stage, yielding a collocated bistatic SAR configuration. The VNA data acquisition and antenna platform motion are controlled by a PC running MATLAB through standard commands for programmable instruments (SCPI) scriptting.

4.3.1 Sensor Tag Hardware

Two custom designed tags were constructed as cooperative targets for the experiment. They are improved designs of the tags introduced in Chapter 2 because a better modulation factor is achieved with a much lower-priced switch.

As shown in Fig. 4.4, each sensor tag consists of:

- An Analog Devices TMP36 analog temperature sensor. The TMP36 temperature sensor provides a voltage output that is linearly proportional to temperature over the range of $-40\,°\mathrm{C}$ to $+125\,°\mathrm{C}$ with an accuracy of $\pm 1\,°\mathrm{C}$. Its voltage operation range is 2.7 V to 5.5 V.

- A bowtie antenna with a size of 3.5 cm $\times$ 3 cm, a maximum gain of 6 dBi, and a -10 dB bandwidth from 9.6 GHz to 13.1 GHz [13].

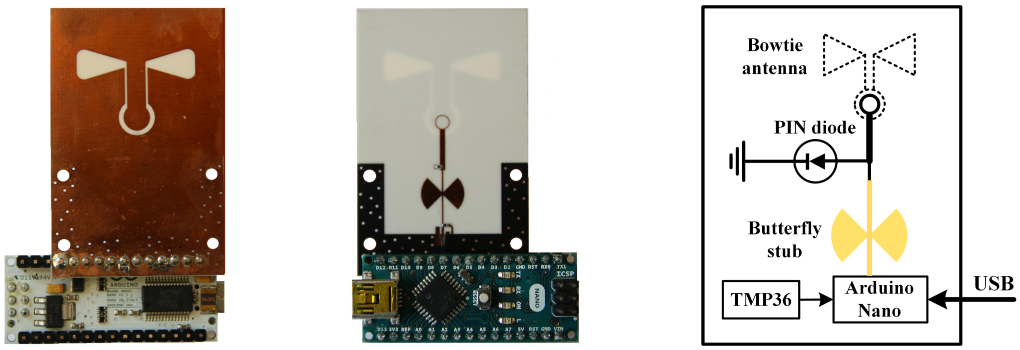

(a) (b) (c)

Figure 4.4: The (a) front side, (b) back side, and (c) schematic of the sensor tag.

- A PIN diode RF switch. The RF switch uses a M/A-COM MA4AGFCP910 PIN diode, with a low RC product (series resistance of 5 Ω, capacitance of 0.025 pF) and a 2 nanosecond switching speed. A single positive bias voltage generated by an Arduino Nano was added to the PIN anode through a butterfly stub decoupling network while the PIN cathode was grounded. Thus short and open loads were easily achieved with forward bias and reverse bias respectively. The reflection coefficients of the two modulation states measured at the antenna reference port are shown in Fig. 4.5, where $|\rho_A| = 0.838$ and $|\rho_B| = 0.945$ over 10-11 GHz band.

- An Arduino Nano processor module based on the Atmel ATMega328 microcontroller with a clock frequency of 16 MHz. The Arduino Nano is directly soldered on the RF circuit board (0.5 mm thick RO4003C substrate). It generates a logic level voltage to control the switch via a digital output pin and reads the TMP36 temperature sensor via an analog input pin.

From Fig. 4.3, the temperature readings are triggered simultaneously by the PC running MATLAB. Given the 16 MHz clock rate of the ATMega328, the maximum possible data rate is $\approx$ 1 Mbps, but due to the slow response of the VNA and MATLAB control software, only 1 b/s is achieved in the proof-of-concept. Given the much faster data acquisition rate possible with dedicated radar hardware, the system data rate could easily approach or even exceed the 1 Mbps that a simple microcontroller-based tag could supply.

4.3.2 Data Packet Structure and Multiple Access Encoding

Given the slow data acquisition speed of the VNA and the MATLAB control software, continuous data acquisition and real-time processing are not practical with the lab setup. Instead, all functions are triggered

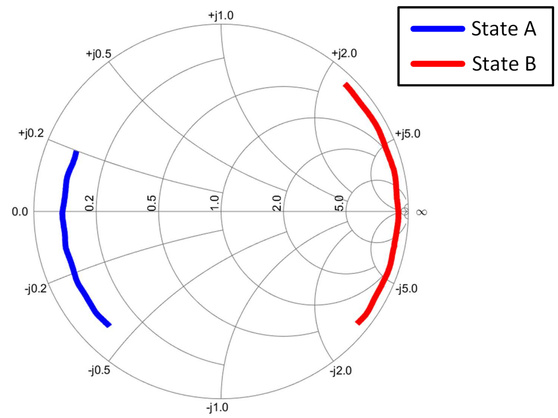

Figure 4.5: Measured reflection coefficients of the PIN switch over 10-11 GHz.

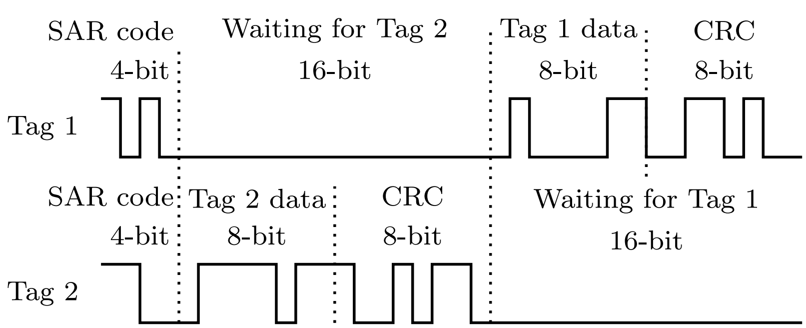

Figure 4.6: Format of the tag data packets showing sub-frames for SAR imaging, sensor data, and CRC.

in sequence by the PC running MATLAB. A preamble indicating the start of each packet is therefore not necessary in this demonstration.

Fig. 4.6 gives an example of an encoded packet sent by both tags. The portions of the packet used for SAR reconstruction ("SAR code") are orthogonally coded as discussed in Section 4.2; this orthogonal coding is used in a CDMA-like approach to mitigate tag collisions during the imaging and localization processes. Data transfer is performed via a TDMA approach. The voltage output of TMP36 is converted into 8-bit binary data followed by 8-bit cyclic redundancy check (CRC) error-detecting code. While Tag 2 transmits its 16-bit data frame, Tag 1 keeps a fixed modulation state, and vice versa. If the sampling rate of the radar system is controlled to be 1 sample/bit, the response $\mathbf{Y} = \left[\mathbf{y}[1], \mathbf{y}[2], \mathbf{y}[3], \mathbf{y}[4]\right]$ is used for SAR reconstructions, and vectors $\left[\mathbf{y}_k[5], \cdots, \mathbf{y}_k[36]\right]$ are used to retrieve the sensor data and its associated CRC.

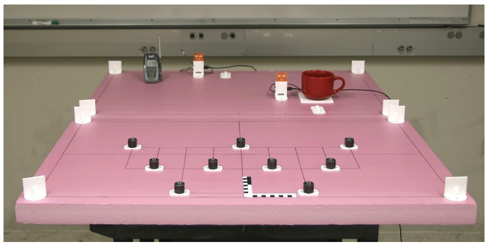

(a) ROI

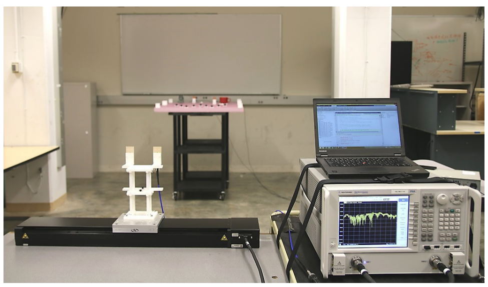

(b) Environment

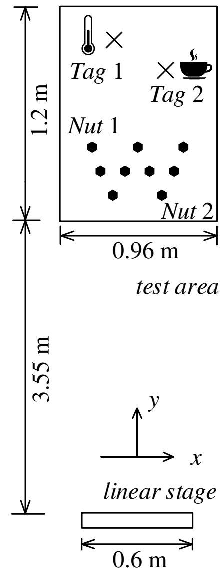

(c) Geometry

Figure 4.7: Photo of (a) the imaging region of interest (ROI) and (b) the cluttered measurement environment. Sub-figure (c) shows the geometry of the imaging area and the linear stage motion.

4.3.3 Measurement Setup and Implementation

Indoor measurements were carried out in a cluttered lab environment as shown in Fig. 4.7. The imaging ROI (Fig. 4.7a) was floored with a 120 cm × 96 cm RF-transparent Styrofoam sheet and placed at a range of $y = 3.5$ m (Fig. 4.7c). To serve as unmodulated targets, nine 5/8”-18 steel hex nuts were added in a “W” shape with a cross-range spacing of 8 cm and a range spacing of 15 cm. Two sensor tags were also placed in the ROI, where Tag 1 recorded room temperature, while Tag 2 measured the temperature of a cup of coffee using its TMP36 sensor attached to the coffee mug.

During the experiment, the motion stage moves the collocated bistatic TX-RX antennas to form a synthetic aperture along $x = [-0.3,\ 0.3]$ m. To meet the Nyquist criterion and avoid spatial aliasing, the sampling distance must be smaller than half of the antenna aperture [38]. An over-sampled step size of 4 mm is used in our data collection. At each motion step, the PC sends a trigger to each sensor tag. In response, each Arduino Nano reads the temperature sensor and formats its output into the 36 bit packet format of Fig. 4.6. The tag’s modulating switch is driven at a rate of 1 bps. The VNA measures the TX-RX response at 301 discrete frequencies over the 10–13 GHz band. After the whole packet is received, the motion stage moves to the next sampling location. Finally, the measurement data is post-processed in MATLAB.

4.4 Phase Center Calibration for Imaging and Localization

As the frequency response expression of all the ROI point scatterers discussed in Chapter 3 (Eq. 3.7) shows, the delay between received and transmitted signals is proportional to the two-way distance R from the radar antenna phase centers to the scattering object. Since the phase center of an antenna is not necessarily coincident with its physical center, the offset is an unwanted addition to R that results in reconstruction error. Therefore, the antenna phase center offset must be estimated during the calibration process and subtracted from the exponential term of Eq. 3.7 [71].

4.4.1 TX-RX Phase Center Correction

In the imaging scenario, the tags are assumed to be constant-scattering. The TX-RX phase center offset can be estimated by comparing the peak in the observed impulse response corresponding to a scattering object with its actual (tape measured) round-trip distance. Figures 4.8a and 4.8b show the TX-RX phase center calibration setup using a known target, a 15 cm $\times$ 10 cm metal plate fixed parallel to the TX-RX antennas. The front surface of the plate is $D = 45.9$ cm away from the antenna plane. The bistatic separation distance between the TX and RX antennas is $d = 11.8$ cm. Thus, the actual round-trip distance of the plate is $R' = 92.56$ cm.

The network analyzer was configured to measure S_{21} from 10 GHz to 13 GHz with a step size of 10 MHz, and its built in calibration process was used to move the reference plane to the far end of the VNA cables. By zero-padding the S_{21} data and performing an inverse fast Fourier transform, a very smooth impulse response is observed, as shown in Fig. 4.8c. The first peak, found at 24 cm, corresponds to the unwanted direct coupling between antennas. The second peak, found at 104.59 cm, corresponds to the electrical round-trip distance. The difference between this value and the actual round-trip distance gives a measured TX-RX phase center offset of 12.03 cm.

4.4.2 Tag Phase Center Correction

When localizing a backscatter based tag, the phase center of the tag antenna and any transmission line length on the tag must also be corrected. This was done with the setup shown in Fig. 4.8d and Fig. 4.8e. The VNA takes two S_{21} measurements for the two tag states over 10–13 GHz in 10 MHz steps. By subtracting the complex S_{21} data of two states and applying zero-padding, the tag impulse response is obtained as shown in Fig. 4.8f. The tag antenna appeared at 115.25 cm, which is 10.66 cm farther than the plate as a result of tag antenna phase center offset. The three antennas require a sum of 22.69 cm in total phase center correction. This additional electrical length can be used for single tag or multiple tags localization to correct the phase of the received backscatter signals.

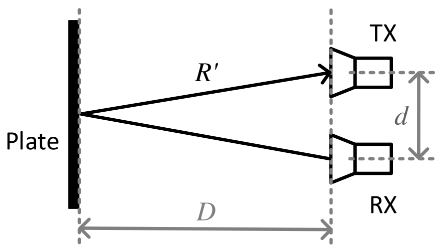

(a) TX-RX phase center correction setup

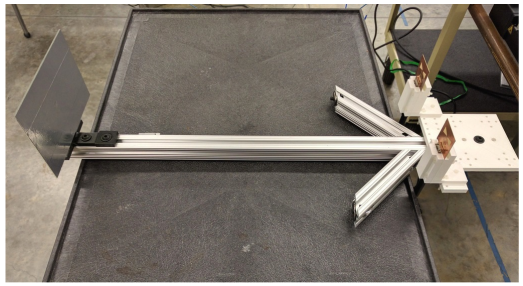

(b) TX-RX correction experimental setup

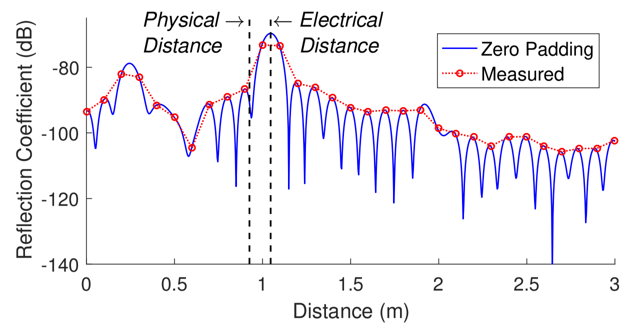

(c) Measured plate round trip distance

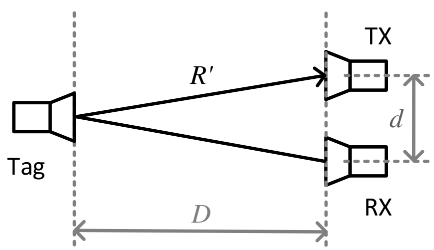

(d) Tag phase center correction setup

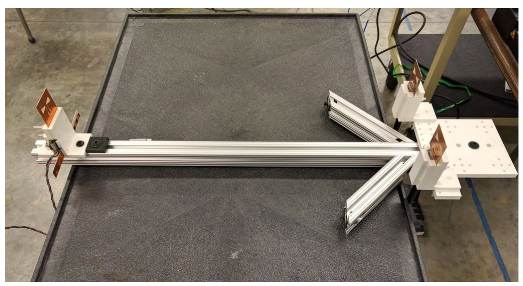

(e) Tag correction experimental setup

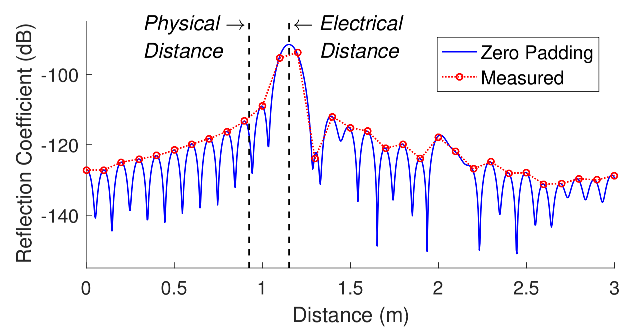

(f) Measured tag round trip distance

Figure 4.8: Experimental setups and measured data used for calibration of TX-RX phase center and tag phase center.

4.5 Imaging, Localization, and Backscatter Uplink Results

To process the data gathered during the SAR experiment, all of the frequency response vectors $\mathbf{y}_k[i]$ obtained during each of the 36 data symbol periods, $i \in \{1, \ldots, 36\}$, and from all radar positions $k \in \{1, \ldots, 151\}$ are concatenated to form the SAR measurement vector $\mathbf{y}[i]$ as defined by (3.9). Since the first 4 samples at each radar position represent the orthogonal SAR code words, the response $\mathbf{Y} = \left[\mathbf{y}[1], \mathbf{y}[2], \mathbf{y}[3], \mathbf{y}[4]\right]$ is used for imaging and localization reconstructions as discussed in Section 4.2, and the remaining 32 samples are used to retrieve the sensor data and its associated CRC.

4.5.1 Imaging Results

When reconstructing images of scattering objects, the TX-RX phase center calibration result is used to compensate the phase center in $\mathbf{Y}$. After multiplying $\mathbf{Y}$ with $\mathbf{c}^{\mathrm{UM}}$, the image of the un-tagged environment can be obtained as shown in Fig. 4.9a, which depicts the ROI excluding the tags, which are suppressed because the SAR code words are balanced and thus zero-mean. This ROI includes very high magnitude scattering from large objects in the background, such as the magnetic white board, electrical conduit, and a metallic closet that form the background of the scene. This high magnitude scattering causes a dynamic range challenge when the objects of interest are small scatters (such as the hex nuts and tags in our example).

To mitigate the effects of background clutter, background subtraction is performed after reconstructing the image using $\mathbf{c}^{\mathrm{SO}}$. The resulting image of all scattering objects depicted in Fig. 4.9b clearly shows the two tags and nine nuts aligned in a "W" shape with the reflectivity normalized and represented on a log scale. The scattering response of Tag 2 is stronger because it has a larger radar cross section than the hex nuts, and is closer to the motion stage than Tag 1. As a contrast, the ground truth positions of the two sensor tags and eight hex nuts are shown in Fig. 4.9c.

4.5.2 Localization Results

To localize the tags, the phase center calibration results are first used to correct the data in $\mathbf{Y}$. Figs. 4.9d to 4.9f show single tag and two-tag localization results. An improved SNR is achieved because the background clutter is canceled due to the balanced SAR code word, so an additional background subtraction is not necessary. With the center point of radar antenna motion forming the origin of each plot, the peak PSF value of Tag 1 is found to be at -0.154 m in cross-range direction and at 4.698 m in range direction. The 3 dB pulse width of the Tag 1 PSF shows $\delta_{\mathrm{r}} = 4.7$ cm and $\delta_{\mathrm{cr}} = 9.1$ cm. Note that the theoretical resolutions are calculated as $\delta_{\mathrm{r}} = 5$ cm and $\delta_{\mathrm{cr}} = 10.2$ cm using Eq. 3.2 and Eq. 3.6, respectively. Similarly, Tag 2 is localized in cross-range at 0.147 m and in range at 4.41 m with $\delta_{\mathrm{r}} = 4.3$ cm and $\delta_{\mathrm{cr}} = 8.3$ cm.

A detailed comparison of imaging and localization results with the calculated ground truth of two tags

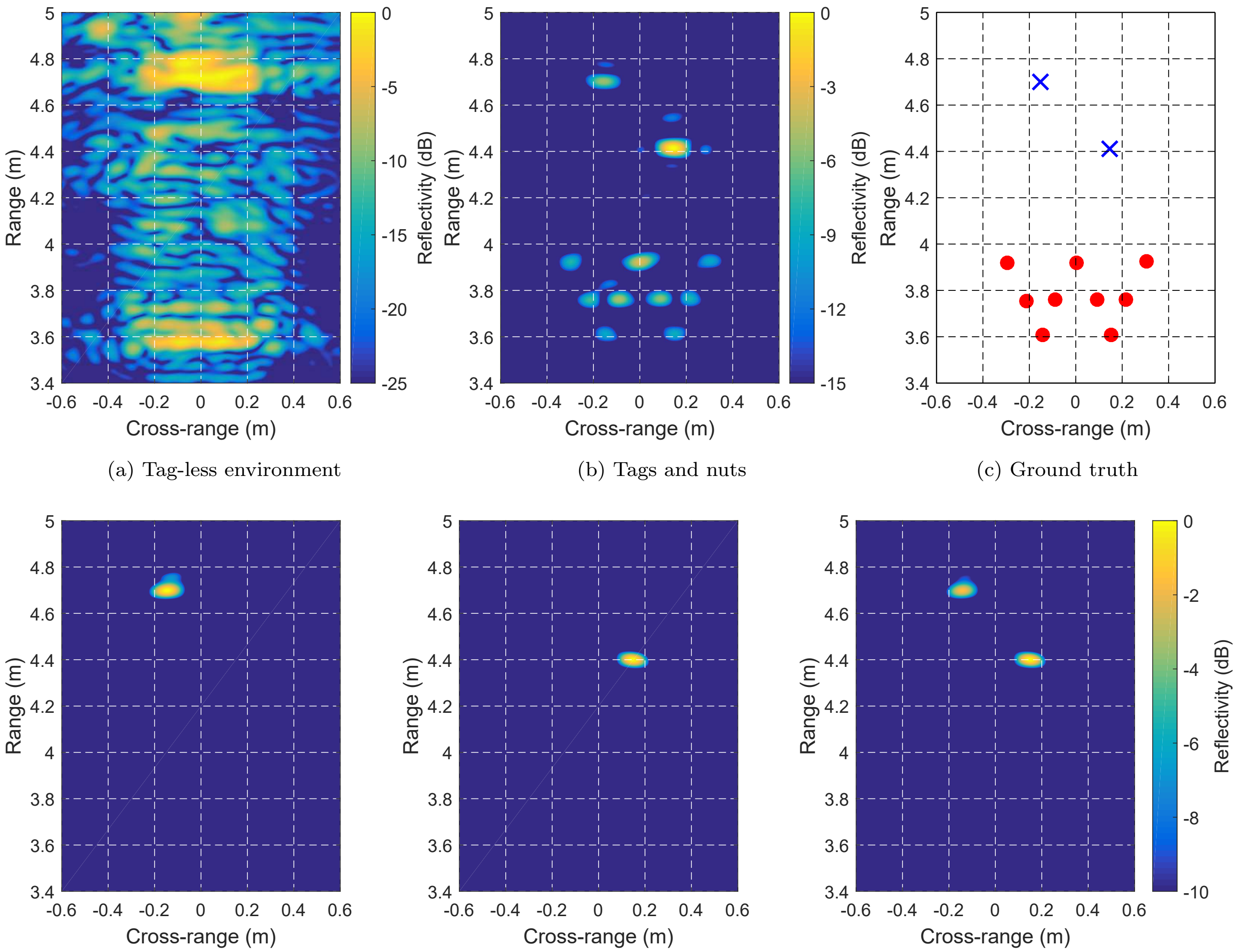

(a) Tag-less environment (b) Tags and nuts (c) Ground truth

(d) Tag 1 only (e) Tag 2 only (f) Tag 1 and Tag 2 together

Figure 4.9: SAR images reconstructed with different processing approaches, showing the ability to separate tags from each other and from the un-tagged scatterers.

Table 4.1: Comparison of measurement results with the ground truths

Object	Imaging (m) (x, y)	Tag Localization (m) (x, y)	Ground Truth (m) (x, y)
Tag 1	(-0.154, 4.698)	(-0.143, 4.696)	(-0.150, 4.689)
Tag 2	(0.147, 4.410)	(0.151, 4.397)	(0.150, 4.401)
Nut 1	(-0.294, 3.919)	–	(-0.289, 3.910)
Nut 2	(0.145, 3.608)	–	(0.149, 3.600)

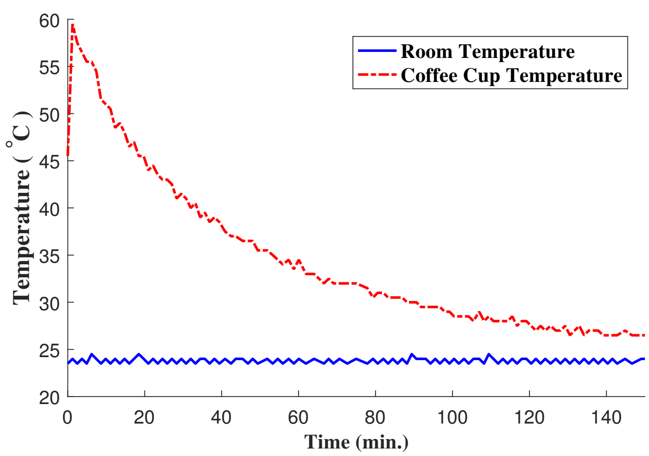

Figure 4.10: Measured time series of room temperature (Tag 1) and coffee cup temperature (Tag 2).

and two hex nuts (opposite corners of the letter "W" per Fig. 4.7) is shown in Table. 4.1. The three type of results agree well to the centimeter level. The localized results have a maximum 2-D offset of 1.5 cm when compared to imaging results and 1 cm offset compared to the ground truth.

4.5.3 Backscatter Data Uplink Results

Finally, the frequency response vectors $\left[\mathbf{y}_k[5], \cdots, \mathbf{y}_k[36]\right]$ at each radar position are demodulated to recover the sensor data. Fig. 4.10 shows the room temperature as measured by Tag 1 and the coffee cup temperature as measured by Tag 2. Due to the slow data acquisition rate of the laboratory SAR system, this measurement was performed over a 150 minute interval. During this time, the room temperature was found to fluctuate around 23.5 °C, and the cup of coffee cooled from 60 °C to 28 °C. The maximum reading range is approximately 5 m, limited by the room size. No CRC errors are detected in the demodulated data indicating a good link quality.

4.6 Chapter Conclusion

This chapter uses the point scatterer expression on cooperative modulated targets and reports experimental results of simultaneous imaging tagged and un-tagged objects, localizing sensor tags, and reading sensor data via backscatter. The coherent processing of backscatter signals over a synthetic aperture formed by a moving radar provides new possibilities for e.g. unmanned vehicles and handheld radar devices.

To fulfill the three purposes, a tag packet data structure is designed around balanced, mutually orthogonal codes to enable tag separation in SAR reconstruction. This approach allows the reconstruction of SAR images containing only cooperative targets (or combinations thereof), unmodulated objects, or the cluttered environment. An indoor experiment over 10–13 GHz is presented leveraging a VNA as a radar, and two sensor tags. After compensating for tag and radar antenna phase center offset, the reconstructed image of scattering objects is obtained and shown to exhibit a range resolution of 4.7 cm and a cross-range resolution of 9.1 cm at a range of 4.7 m. The SAR code words allow separation of multiple tags as well as enhancing SNR by 6 dB due to noise averaging. The localization results agree well with ground-truth tag positions to an error of approximately 1 cm.

Chapter 5

MULTIPATH EXPLORATION IN SIMULTANEOUS RADAR IMAGING AND COOPERATIVE TARGET LOCALIZATION

In this chapter, we consider the multipath components in the general model of system frequency response

$$y_{k,l}[i] = \overbrace{\sum_{n=1}^{N} \rho_{n,l}[i] \, \alpha^2_{k,l,n}[i] \, e^{-j2\pi f_l \frac{2\left\|\vec{\mathbf{R}}_{k}[i] + \vec{\mathbf{r}_n}[i]\right\|}{c_0}}}^{\text{general modulated target response}} + \text{Multipath}_{k} + \nu_{k,l}[i]$$

and explore one way to model them in the proposed simultaneous SAR imaging and cooperative target localization application.

With an assumption that the multipath reflections from targets are direct reflections from a number of virtual point scatterers, we can write the multipath components in the same forms as the direct responses from modulated targets. By modeling the 1-bounce multipath reflections from large reflective planes with first-order virtual point scatterers, we are able to predict specular multipath ghosts that appear in the reconstructed images.

5.1 Introduction and Related Work

Radar imaging techniques become increasingly attractive in a wide range of military and civilian applications, such as reconnaissance, geological mapping, security screening, robot navigation, autonomous driving, etc. Due to the scattering and reflection from obstacle surfaces like building walls, the returned signal from the field may reach the receiver through a countless number of paths, yielding multipath components in the backscatter signal. Such multipath echoes result in spurious targets (are referred as ghosts in literature, but as virtual targets in this chapter) to be reconstructed in radar images, and can significantly degrade the image quality. Therefore, the unwanted virtual targets generated in multipath propagation need to be positioned and suppressed for a high-quality detection, imaging, and localization of the real targets.

There is extensive literature on multipath positioning and mitigation in imaging radars [72–81]. Most articles have assumed a LOS path, a knowledge of the reflective geometry, and do not account for the modulation of targets. In [72], the authors developed a multipath exploitation technique for through-the wall-imaging using point spread functions that does not require *a priori* assumptions on the number of targets. Then the model was used in a SAR system to position multipath ghosts of stationary or slowly moving targets [73, 74]. In [75], SAR images demonstrating multipath ghosts of a human target in a rectangular room were obtained with FDTD EM simulation. In [76, 77], the first-order multipath propagating models were established for time-division MIMO imagers, but accuracy of positioned multipath ghosts was not analyzed. To suppress or mitigate the multipath ghost, the authors in [78] proposed an algorithm based on image fusion of correlation-weighted sub-apertures and significantly lowered the interference of first-order real-wall ghosts. And the authors in [79, 80] applied compressive sensing (CS)-based algorithms to both stationary and moving targets under wall scatterings that solves the inverse problem of joint localization and velocity estimation of the targets in an indoor multipath environment from a few measurements. They also proposed a computationally inexpensive scheme that first locates the targets using sparse reconstruction and subsequently estimates the velocity vectors. In addition, the authors in [81] compares two strategies for multipath clutter suppression, the multiplicative subarray image fusion (MSIF) and coherence factor (CF) filtering, and showed that they are both robust to noise and have similar detection performance.

In this Chapter, we consider the positioning of first-order virtual targets in a SAR measurement containing both unmodulated and cooperative targets by utilizing the general frequency response model and the SAR reconstruction algorithm proposed in previous chapters.

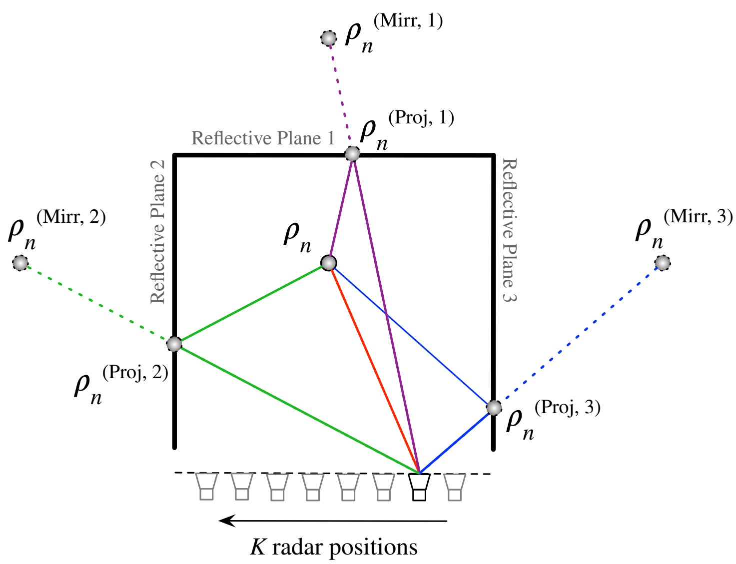

Figure 5.1: An example of first-order virtual point scatterers generated in an indoor SAR measurement. The three reflective walls create three mirrored and three projected point scatterers in addition to the one actual point scatterer.

5.2 *Virtual Targets in Simultaneous Imaging and Cooperative Target Localiaztion*

In a line-of-sight environment, when a radar signal is incident on a modulated target, a portion of the propagating wave is intercepted by the target and reflected back to the field. Due to the diffraction and reflection of other objects in the environment, target backscatter signals may reach the radar receiver through a countless number of paths. There can be clusters caused by multiple reflections of small objects that are spatially close to the target and major 1-bounce or multi-bounce interference from walls, floor, ceiling, and other large objects. This chapter focuses on the 1-bounce reflections from reflective planes (walls) that could happen in indoor SAR measurements, and uses first-order virtual point scatterers to model such reflections.

5.2.1 Mirrored and Projected Point Scatterers

A reflective plane creates two virtual point scatterers in addition to each actual point scatterer in the modulated target. One is the mirrored point scatterer that is symmetric to the actual scatterer about the plane, and the other is the projected point scatterer of the mirrored point point scatterer that is left on the reflective plane. The reflection coefficient values of both virtual point scatterers are dependent on the reflectivity of the plane. Fig. 5.1 illustrates the generation and usage of virtual point scatterers during a SAR measurement. At each radar sampling position, there are three mirrored point scatterers, $\rho_n^{(\mathrm{Mirr},1)}$, $\rho_n^{(\mathrm{Mirr},2)}$, and $\rho_n^{(\mathrm{Mirr},3)}$, three projected point scatterers, $\rho_n^{(\mathrm{Proj},1)}$, $\rho_n^{(\mathrm{Proj},2)}$, and $\rho_n^{(\mathrm{Proj},3)}$, and the actual point scatterer ρ_n. The backscatter signal obtained by the receiver includes reflections from all of them. Only the reflection from actual point scatterers contains useful target feature information, the rest are all unwanted multipath noise. It is noted that all virtual point scatterer in Fig. 5.1 are created by 1-bounce reflections. There could be additional higher order virtual point scatterers, e.g. the virtual point scatterer $\rho_n^{(mirror,1)}$ can also have its own mirror image about "Reflective Plane 2", but they are not discussed since they usually have very weak reflectivity.

5.2.2 *Multipath Frequency Response*

With the virtual point scatterers introduced above, the frequency response in SAR measurements (Eq. 3.1) with added multipath reflection can be written as

$$
\begin{aligned}
y_{k,l}[i] &= \overbrace{\sum_{n=1}^{N} \rho_{n,l}[i]\alpha_{k,l,n}^{2} e^{-j2\pi f_l \frac{2\left\|\vec{\mathbf{R}}_k+\vec{\mathbf{r}}_n\right\|}{c_0}}}^{\substack{\text{cooperative modulated and}\\ \text{unmodulated target response}}} + \text{Multipath} + \nu_{k,l}[i] \\
&= \overbrace{\sum_{n=1}^{N} \rho_{n,l}[i]\alpha_{k,l,n}^{2} e^{-j2\pi f_l \frac{2\left\|\vec{\mathbf{R}}_k+\vec{\mathbf{r}}_n\right\|}{c_0}}}^{\text{target direct response}} \\
&\quad + \overbrace{\sum_{p=1}^{P}\sum_{n=1}^{N} \rho_{n,l}^{(\mathrm{Mirr},p)}[i]\alpha_{k,l,n}^{2,(\mathrm{Mirr},p)} e^{-j2\pi f_l \frac{2\left\|\vec{\mathbf{R}}_k^{(\mathrm{Mirr},p)}+\vec{\mathbf{r}}_n^{(\mathrm{Mirr},p)}\right\|}{c_0}}}^{\text{mirrored target response}} \\
&\quad + \overbrace{\sum_{p=1}^{P}\sum_{n=1}^{N} \rho_{n,l}^{(\mathrm{Proj},p)}[i]\alpha_{k,l,n}^{2,(\mathrm{Proj},p)} e^{-j2\pi f_l \frac{2\left\|\vec{\mathbf{R}}_k^{(\mathrm{Proj},p)}+\vec{\mathbf{r}}_n^{(\mathrm{Proj},p)}\right\|}{c_0}}}^{\text{projected target response}} + \nu_{k,l}[i]
\end{aligned}
, \qquad (5.1)
$$

where $\rho_{n,l}^{(\mathrm{Mirr},p)}$ and $\rho_{n,l}^{(\mathrm{Proj},p)}$ denote the p-th mirrored and projected point scatterers corresponding to the n-th actual point scatterer, $\alpha_{k,l,n}^{2,(\mathrm{Mirr},p)}$ and $\alpha_{k,l,n}^{2,(\mathrm{Proj},p)}$ are the two-way channel loss factors, $\vec{\mathbf{R}}^{(\mathrm{Mirr},p)}$ and $\vec{\mathbf{R}}^{(\mathrm{Proj},p)}$ are the range vectors from the radar to virtual target centers, and $\vec{\mathbf{r}}_n^{(\mathrm{Mirr},p)}$ and $\vec{\mathbf{r}}_n^{(\mathrm{Proj},p)}$ are the vectors from virtual target centers to the p-th mirrored and projected point scatterers. The frequency response at each frequency and each radar position contains three parts: the direct response from the target, the reflection from the mirrored virtual target, and the reflection from the projected virtual target.

And the bistatic frequency response model, with added multipath reflections, in the simultaneous imaging and localization application (Eq. 3.7) can be written as

$$
\begin{aligned}
y_{k,l}[i] = &\overbrace{\sum_{m=1}^{M} \tilde{\rho}_m \tilde{\alpha}^{\mathrm{TX}}_{k,l,m} \tilde{\alpha}^{\mathrm{RX}}_{k,l,m} e^{-j2\pi f_l \frac{R\left(\mathbf{z}^{\mathrm{TX}}_k, \mathbf{z}^{\mathrm{RX}}_k, \tilde{\mathbf{z}}_m\right)}{c_0}}}^{\text{actual constant scatterers}} \\
&+ \overbrace{\sum_{p=1}^{P} \sum_{m=1}^{M} \tilde{\rho}^{(\mathrm{Mirr},p)}_m \tilde{\alpha}^{\mathrm{TX},(\mathrm{Mirr},p)}_{k,l,m} \tilde{\alpha}^{\mathrm{RX},(\mathrm{Mirr},p)}_{k,l,m} e^{-j2\pi f_l \frac{R\left(\mathbf{z}^{\mathrm{TX}}_k, \mathbf{z}^{\mathrm{RX}}_k, \tilde{\mathbf{z}}^{(\mathrm{Mirr},p)}_m\right)}{c_0}}}^{\text{mirrored constant scatterers}} \\
&+ \overbrace{\sum_{p=1}^{P} \sum_{m=1}^{M} \tilde{\rho}^{(\mathrm{Proj},p)}_m \tilde{\alpha}^{\mathrm{TX},(\mathrm{Proj},p)}_{k,l,m} \tilde{\alpha}^{\mathrm{RX},(\mathrm{Proj},p)}_{k,l,m} e^{-j2\pi f_l \frac{R\left(\mathbf{z}^{\mathrm{TX}}_k, \mathbf{z}^{\mathrm{RX}}_k, \tilde{\mathbf{z}}^{(\mathrm{Proj},p)}_m\right)}{c_0}}}^{\text{projected constant scatterers}} \\
&+ \overbrace{\sum_{n=1}^{N} \rho_{n,l}[i] \alpha^{\mathrm{TX}}_{k,l,n} \alpha^{\mathrm{RX}}_{k,l,n} e^{-j2\pi f_l \frac{R\left(\mathbf{z}^{\mathrm{TX}}_k, \mathbf{z}^{\mathrm{RX}}_k, \mathbf{z}_n\right)}{c_0}}}^{\text{actual time-variant scatterers}} \\
&+ \overbrace{\sum_{p=1}^{P} \sum_{n=1}^{N} \rho^{(\mathrm{Mirr},p)}_{n,l}[i] \alpha^{\mathrm{TX},(\mathrm{Mirr},p)}_{k,l,n} \alpha^{\mathrm{RX},(\mathrm{Mirr,p})}_{k,l,n} e^{-j2\pi f_l \frac{R\left(\mathbf{z}^{\mathrm{TX}}_k, \mathbf{z}^{\mathrm{RX}}_k, \mathbf{z}^{(\mathrm{Mirr},p)}_n\right)}{c_0}}}^{\text{mirrored time-variant scatterers}} \\
&+ \overbrace{\sum_{p=1}^{P} \sum_{n=1}^{N} \rho^{(\mathrm{Proj},p)}_{n,l}[i] \alpha^{\mathrm{TX},(\mathrm{Proj},p)}_{k,l,n} \alpha^{\mathrm{RX},(\mathrm{Proj,p})}_{k,l,n} e^{-j2\pi f_l \frac{R\left(\mathbf{z}^{\mathrm{TX}}_k, \mathbf{z}^{\mathrm{RX}}_k, \mathbf{z}^{(\mathrm{Proj},p)}_n\right)}{c_0}}}^{\text{projected time-variant scatterers}} + \nu_{k,l}[i],
\end{aligned}
\tag{5.2}
$$

where the complex reflection coefficient values, the one-way loss factors, and the ranges vectors are all added with a superscript (Mirr, p) or (Proj, p) to indicate that they are parameters of the p-th mirrored or projected point scatterer.

5.2.3 Imaging and Localization of Virtual Modulated Targets

In the simultaneous SAR imaging, sensor tag localization, and backscatter data uplink application, multiple samples are collected at each radar position and for each carrier frequency. The tag packets contain balanced orthogonal SAR code words to enable tag-vs-tag and tag-vs-environment discrimination. In the demonstrated 2 tag (J=2) case, the SAR codes have been defined as

$$
\mathbf{c}_j = \begin{cases} [+1, -1, +1, -1]^\dagger, & j = 1 \\ [+1, +1, -1, -1]^\dagger, & j = 2 \end{cases}.
$$

Since each point scatterer in a BPSK tag has only two different reflection coefficient values, $\rho_{\{-1,1\},n,l}$, the virtual point scatterers corresponding to each actual point scatterer also have two different reflection coefficient values $\rho^{(*,p)}_{\{-1,1\},n,l}$, with $(*, p)$ meaning either mirrored or projected point scatterers. Therefore, the frequency response vector at the k-th radar position considering multipath propagation becomes

$$\begin{aligned}\mathbf{y}_k[i] =& \mathbf{y}_k^{\mathrm{UM}} + \mathbf{y}_k^{\mathrm{UM,Mirr}} + \mathbf{y}_k^{\mathrm{UM,Proj}} \\ &+ \mathbf{y}_{\{-1,+1\},k}^{j=1} + \mathbf{y}_{\{-1,+1\},k}^{j=1,\mathrm{Mirr}} + \mathbf{y}_{\{-1,+1\},k}^{j=1,\mathrm{Proj}} + \mathbf{y}_{\{-1,+1\},k}^{j=2} + \mathbf{y}_{\{-1,+1\},k}^{j=2,\mathrm{Mirr}} + \mathbf{y}_{\{-1,+1\},k}^{j=2,\mathrm{Proj}} + \nu_k[i],\end{aligned} \tag{5.3}$$

where $\mathbf{y}_k^{\mathrm{UM},*}$ is the response from all mirrored or projected scatterers of the unmodulated targets, $\mathbf{y}_{\{-1,+1\},k}^{j=1,*}$ and $\mathbf{y}_{\{-1,+1\},k}^{j=2,*}$ are the frequency responses of the virtual point scatterers that are changing with the different reflection states of Tag 1 and Tag 2 respectively. The four modulation state combinations found in the first four measurement samples are

$$\begin{aligned}\mathbf{y}[1] =& (\mathbf{y}^{\mathrm{UM}} + \mathbf{y}^{\mathrm{UM,Mirr}} + \mathbf{y}^{\mathrm{UM,Proj}}) \\ &+ (\mathbf{y}_{+1}^{j=1} + \mathbf{y}_{+1}^{j=1,\mathrm{Mirr}} + \mathbf{y}_{+1}^{j=1,\mathrm{Proj}}) + (\mathbf{y}_{+1}^{j=2} + \mathbf{y}_{+1}^{j=2,\mathrm{Mirr}} + \mathbf{y}_{+1}^{j=2,\mathrm{Proj}}) + \nu[1] \\ \mathbf{y}[2] =& (\mathbf{y}^{\mathrm{UM}} + \mathbf{y}^{\mathrm{UM,Mirr}} + \mathbf{y}^{\mathrm{UM,Proj}}) \\ &+ (\mathbf{y}_{-1}^{j=1} + \mathbf{y}_{-1}^{j=1,\mathrm{Mirr}} + \mathbf{y}_{-1}^{j=1,\mathrm{Proj}}) + (\mathbf{y}_{+1}^{j=2} + \mathbf{y}_{+1}^{j=2,\mathrm{Mirr}} + \mathbf{y}_{+1}^{j=2,\mathrm{Proj}}) + \nu[2] \\ \mathbf{y}[3] =& (\mathbf{y}^{\mathrm{UM}} + \mathbf{y}^{\mathrm{UM,Mirr}} + \mathbf{y}^{\mathrm{UM,Proj}}) \\ &+ (\mathbf{y}_{+1}^{j=1} + \mathbf{y}_{+1}^{j=1,\mathrm{Mirr}} + \mathbf{y}_{+1}^{j=1,\mathrm{Proj}}) + (\mathbf{y}_{-1}^{j=2} + \mathbf{y}_{-1}^{j=2,\mathrm{Mirr}} + \mathbf{y}_{-1}^{j=2,\mathrm{Proj}}) + \nu[3] \\ \mathbf{y}[4] =& (\mathbf{y}^{\mathrm{UM}} + \mathbf{y}^{\mathrm{UM,Mirr}} + \mathbf{y}^{\mathrm{UM,Proj}}) \\ &+ (\mathbf{y}_{-1}^{j=1} + \mathbf{y}_{-1}^{j=1,\mathrm{Mirr}} + \mathbf{y}_{-1}^{j=1,\mathrm{Proj}}) + (\mathbf{y}_{-1}^{j=2} + \mathbf{y}_{-1}^{j=2,\mathrm{Mirr}} + \mathbf{y}_{-1}^{j=2,\mathrm{Proj}}) + \nu[4]\end{aligned}. \tag{5.4}$$

It can be seen from the above four samples, the reconstructed virtual tags, including both mirrored and projected tags, are always in coexistence with the localized actual tags of interest and existing in the imaging results of all scattering objects. The SAR reconstructions discussed in Section 4.2.1, 4.2.2, and 4.2.3 can then be expanded to add the multipath propagation for the general multi-tag measurements.

Single Tag Localization with Multipath Reflections Included

The reconstruction of the j-th tag, along with its P mirrored tags and P projected tags (P being the number of reflective planes), can be obtained by

$$\hat{\boldsymbol{\rho}}_j + \sum_{p=1}^{P} \hat{\boldsymbol{\rho}}_j^{(\mathrm{Mirr},p)} + \sum_{p=1}^{P} \hat{\boldsymbol{\rho}}_j^{(\mathrm{Proj},p)} = \mathbf{A}^P \mathbf{Y} \mathbf{c}_j, \tag{5.5}$$

where $\hat{\boldsymbol{\rho}}_j^{(*,p)}$ is the reflection coefficient estimate of the p-th virtual counterpart of the j-th tag, $\mathbf{A}^P$ is the new reconstruction matrix to include the positions and path loss of virtual targets, and $\mathbf{Y}$ is the same measurement matrix as in Eq. 4.5. Due to the orthogonality property of SAR codes, the contributions of other tags and their multipath reflections are canceled. Constant scatterer multipath responses from the environment are also canceled due to the balance property. And the SNR during the reconstruction is improved because of the inherent noise averaging.

Simultaneous Multi-Tag Localization with Multipath Reflections Considered

By multiplying $\mathbf{Y}$ with the sum of multiple SAR codes, e.g. $\mathbf{c}_j \in \mathcal{C}$, where $\mathcal{C}$ is the set of corresponding codes, a combined reconstruction of these tags and all their virtual tags can be obtained. Hence,

$$\hat{\boldsymbol{\rho}}_{\text{multi}} + \sum_{p=1}^{P} \hat{\boldsymbol{\rho}}_{\text{multi}}^{(\text{Mirr},p)} + \sum_{p=1}^{P} \hat{\boldsymbol{\rho}}_{\text{multi}}^{(\text{Proj},p)} = \mathbf{A}^{P}\mathbf{Y} \sum_{\mathbf{c}_j \in \mathcal{C}} \mathbf{c}_j, \tag{5.6}$$

where $\hat{\boldsymbol{\rho}}_{\text{multi}}^{(*,p)}$ is the combined reflection coefficient estimate of the virtual tags mirrored by the p-th reflective surface or projected on the p-th plane. The SNR during the reconstruction is also increased due to noise averaging.

Imaging All the Actual and Virtual Targets

With $\mathbf{c}^{\text{SO}}$ being a unit vector, an image containing all of the actual and virtual scattering objects in the ROI can be reconstructed, hence

$$\hat{\boldsymbol{\rho}}_{\text{obj}} + \sum_{p=1}^{P} \hat{\boldsymbol{\rho}}_{\text{obj}}^{(\text{Mirr},p)} + \sum_{p=1}^{P} \hat{\boldsymbol{\rho}}_{\text{obj}}^{(\text{Proj},p)} = \mathbf{A}^{P}\mathbf{Y}\mathbf{c}^{\text{SO}}, \tag{5.7}$$

where $\hat{\boldsymbol{\rho}}_{\text{obj}}^{(*,p)}$ denotes the reflection coefficient estimate of virtual targets mirrored by or projected on the p-th reflective surface.

5.3 Reconstruction of Virtual Targets in Simultaneous Imaging and Localization

5.3.1 Measurement and Phase Center Correction

To verify the multipath response model in the simultaneous imaging and localization application, the same indoor measurements in Chapter 4.3 are repeated with only one modification, which is adding a large reflective plane behind the Styrofoam. The reflective plane is 80 cm wide and 5.24 m away from the motion stage.

As been discussed in Chapter 4.4, the antenna phase center offsets must be estimated during the calibration process and subtracted from the exponential term of Eq. 5.2 for imaging and localization scenarios separately. The measured TX-RX phase center offset of 12.03 cm and tag phase center offset of 10.66 cm are used to minimize the errors in SAR reconstruction.

5.3.2 Imaging Results

When reconstructing images of scattering objects, the TX-RX phase center calibration result is used to compensate the phase center in $\mathbf{Y}$. After multiplying $\mathbf{Y}$ with $\mathbf{c}^{\text{SO}}$, an image containing all targets and virtual targets can be obtained as shown in Fig. 5.3a. It clearly shows the reflective plane and a mirror

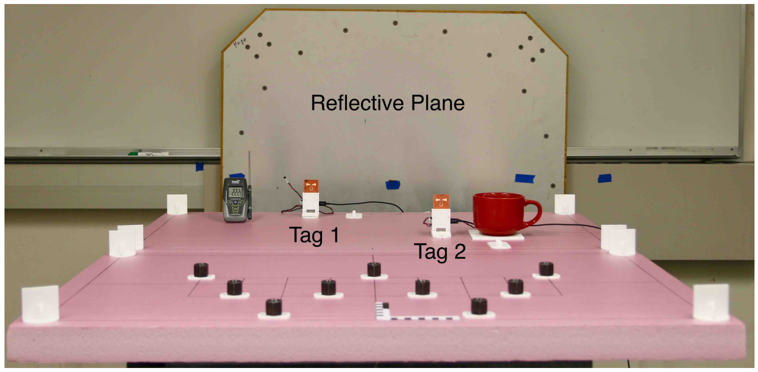

Figure 5.2: Rerun the measurements in Chapter 4.3 with the same setup except that a large reflective plane is placed behind the Styrofoam.

image of Tag 1, with the reflectivity normalized and represented on a log scale. Mirror images of Tag 2 and the nine hex nuts are hardly discernible because their 1-bounce reflections are weak. The projected images of the targets are overlapped with the PSFs of the reflective plane.

5.3.3 Localization Results

To localize the tags and also reconstruct virtual tags, the phase center offsets of TX, RX, and tag are all compensated in $\mathbf{Y}$. Figs. 5.3c to 5.3e show single tag and two-tag localization results. The background clutter and reflections from unmodulated targets are canceled due to the balanced SAR code words.

A detailed comparison of imaging and localization results with the predicted positions of mirrored and projected cooperative targets is shown in Table. 5.1. The three type of results agree well to the centimeter level. The localized results have a maximum 2-D offset of 3.6 cm when compared to imaging results and 1.4 cm offset compared to the predicted positions.

Table 5.1: Comparison of reconstructed virtual targets with their predicted positions

Target	Imaging (m) (x, y)	Localization (m) (x, y)	Predicted Position (m) (x, y)
Mirrored Tag 1	(-0.156, 5.774)	(-0.160, 5.774)	(-0.158, 5.775)
Mirrored Tag 2	(0.150, 6.094)	(0.144, 6.06)	(0.158, 6.063)
Projected Tag 1	-	(-0.148, 5.232)	(-0.154, 5.230)
Projected Tag 2	-	(0.146, 5.232)	(0.154, 5.230)

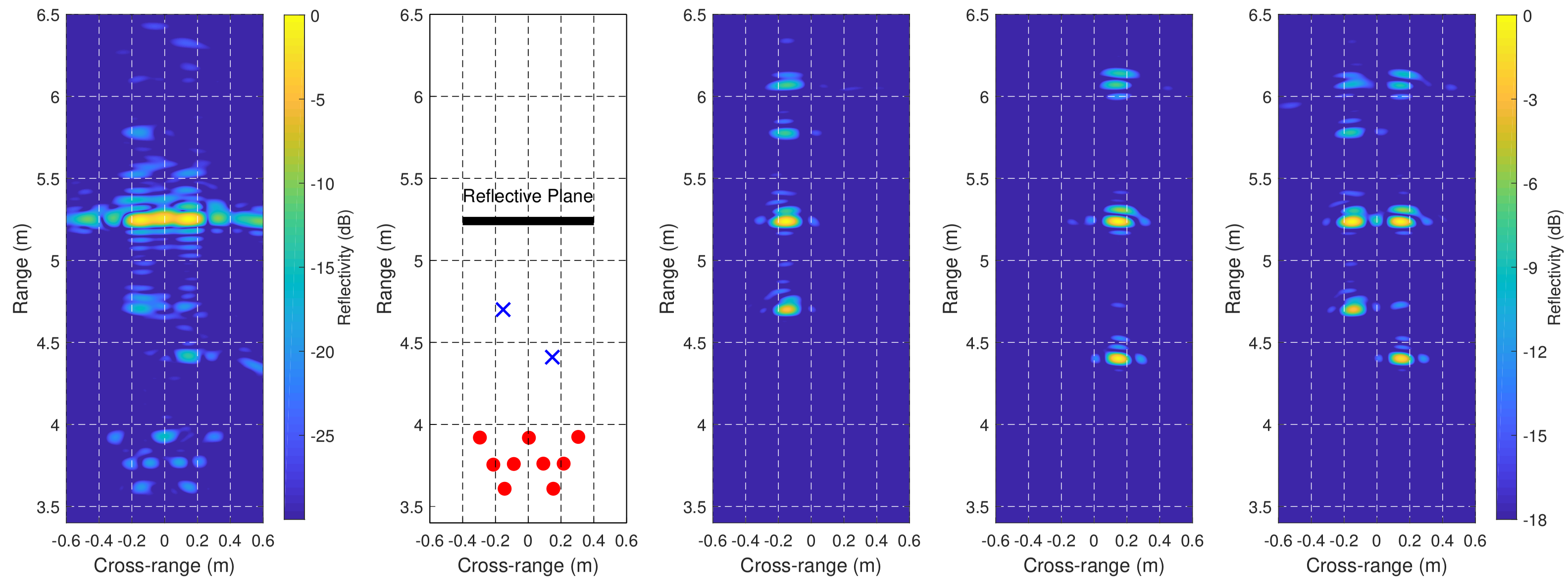

(a) (b) (c) (d) (e)

Figure 5.3: (a) Imaging result showing all reflective objects and virtual tags. (b) Ground truth of the tags, nuts, and the reflective plane. Localization results show the actual, mirrored, and projected cooperative targets: (c) Tag 1 only; (d) Tag 2 only; (e) Tag 1 and Tag 2 together.

5.4 Chapter Conclusion

In this chapter, we assumed that the multipath reflections from targets are direct reflections from a number of virtual point scatterers. And we proposed two types of first-order virtual point scatterers that are always simultaneously presented with their corresponding actual point scatterer. These virtual point scatterers are created by a large reflective plane in 1-bounce multipath reflections, which are commonly seen in indoor SAR measurements. The frequency response model, with added multipath response components, is derived based on these virtual point scatterers. By correlating the SAR code words of cooperative targets with multiple SAR measurement samples, we are able to predict specular multipath ghosts that shall appear in the imaging results of all objects and localization results of a single or multiple tags. The predicted positions agree well with the reconstructed multipath ghosts to an error of 1.4 cm in localization and 3.6 cm in imaging scenario.

Chapter 6

QUADCOPTER UAV: AN EXAMPLE OF UNCOOPERATIVE MODULATED TARGETS

In this chapter, a quadcopter UAV is selected as an uncooperative target for the study. Several indoor measurements are implemented to characterize the reflectivity, static and dynamic radar cross sections, and micro-Doppler signatures of the quadcopter using different radar system prototypes.

It is seen that by applying the general target model

$$\boxed{y_{k,l}[i] = \overbrace{\sum_{n=1}^{N} \rho_{n,l}[i]\ \alpha^2_{k,l,n}[i]\ e^{-j2\pi f_l \frac{2\left\|\vec{\mathbf{R}}_k[i]+\vec{\mathbf{r}_n}[i]\right\|}{c_0}}}^{\text{general modulated target response}} + \text{Multipath}_k + \nu_{k,l}[i],}$$

we are able to achieve these goals:

- perform 3-D SAR imaging on the quadcopter for a reflectivity profile and identify the contribution of propellers to the total reflectivity;
- compare the static and dynamic radar cross sections of the quadcopter;
- analyze the interference between different micro-motions in a same uncooperative target, in this example, the interference between multiple propellers when they are rotating simultaneously;
- characterize the spectral properties of Doppler shifts from one micro-motion at different intensities (different rotation rates of one rotating propeller).

6.1 Overview on the Research of UAVs

6.1.1 Research Background

Unmanned Aerial Vehicles (UAVs) are a special type of aerial targets which are small and without a human pilot onboard. Over past few decades, the cheap production of lightweight flight controllers, global positioning systems, cameras, and other aircraft accessories stimulates a massive growth in the manufacturing and sales of consumer grade UAVs which are small and easily maneuvered. They are widely used in outdoor research, military surveillance, aerial imagery, news reporting, and merchandise delivery [82, 83]. However, they are also rapidly becoming low-cost aerial platforms for hostile reconnaissance, targeting, and weapon delivery and now are emerging threats for ground forces.

Unlike traditional air targets, consumer grade UAVs usually operate at low altitudes which make them easily hidden by complex terrain. They also move at slow speeds and therefore impractical to differentiate from other movers. In addition, their small size (radar cross section) makes them difficult to be sensed by a traditional radar system. Given the above limitations and the rapid proliferation of consumer grade UAVs with increasing endurance and payload capacity, aerial surveillance systems that have the abilities to detect, track, and classify these small consumer grade UAVs need to be developed.

6.1.2 Prior Art

Two of the traditional techniques used for aerial target identification and classification are the Inverse Synthetic Aperture (ISAR) imaging and micro-Doppler signature analysis.

ISAR, shares the same underlying theory with SAR and only differs in configuration, utilizes the motion of targets rather than the radar systems to create a synthetic aperture. C. J. Li et al. in [84] conducted measurements on several small consumer UAVs fixed on a turntable in an anechoic chamber and reconstructed ISAR images to reveal the size and geometrical outlines of each UAV. W. Lee et al. in [85] verified the feasibility of ISAR imaging in the classification of simultaneously flying UAVs. By applying motion and phase compensations to the backscattered signals corrupted by micro-Doppler effects, high resolution ISAR images are obtained showing structures and a number of rotors. ISAR imaging is not practical in many cases. In fact, not much work has been done using this technique on UAVs because ISAR imaging has to depend on the translation and rotation of targets and has a long observation time [86].

The micro-Doppler signature analysis, on the other hand, is free of such limitations in target classification. And it can be used on any targets that have micro-motions, and is especially beneficial in the classification of UAVs that have periodic rotations. There is extensive literature on UAV detection and classification using micro-Doppler signatures and we only list some of it as examples. A. K. Singh and Y. H. Kim [87] showed

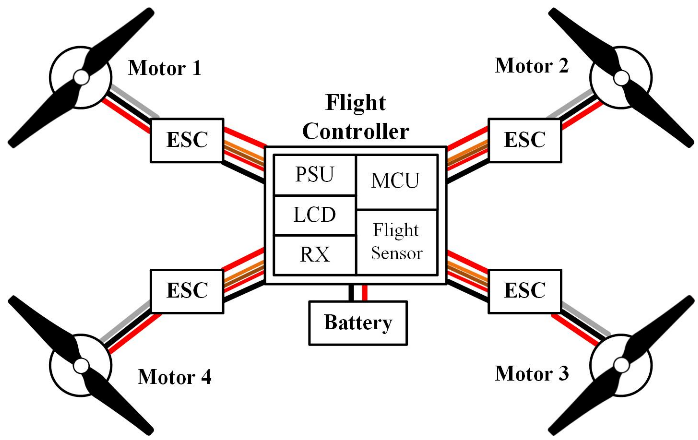

Figure 6.1: System Diagram of a typical quadcopter.

that the blade length and rotation rate of UAV systems can be calculated using micro-Doppler signatures. P. Molchanov et al. [88] verified their micro-Doppler signature-based feature extraction methods with real radar measurements. They used micro-Doppler signatures captured from a 9.5 GHz radar to classify planes, quadcopters, helicopters, and birds. P. Zhang et al. [89] demonstrated a classification accuracy up to 94.7% to classify quadcopters, helicopters and hexacopters by using a dual-band (24 GHz and 9.8 GHz) radar sensor and the Support Vector Machine (SVM). B. K. Kim et al. [90] presented polarimetric analysis on small commercial UAVs from different perspective angles that maximize and minimize RCS and micro-Doppler signature. M. Ritchie et al. [91] used micro-Doppler signatures collected by a multistatic radar to detect and discriminate among small UAVs that were loaded with different weights.

In this thesis, we choose an off-the-shelf quadcopter UAV as an example in the study of uncooperative targets. This chapter presents results from measurements of the whole quadcopter structure. Chapter 6 analyzes the micro-Doppler frequency shifts and spectral envelopes with just a single propeller using the point scatterer expression.

6.1.3 Quadcopter Hardware Selection and Characterization Methods

Quadcopters are multi-rotor helicopters that are lifted and propelled by four vertically oriented propellers. Two of these fixed pitched propellers rotates in clockwise (CW) and the other two in counterclockwise (CCW), and the identical ones are mounted diagonally opposite to each other. Independently changing the rotating speed of the propellers can yield to different yaw, pitch, and roll motions of a quadcopter, such as hovering, climbing, descending, and turning. They show advantages over helicopters and other aircrafts for their mechanical simplicity and operational safety due to the shorter rotors. Therefore, they become a

Figure 6.2: Turnigy SK450 quadcopter, with the original flight controller unit highlighted.

popular selection for small-scale, remote-controlled UAVs.

In general, a commercial quadcopter consists of a flight controller unit, four electric speed controllers (ESCs), four brushless motors to spin the CW and CCW propellers, and a battery pack attached to the quadcopter frame. Other optional components such as cameras, GPS systems, and telemetries can also be added for imaging and delivery purpose.

A system diagram of a typical quadcopter is depicted in Fig. 6.1. The core component that stabilize and control a quadcopter is the flight controller unit. It has an RF receiver to capture wireless remote control signals and decode flight motion instructions, a microprocessor that compares flight motion instructions with data from flight sensors, and a power distribution unit to supply high AC currents to the motors. The microprocessor outputs pulse width modulation (PWM) signals to ESCs which then generate three-phase AC power to run brushless motors. The speed of the motor is varied by adjusting the duty cycle of controlling currents delivered to several windings of the motor.

In this chapter, the quadcopter is first characterized as an unmodulated target by 3-D SAR imaging and RCS measurements to find the distribution of its point scatterers. Then micro-Doppler measurements are implemented to explore the uncooperative features of the target. The off-the-shelf Turnigy SK450 (see Fig. 6.2) is chosen for research because the flight controller unit can be easily dissembled and replaced with a custom-designed controller. Hence, we can individually control the rotation speed of each motor to learn about their micro-Doppler signatures. *Noted that in all measurements, the quadcopter, either in operation state or is powered down, is always fixed to a platform or tripod for safety concerns.*

Table 6.1: Characterization measurements of the quadcopter

Quadcopter	Target Model Category	Measurement	Quadcopter Operation		Implementation		Target Feature	Presentation of Results
			Number of Rotating Propellers	Rotation Rate	Facilities	Environment		
Turnigy SK450 (fixed on a tripod)	unmodulated target	3-D SAR Imaging	0		motion stage, VNA as K-band radar	lab	point scatterer distribution	2-D and 3-D reflectivity profiles
		RCS measurement	0		VNA as K-band radar	anechoic chamber	scalar reflectivity	RCS over wideband
	uncooperative modulated target	micro-Doppler measurement	4	varying	custom K-band radar		micro-Doppler frequency shifts	spectrograms
			4	fixed	custom K-band radar and flight controller unit			dynamic RCS power spectral density plots
			2 v.s. each separately	fixed				
			1	fixed at 3 rates				

6.2 Quadcopter Characterized as an Unmodulated Target

6.2.1 Distribution of Point Scatterers in a Quadcopter Based on 3-D SAR Imaging

Measurement Setup

In this section, we leverage the SAR imaging technology at K-Band (15 − 26.5 GHz) to achieve a 3-D reflectivity profile of the Turnigy SK450 quadcopter including all flight components. By coherently processing the phase and amplitude of the backscatter signal collected over a synthetic aperture, the primary and secondary contributors to the reflectivity of the quadcopter can be identified.

To implement a 3-D SAR measurement, the setup used in Chapter 4 which has an IMS 600 linear stage implemented horizontally to create motion in cross-range direction (x-dimension) is now adapted to using two linear stages (one horizontal, the other vertical) to move antennas along both cross-range direction ($x = [-0.3,\ 0.3]$ m) and the vertical direction ($z = [-0.3,\ 0.3]$ m). A motion step size of 2 mm is chosen for both directions to have a total of 301 × 301 sampling positions and avoid spatial aliasing. The schematics of two quadcopter measurement configurations are shown in Fig. 6.3 and Fig. 6.4. When the quadcopter is landed in plane $y = 0.6$ m (the radar antennas looking at the quadcopter in the pitch direction), we call it a top-view characterization, see Fig. 6.3. When the quadcopter lands in plane $z = 0$ m (viewing by the radar from the quadcopter edges), we call it an edge-view characterization, see Fig. 6.4. The TX and RX antennas are closely located on a 3-D printed holding structure with a distance of 8 cm. They are 10 dB standard-gain horn antennas which are connected to the VNA to collect S_{21} data from the field.

Measurement Results

By applying the SAR reconstruction algorithms derived in Chapter 3, the resulting 3-D images of Turnigy SK450 are shown in Fig. 6.5a and 6.5b respectively. Averaging the absolute reflectivity values in the range direction ($y = [0.582, 0.728]$ m for top-view configuration and $y = [0.518, 0.938]$ m for edge-view configuration) gives 2-D overlapping reflectivity profiles as shown in Fig. 6.5c and Fig. 6.5d. The Turnigy sk450 quadcopter has an Acrylonitrile Butadiene Styrene (ABS) plastic body frame which is transparent to the K-band radar signal. Hence the reflections are mainly from other parts. As can be seen in the images, there is significant specular scatterings from the carbon-loaded and metallic parts (battery, motors, electronics/printed circuits) both in the central region of the quadcopter where the flight controller unit and battery are located, and along the arms where the four ESCs, motors, and propellers are located.

The backscattered signal power of each quadcopter component (e.g. received signal power of all scatterers in a propeller) is calculated by first locating a region for that component in the SAR image, then integrating the backscattered power (square of the scattering E-field magnitude) of all scatterers in that region, and

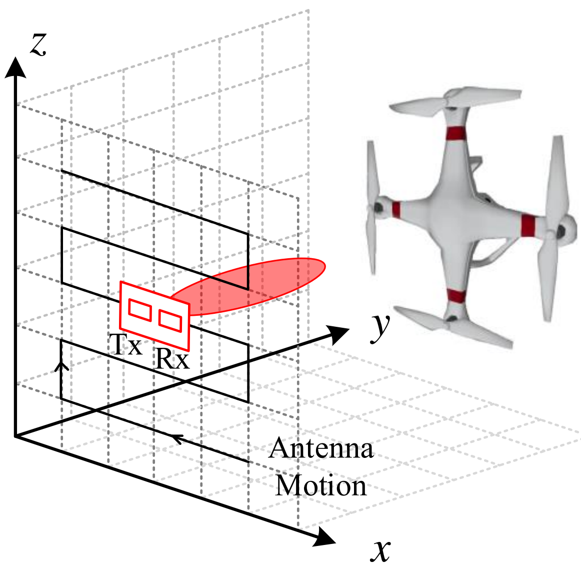

Figure 6.3: Top-view 3-D SAR imaging characterization of a quadcopter. The antennas look at the quadcopter in the pitch direction.

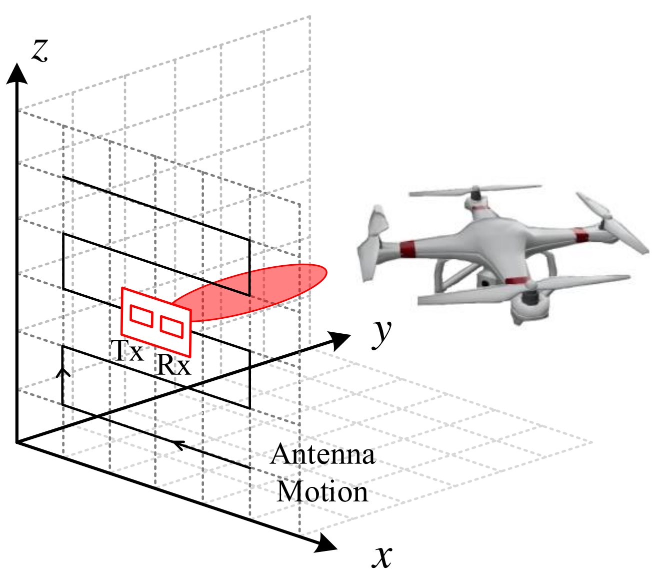

Figure 6.4: Edge-view 3-D SAR imaging characterization of a quadcopter. The antennas look at the quadcopter from the edges.

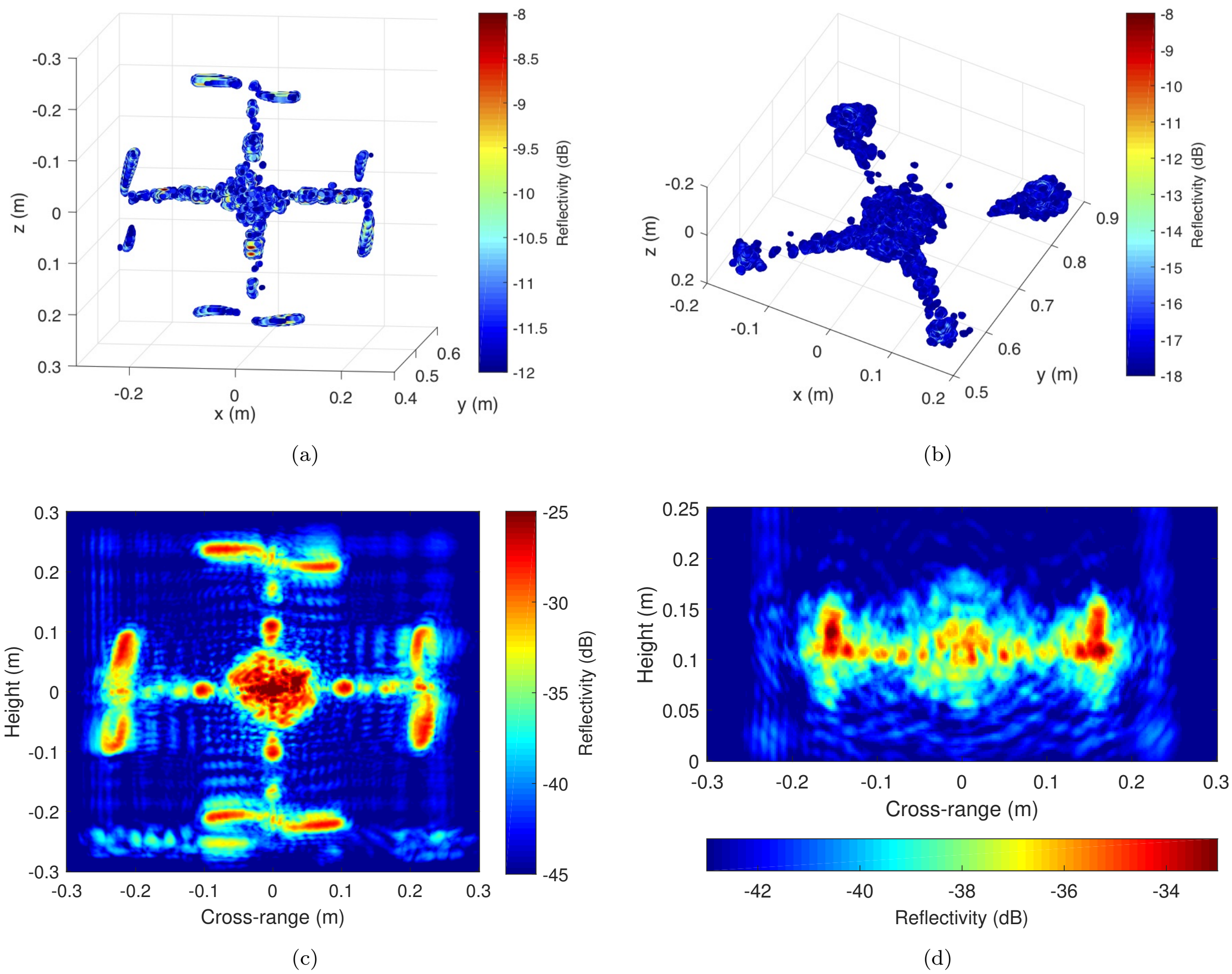

Figure 6.5: 3-D SAR images of a Turnigy SK450 quadcopter (a) looking from the top and (b) looking from the edges. (c) and (d) show the mean reflectivity in range direction (averaging the absolute reflectivity values over $y = [0.582, 0.728]$ m for top-view characterization and over $y = [0.518, 0.938]$ m for edge-view characterization). All the reflectivity values are normalized to the maximum reflection of each configuration. Different scales are used in different figures for clearly showing the profile and detail structures. *Courtesy of Dr. Claire M. Watts at University of Washington.*

Table 6.2: Ratio of the backscatter signal power from different components in the quadcopter

Quadcopter Component	**Ratio to the Total Reflected Power**
4 propellers and 4 motors	27.8%
4 arms (with 4 ESCs mounted)	32.1%
Central part (contains a battery, sensors, and a flight controller unit)	37.3%
Others	2.8%

finally dividing this value by the total backscatter signal power from all point scatterers in the image. The resulting ratio of each component in a top-view characterization can be seen in Table 6.2. We find that around 27.8% of the total backscatter signal power is due to scatterings from the propellers and motors.

6.2.2 Radar Cross Section of a Quadcopter

RCS Equation

When the radar signal wave is incident on the target, only a portion of the transmitted power is intercepted by the target and reflected back to the field. Radar cross section (RCS), denoted as σ, is the equivalent reflective area that intercepts the incident power. It can be seen as the projected area in the radar antenna beam and has a unit of square meter (frequently expressed in dBsm). The RCS of a target can be derived from Eq. 2.11, which is given as

$$\begin{aligned}\sigma =&\frac{P_{\mathrm{r}}(4\pi)^3 R_1^2 R_2^2}{P_{\mathrm{t}} G_{\mathrm{t}} G_{\mathrm{r}} \lambda^2}\\ =&\frac{|S_{21}|^2 (4\pi)^3 R_1^2 R_2^2}{G_{\mathrm{t}} G_{\mathrm{r}} \lambda^2},\end{aligned} \tag{6.1}$$

where R_1 and R_2 are distances from the transmit and receive antenna phase center to the quadcopter body center measured with a laser meter.

Measurement

In this section, a broadband (15 – 26.5 GHz) measurement is implemented in an anechoic chamber using the bistatic horn antennas connected to a VNA functioning as a radar to collect the frequency response (S_{21}) from the field and then estimate the RCS of the Turnigy SK450. The quadcopter is fixed on a tripod in the chamber and is 3 m away from the antenna pair.

Since the RCS of the target can vary with its orientation to the antennas, measurement frequency,

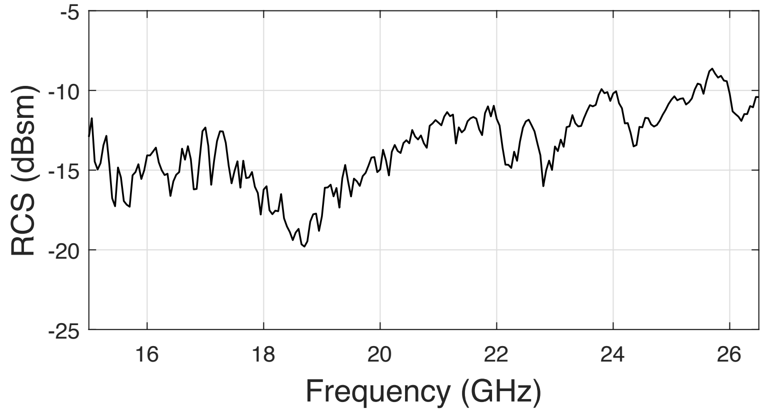

(a) Top-View

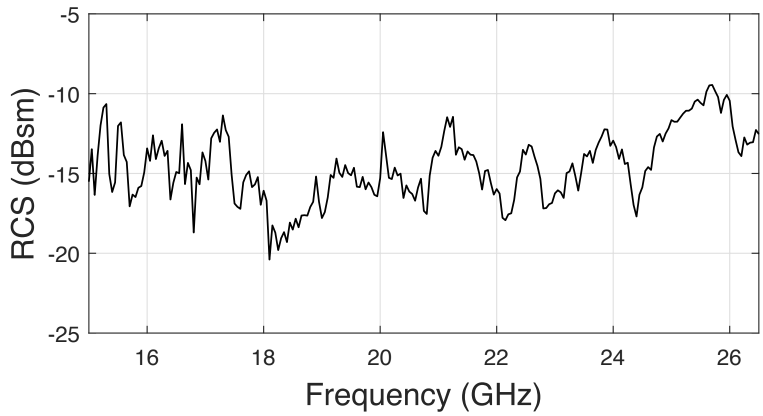

(b) Edge-View

Figure 6.6: Mean RCS of a Turnigy SK450 quadcopter over 15 – 26.5 GHz when the radar looks at the quadcopter from the (a) top and (b) edges.

and antenna polarization, a statistical averaging approach is used across multiple quadcopter orientations during the measurement. In either a top-view or edge-view configuration, small deviations from the starting quadcopter orientation (e.g. in top-view measurements, the quadcopter is slightly turned by several degrees about the vertical direction in clockwise and counter-clockwise) are made to sample the scattered field and then a statistical average is applied in the calculation.

The measured mean RCS results of the Turnigy SK450 over 15 – 26.5 GHz for the two configurations are shown in Fig. 6.6. In both cases, the RCS values range from -20 dBsm to -8 dBsm depending on the frequency. In comparison with typical RCS values of other targets listed in Table 6.3, the Turnigy SK450 has an RCS value approximating a bird.

Table 6.3: Typical radar cross section values

Target	**RCS (dBsm)**	**Target**	**RCS (dBsm)**
Frigate (103 m length)	37 ∼ 50	DJI Matrice 200	-10 ∼ 5
Pickup truck	23	DJI Inspire 1	-15 ∼ -5
Cargo aircraft	Up to 20	**Turnigy SK450**	**-20 ∼ -10**
Helicopter	5	Large bird	-20
Human	0	Large insect (locust)	-40

6.3 Quadcopter Characterized as an Uncooperative Target

6.3.1 Implementation of K-Band Measurements in the Chamber

To understand the micro-Doppler signature of an operating Turnigy SK450, two different sets of characterization measurements are implemented in the anechoic chamber using a custom-designed transceiver front-end and the horn antenna pair from the SAR configuration.

In the first set of measurements, we use the stock remote control that comes with the quadcopter and the original flight controller unit that was originally mounted on the quadcopter to continuous vary the throttle command. The micro-Doppler frequency shifts are observed in the spectrogram when all propellers are rotating simultaneously at continuously varying speed. In the second set of measurements, a custom-designed flight controller unit is used in place of the original one. The WiFi module in the new flight controller allows for wireless remote control of all the motors individually in a MATLAB interface. The micro-Doppler frequency measurement results of multiple or a single propeller each rotating at a fixed speed are displayed in power spectra. The two sets of measurements are constructed using a combination of lab instrumentation with added custom hardware and firmware as shown in Fig. 6.7.

K-Band Radar Design

The fast-prototyped K-band radar system utilizes an Agilent E8257D signal generator to provide an X-band (8 – 13 GHz) continuous wave as a reference source for the system. Then the X-band signal is divided into two ways, one way is used as the input signal for the K-band transmitter and the other way serves as the LO input of the downcoverter in the receiver. In the transmit path, this X-band signal is multiplied by a Hittite HMC576 multiplier to a K-band signal and fed into the transmit horn antenna. And in the receive path, the K-band backscatter signal is directly downconverted to baseband by a Hittite HMC977LP4E I/Q demodulator with the X-band LO input from the signal generator. The baseband signal is then sampled by

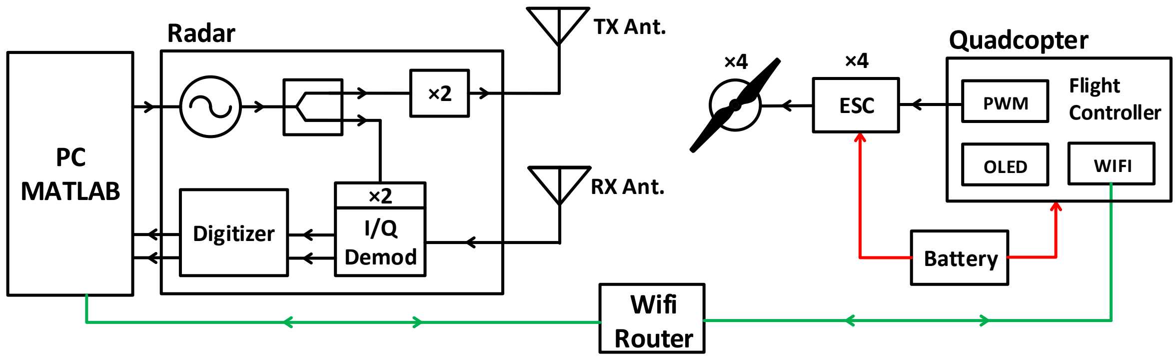

Figure 6.7: Schematic of the hardware connections in the micro-Doppler measurements. The custom-designed flight controller unit uses WiFi to interface with the computer.

an Agilent L4534A Digitizer and buffered to PC memory.

The HMC977 I/Q demodulator has an integrated $\times 2$ multiplier to convert the LO input signal to K-band, so the signal collected by the digitizer contains a strong DC component and much weaker Doppler frequency shifts at low analog frequencies. Both the signal generation and data collection are triggered and controlled by a computer using MATLAB interfaces. The system is pre-calibrated before running measurements for fixed or continuous varying rotation rates. Fig. 6.10 shows the measurement environment. As can be seen, all radar system hardwares are put on a cart that is placed outside the chamber during the measurement.

Custom Flight Controller Unit Design

The custom flight controller unit to set the rotation rate of each motor to a specfiic value is shown in Fig. 6.9. We choose the Adafruit Feather M0 microcontroller tripler kit and write our own firmware to realize wireless control of each motor rotation. The tripler kit consists of a main board of ARM Cortex M0 processor integrated with a 802.11bgn-capable WiFi module, an 8-Channel PWM or Servo FeatherWing board, and an OLED FeatherWing.

The User Datagram Protocol (UDP) is used for a WiFi connection between the flight controller unit and the computer. To start, the computer sends a command to arm the quadcopter through WiFi network and gets feedback from the flight controller unit saying if the quadcopter is ready for operation. Then a message containing rotation rate information of a particular propeller is sent from the PC and the microprocessor in the flight controller decodes this message and outputs a PWM signal to the specified ESC to drive the motor. Hence, different rotation rates can be achieved individually at the motors. Finally, after each measurement is finished, the computer sends an query signal to check if the quadcopter can be shut down.

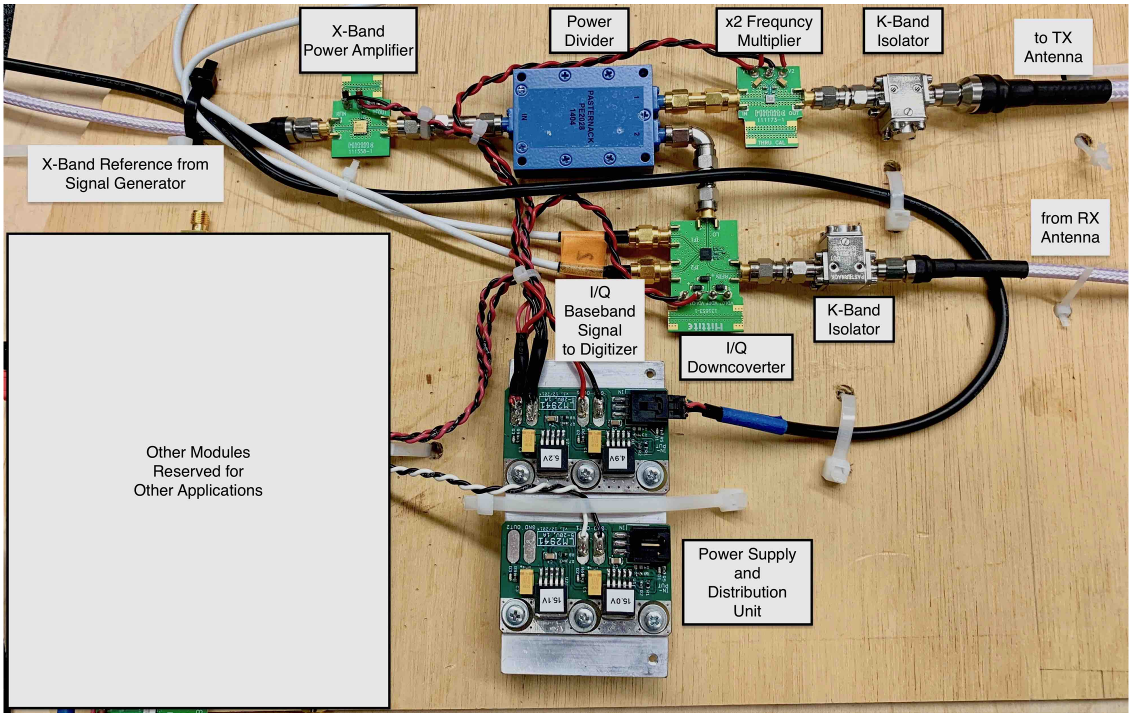

Figure 6.8: A photo of the custom-designed K-band radar front-end.

Figure 6.9: A photo of the custom-designed flight controller unit mounted on the quadcopter.

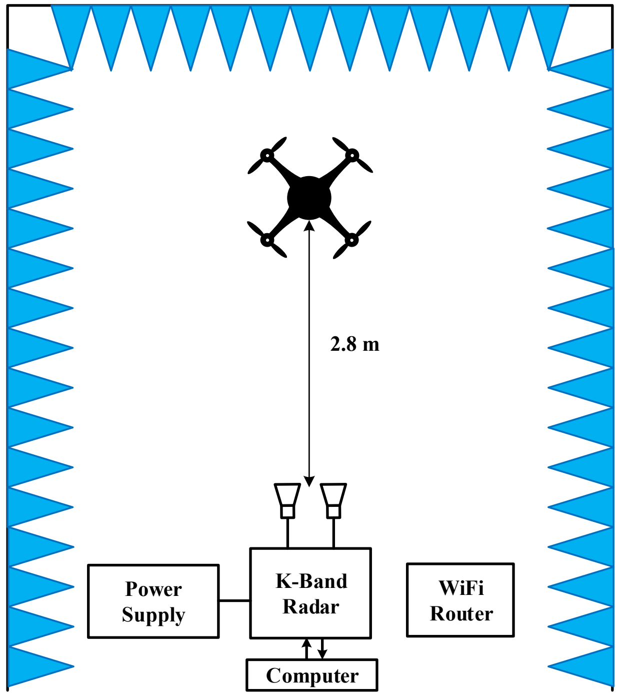

(a)

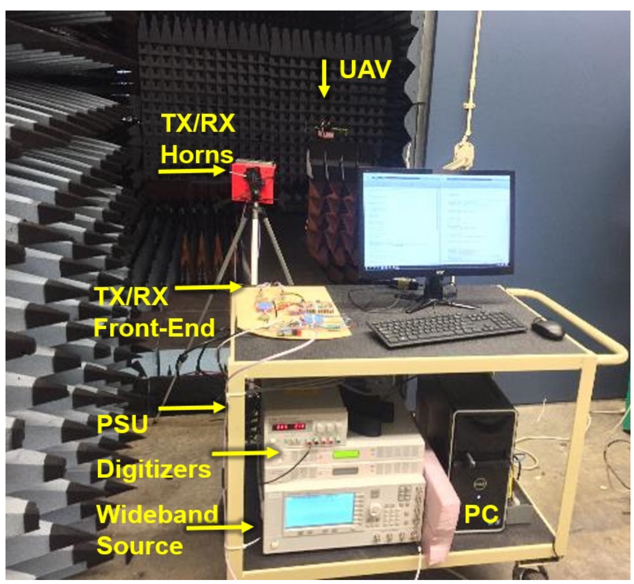

(b)

Figure 6.10: K-band micro-Doppler measurements in the chamber. (a) A schematic of the chamber measurement setup. (b) A Photo showing the measurement environment.

6.3.2 *Micro-Doppler Signatures of Continuously Varying Rotating Rates*

The micro-Doppler signatures are characterized at a fixed mid-band frequency of 20 GHz. Similar results are expected in the measurements with the same radar system at any carrier frequency in the available band of 16 – 26 GHz, and also in the analysis or modeling of signals.

Measurements

As seen in Fig. 6.10, the Turnigy SK450 is fixed on a tripod in the chamber about 2.8 m away from the antennas. The metals on the tripod are covered by absorbers to reduce unwanted scatterings and minimize multipath propagation. Before taking measurements with the remote control, the quadcopter needs to be powered on and all motors have to be armed by holding the throttle down and rudder right for 5 times. During each measurement, the signal generator outputs a carrier signal at 10 GHz with a power of 10 dBm and the digitizer samples the downcoverted receive signal at 50 kHz for 40 seconds.

We vary the throttle from minimum value to maximum, then decrease back to minimum, and repeat this cycle for another three times. And in comparison, we also sampled the backscatter signal when the throttle was fixed at the maximum level for 40 s. *These measurements are to find out the maximum rotation rate of the propellers at which this quadcopter can actually handle.*

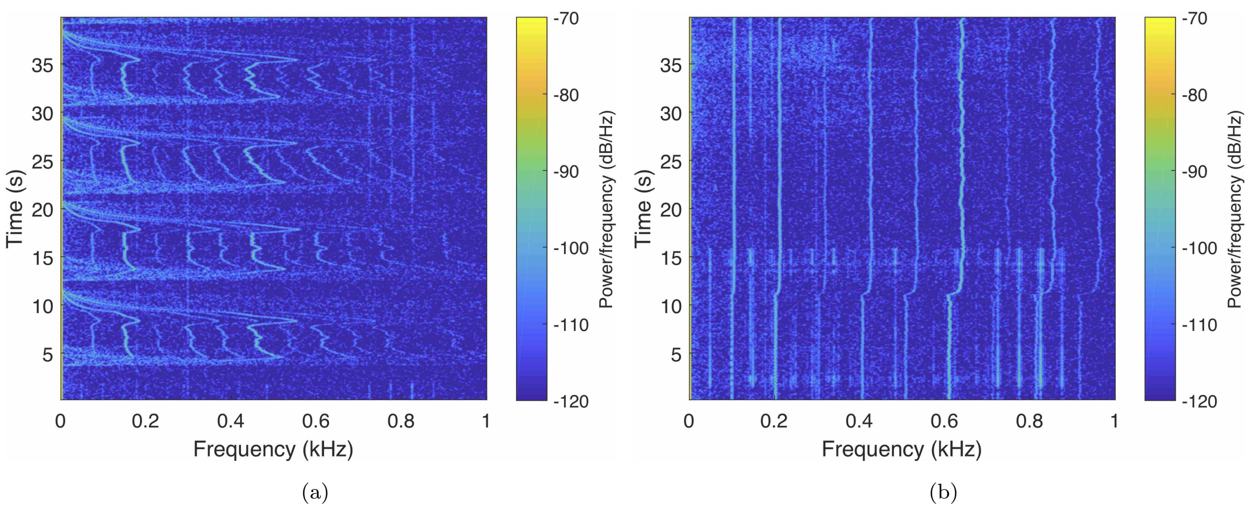

Figure 6.11: Spectrograms of the radar received signals. By using the stock remote control to continuously vary the rotation rate of all propellers, the maximum rotation rate at which the quadcopter can handle is found at 6500 rpm (corresponding to 108 Hz in the spectrogram). (a) Throttle varied from idle to max for four time in 40s. (b) Constant Throttle level over 40s.

Results Analysis

The single side band spectrograms (zoomed to $[0, 1]$ kHz) of the two measurements are shown in Fig. 6.11a and Fig. 6.11b respectively. It can be seen that the first harmonic of micro-Doppler frequency is reaching 108 Hz in both cases which gives a safe maximum rotation rate of 6500 rpm. And the fact that the modulated signal contains all the harmonics shown in the figures discloses the angle-modualtion nature of micro-Doppler signatures.

6.3.3 Micro-Doppler Signatures of Fixed Rotation Rates

After setting the maximum rotation rate of this quadcopter, controlled-speed measurements are carried out to first find out the dynamic radar cross section when four propellers are operating at a same speed, then compare the micro-Doppler signatures of two propellers in simultaneous and separate rotations, and in the end depict the frequency spectrum of a single propeller when it is rotating at different rates.

Dynamic RCS Equation

When the quadcopter was powered down, we measured and calculated its static radar cross section across the whole radar frequency band. Based on the same theory, the equation of dynamic radar cross section at the l-th frequency sample can be given as

$$\begin{aligned} \sigma_{l,\text{dynamic}}[i] =& \frac{P_\mathrm{r}[i](4\pi)^3 R_1^2 R_2^2}{P_\mathrm{t} G_\mathrm{t} G_\mathrm{r} \lambda_l^2} \\ =& \frac{\left\|\mathbf{y}_l[i]\right\|^2 (4\pi)^3 R_1^2 R_2^2 f_l^2}{G_\mathrm{t} G_\mathrm{r} c_0^2}. \end{aligned} \tag{6.2}$$

Since frequency response vecter $\mathbf{y}_l[i]$ is changing periodically, the dynamic RCS can be different when sampled at different times. We sample the backscatter signals over a long enough time and calculate the power spectral density of dynamic radar cross section within the sampling frequency bandwidth.

4-Propeller Measurement

Example measurements discussed here are same-speed 4-propeller operations in both top-view and edge-view configurations when the rotation rate is set to 4200 rpm. The harmonics are seen at up to 2 kHz in both side bands for both configurations. It is also observed that all frequency shifts are not exactly multiples of 70 Hz (corresponding to 4200 rpm). This is mainly because when all propellers start rotating together, the software of the quadcopter tries to stabilize it on the tripod and the rotation rates are slightly adjusted to a value different from 4200 rpm. Integrating the power density values from -2 kHz to 2 kHz, the total micro-Doppler RCS can be calculated as -7.8 dBsm for top-view configuration and -18.56 dBsm for edge-view configuration at 20 GHz, which are close to the static RCS values.

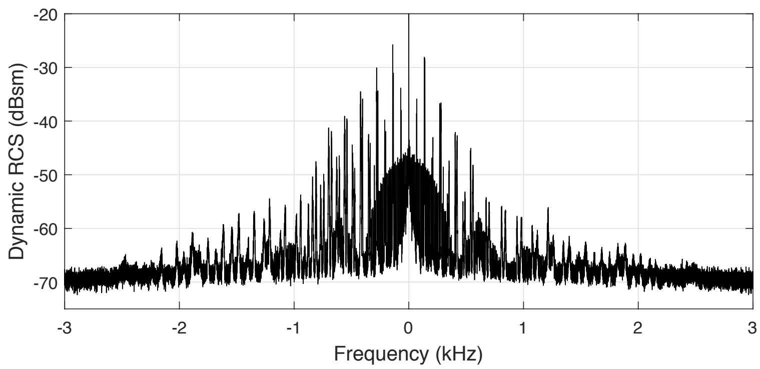

(a) Top-view configuration

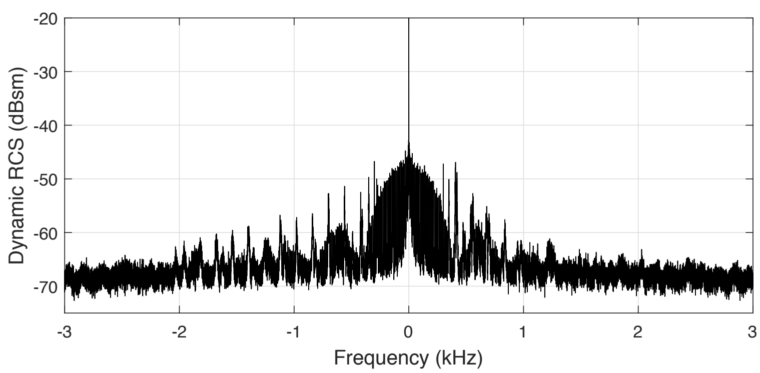

(b) Edge-view configuration

Figure 6.12: The Doppler power spectrum of dynamic radar cross sections measured with a radar carrier signal at 20 GHz when all four propellers are set to rotate at a rate of 4200 rpm.

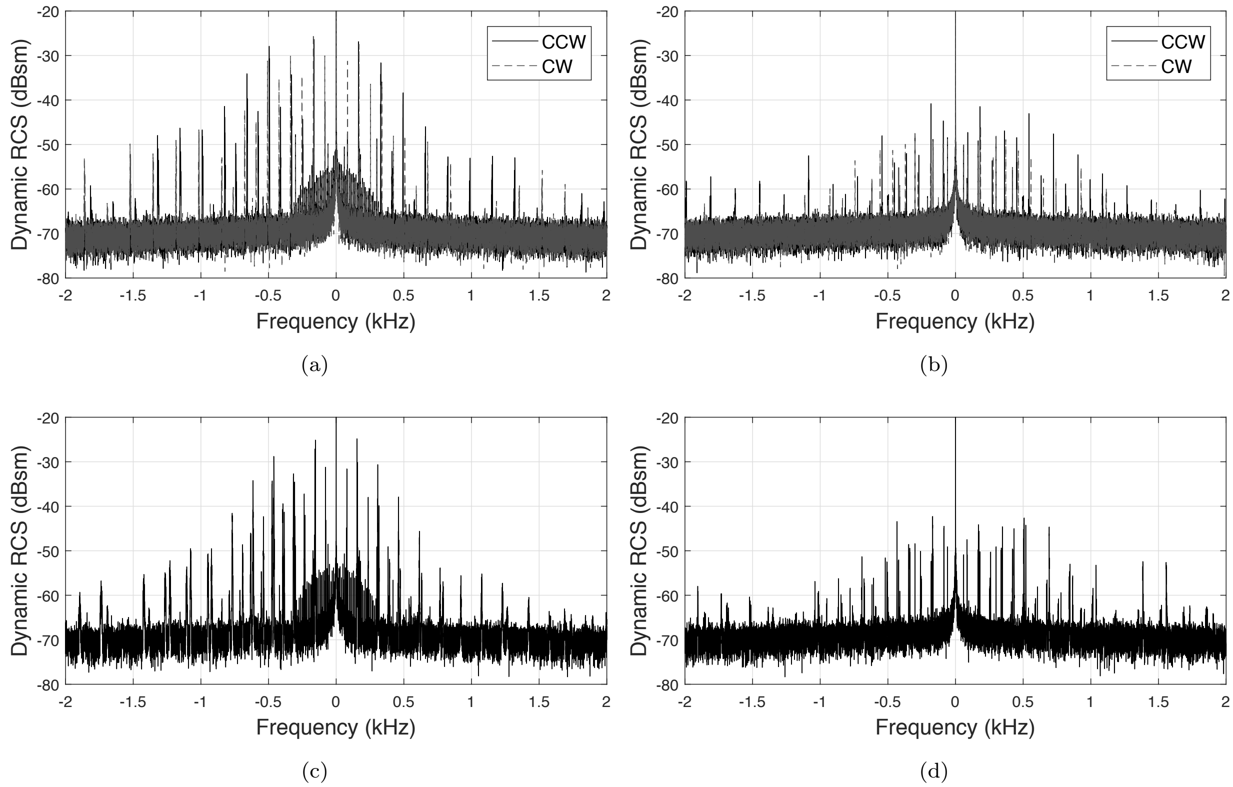

Figure 6.13: Dynamic RCS results in top-view configuration (rotation rate is approximately 5000 rpm): (a) displays two micro-Doppler power spectra of the two propellers when they are measured separately; (c) is the power spectrum when the two propellers are rotating simultaneously. Dynamic RCS results in edge-view configuration (rotation rate is approximately 5100 rpm): (b) separate rotations; (d) simultaneous rotation.

A 2-Propeller Measurement v.s. two 1-Propeller Measurements

To find out the interference between two propellers, especially between the two neighbouring propellers that have different rotation directions, measurements are implemented with one CW propeller and one CCW propeller that are set to first rotate separately then simultaneously in both top-view and edge-view configurations. And the two propellers are in a same distance to the measurement antennas. Fig. 6.13a and 6.13c display the dynamic RCS values in top-view configuration of separate and simultaneous rotations respectively when the rotation rate is set to 5000 rpm for both propellers. Fig. 6.13b and 6.13d display the dynamic RCS values in edge-view configuration when the rotation rate is approximately 5100 rpm. Both the upper and lower sidebands are zoomed to 2 kHz to better compare the results. It is seen that the power spectrum of simultaneous rotation is approximately an overlay of the two spectra of separate rotations.

1-Propeller Measurement

From the analysis above, the micro-Doppler signature of a quadcopter can be decomposed to the mechanically induced modulation of each propeller. By understanding the fundamental principle of how each propeller modulates the radar carrier signal, we will be able to learn more of the quadcopter behaviors from the backscatter signals. In this subsection, the micro-Doppler signature is observed on a single propeller that rotates at different rates from different viewpoints of the radar antenna.

In the top-view configuration, the propeller is measured at different rotation rates of 3000 rpm, 5000 rpm, and 6500 rpm respectively with a 20 GHz radar carrier signal. From their dynamic RCS results displayed in Fig. 6.14, there are harmonic Doppler shifts at multiples of 50 Hz, 83 Hz, and 108 Hz respectively in each plot. And the effective bandwidth above the noise floor is increasing with rotation rates. In all the three cases, the maximum dynamic RCS is observed to be above -30 dBsm. In comparison, the dynamic RCS results in edge-view measurements implemented at the same rotation rates are shown in Fig. 6.15. While the harmonic frequencies remain same, the effective bandwidths are much wider in the edge-view measurements but the maximum dynamic RCS values are about 20 dB lower than the measured dynamic RCS values in the top-view configuration.

An explanation of such differences can be: in edge-view configuration, the intensity of micro-motion looks higher from the radar which induces an angle modulation in more depth on the radar carrier signal; while in the top-view configuration, the reflectivity of the propeller looks higher to the radar, so there is a much higher amplitude modualtion with a rotation in top-view configuration.

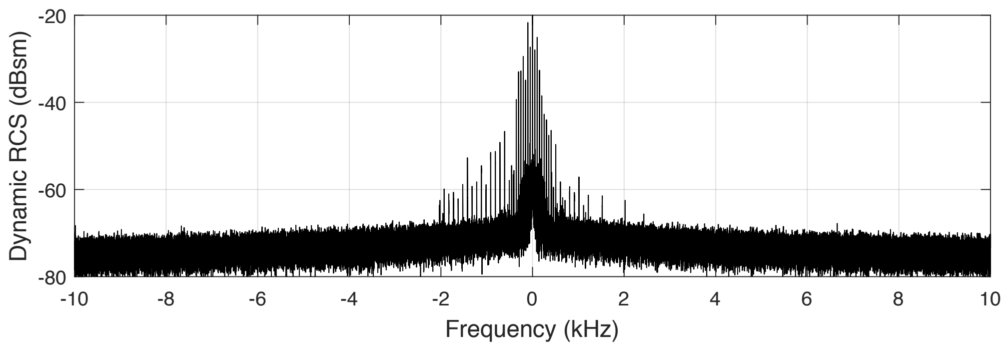

(a)

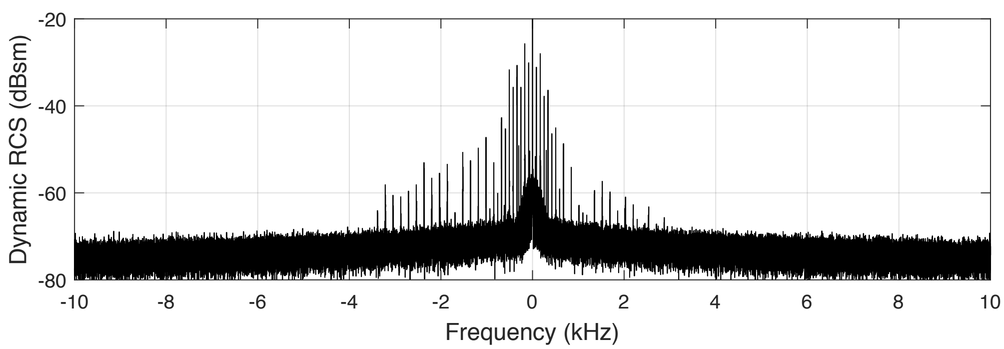

(b)

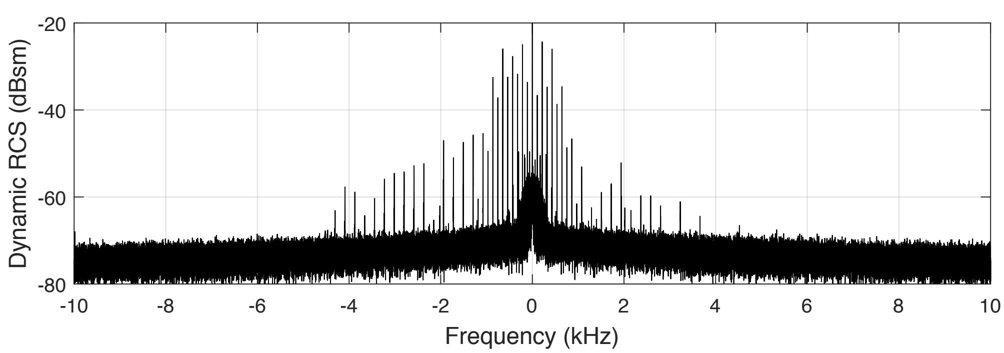

(c)

Figure 6.14: The Doppler power spectra of dynamic radar cross sections measured with a radar carrier signal at 20 GHz when one propeller is rotating in top-view configuration at a rate of (a) 3000 rpm; (b) 5000 rpm; (c) 6500 rpm.

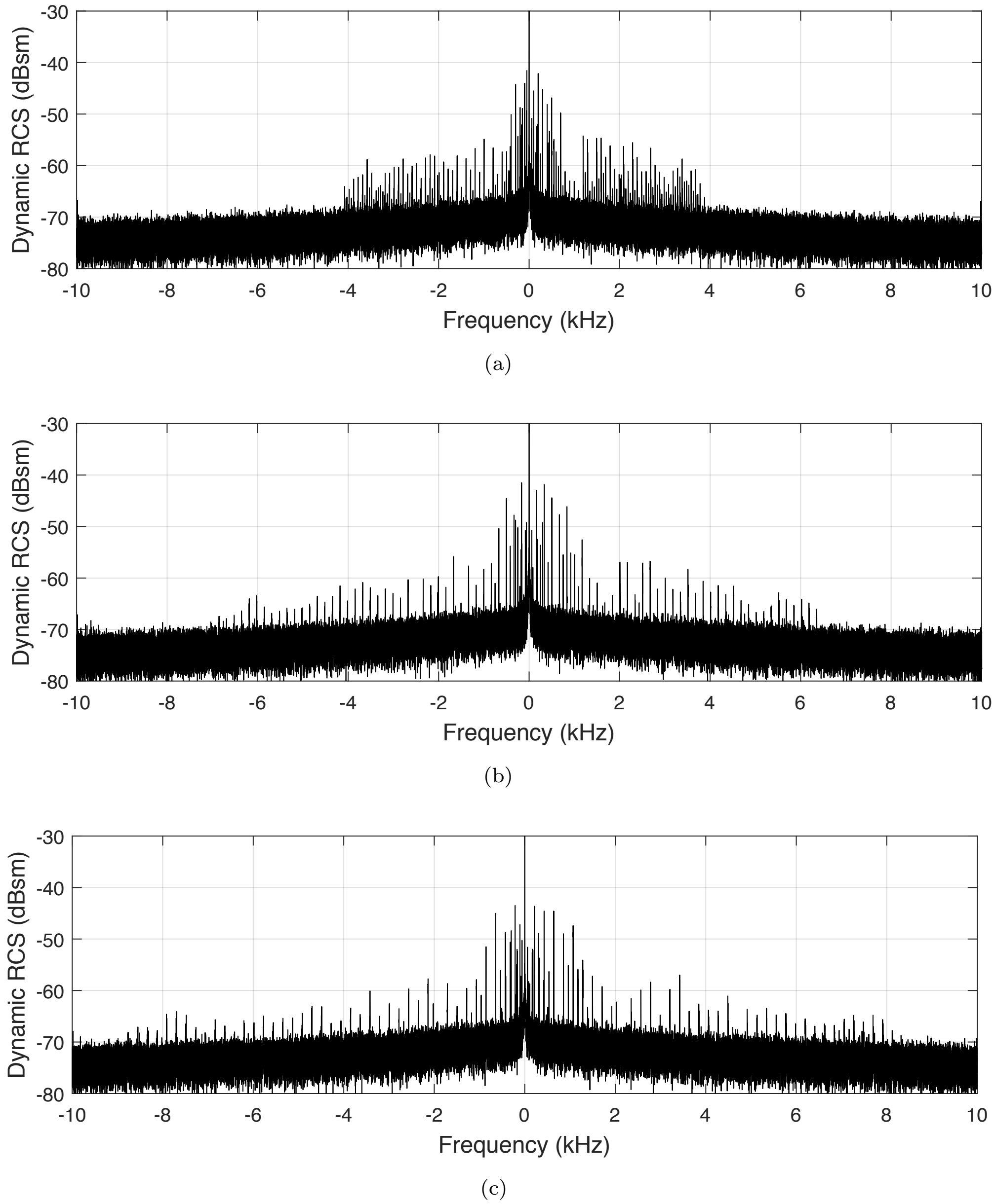

Figure 6.15: The Doppler power spectra of dynamic radar cross sections measured with a radar carrier signal at 20 GHz when one propeller is rotating in edge-view configuration at a rate of (a) 3000 rpm; (b) 5000 rpm; (c) 6500 rpm.

6.4 Chapter Conclusion

In this chapter, different radar systems and a custom-designed flight controller unit are used in the characterization of the reflectivity, static and dynamic radar cross sections, and micro-Doppler signatures of the Turnigy SK450 quadcopter. Important observations are summarized as follows:

- by leveraging 3D SAR imaging technologies, it is found that around 27.8% of the total backscatter signal power from the quadcopter is due to scatterings from the propellers and motors;
- the static RCS of the Turnigy SK450 over the $15 - 26.5$ GHz bandwidth is between -20 dBsm to -8 dBsm, similar to the RCS of a bird;
- the micro-Doppler (dynamic) RCS of Turnigy SK 450 at 20 GHz in mid-speed operation is -7.8 dBsm in top-view configuration and -18.56 dBsm in edge-view configuration;
- the interference between propellers does not contribute to the overall micro-Doppler signature; the Doppler power spectrum of simultaneous rotation is approximately an overlay of the spectra of separate rotations;
- the effective Doppler bandwidth of the same rotation is wider in edge-view configuration and narrower in top-view configuration; the dynamic RCS value, on the contrary, is higher in top-view configuration and lower in edge-view.

These results give us some basic knowledge of the micro-Doppler signatures of different quadcopters operations. Next, complex-valued point scatterers will be used in the modeling of different propeller behaviors to better explain the differences in Doppler bandwidth and dynamic RCS between the two different configurations, and help us achieve a more fundamental understanding on the mechanisms of micro-motion induced modulation.

Chapter 7

MICRO-DOPPLER SIGNATURE OF A SPINNING PROPELLER MODELED WITH POINT SCATTERERS

This chapter, based on the observations and analysis of the whole quadcopter, decomposes micro-Doppler signatures to the contribution of point scatterers on the modulation of radar carrier signals. With limited numbers of point scatterers modeling different propeller rotations, we can understand the previous measurement results more quantitatively and spread the conclusions and theories to other uncooperative targets that have periodic micro-motions.

By using this frequency response model from uncooperative targets

$$y_l[i] = \sum_{n=1}^{N} \rho_n \alpha_{l,n}^2[i] e^{-j2\pi f_l \frac{2\left\|\vec{\mathbf{R}}[i]+\vec{\mathbf{r}_n}[i]\right\|}{c_0}} + \nu_l[i] \tag{7.1}$$

we are able to achieve these goals:

- find out how the motion of each point scatterer modulates the amplitude and angle of carrier signals;
- mathematically analyze the bandwidth and amplitude of the received modulated signal for both the top-view and edge-view configurations;
- leverage the 3-D SAR imaging technologies to learn the reflectivity and distribution of point scatterers in a reflective propeller;
- and finally, use limited number of point scatterers to model different rotations of a propeller, reconstruct the Doppler power spectrum, and match with the measurement results.

7.1 *The Modulation Nature of Micro-Doppler Signature*

7.1.1 Amplitude Modulation and Angle Modulation by a Sinusoidal Signal

To fully understand the modulation mechanisms and schemes in micro-Doppler effects and interpret how the point scatterers in an uncooperative target modulate radar carrier signals, it is necessary to first review the amplitude modulation and angle modulation in analog signal transmissions.

Amplitude modulation is the process that a function of a message signal becomes the amplitude of a carrier signal. Suppose that the carrier signal $c(t)$ and modulating signal $m(t)$ are sinusoids of the forms [92]

$$\begin{aligned} c(t) &= A_c \cos(2\pi f_c t) \\ m(t) &= a \cos(2\pi f_m t) \qquad \text{for AM,} \end{aligned}$$

where A_c is the carrier amplitude, f_c is the carrier frequency, a is the amplitude of the modulating signal, and f_m is the modulating signal frequency. Thus, the amplitude modulated signal is

$$\begin{aligned} u_{\text{AM}}(t) = m(t)c(t) =& A_c a \cos(2\pi f_c t) \cos(2\pi f_m t) \\ =& \frac{A_c a}{2} \left[\cos\left(2\pi\left(f_c - f_m\right)t\right) + \cos\left(2\pi\left(f_c + f_m\right)t\right)\right]. \end{aligned} \tag{7.2}$$

The modulated signal in the frequency domain will have this form

$$\begin{aligned} U_{\text{AM}}(f) =& \frac{A_c}{2}\left[M(f - f_c) + M(f + f_c)\right] \\ =& \frac{A_c a}{4}\left[\delta(f - f_c + f_m) + \delta(f - f_c - f_m) + \delta(f + f_c - f_m) + \delta(f + f_c + f_m)\right]. \end{aligned} \tag{7.3}$$

Therefore, after AM modulation, the spectrum of the modulating signal is shifted in frequency by the carrier frequency. And the bandwidth of modulated signal becomes two times of the bandwidth of modulating signal.

In angle modulation, the message signal changes the frequency or the phase of the carrier signal. Suppose the modulating signal for frequency modulation and phase modulation are

$$\begin{aligned} m(t) &= a \sin(2\pi f_m t) \qquad \text{for PM} \\ m(t) &= a \cos(2\pi f_m t) \qquad \text{for FM.} \end{aligned}$$

Then the modulated signal for both PM and FM is

$$\begin{aligned} u_{\text{PM or FM}}(t) =& A_c \cos\left(2\pi f_c t + \beta \sin\left(2\pi f_m t\right)\right) \\ =& \sum_{q=0}^{\infty} A_c J_q(\beta) \cos(2\pi(f_c \pm q f_m)t), \end{aligned} \tag{7.4}$$

where β is the modulation index and $J_q(\beta)$ is the Bessel function of the first kind of order q. In the frequency domain, the modulated signal is written as

$$U_{\text{PM or FM}}(f) = \frac{A_c}{2} \sum_{q=0}^{\infty} J_q(\beta)\left[\delta(f - f_c \pm q f_m) + \delta(f + f_c \pm q f_m)\right]. \tag{7.5}$$

Therefore, the frequency spectrum of the modulated signal contains harmornics at $f_c \pm q f_m$ for $q = 0, 1, 2, \cdots$, with an envelope following the Bessel function. And the effective bandwidth is given by Carson's rule as

$$B = 2(\beta + 1) f_m. \tag{7.6}$$

7.1.2 Modulation Induced by Micro-Motions

In a radar view of the AM, FM, or PM modulation, the radar transmit signal is the carrier signal, the response from the wireless channel containing modulated targets can be seen as the message signal, and the received radar signal is the modulated signal. As proposed previously, the frequency response of a channel containing uncooperative targets, using the Born approximation for scattering (considering only the first-order scatterings), has the expression of

$$\begin{aligned} y_l[i] &= \sum_{n=1}^{N} \rho_n \alpha_{l,n}^2[i] e^{-j2\pi f_l \frac{2\left\|\vec{\mathbf{R}}[i]+\vec{\mathbf{r}_n}[i]\right\|}{c_0}} + \nu_l[i] \\ &= \sum_{n=1}^{N} |\rho_n| \, e^{j\psi_n} \alpha_{l,n}^2[i] e^{-j2\pi f_l \frac{2\left\|\vec{\mathbf{R}}[i]+\vec{\mathbf{r}_n}[i]\right\|}{c_0}} + \nu_l[i] \\ &= \sum_{n=1}^{N} |\rho_n| \, \alpha_{l,n}^2[i] e^{-j2\pi f_l \left(\frac{2\left\|\vec{\mathbf{R}}[i]+\vec{\mathbf{r}_n}[i]\right\|}{c_0} - \frac{\psi_n}{2\pi f_l}\right)} + \nu_l[i], \end{aligned} \tag{7.7}$$

where $-2\pi \le \psi_n \le 2\pi$ is the phase of the complex reflection coefficient of the n-th point scatterer. From this equation, we see that the target and wireless channel modulate a radar transmit signal by having each point scatterer change both the amplitude and phase of the carrier signal. Therefore, with each point scatterer, there are two message signals:

$$\begin{aligned} m_{n,1}(t) &= |\rho_n| \, \alpha_{l,n}^2(t), \\ m_{n,2}(t) &= -\, 2\pi f_l \left(\frac{2\left\|\vec{\mathbf{R}}(t) + \vec{\mathbf{r}_n}(t)\right\|}{c_0} - \frac{\psi_n}{2\pi f_l}\right) \approx -2\pi f_l \frac{2\left\|\vec{\mathbf{R}}(t) + \vec{\mathbf{r}_n}(t)\right\|}{c_0}, \end{aligned} \tag{7.8}$$

where according to Eq. 2.13, the monostatic loss factor is

$$\alpha_{l,n}^2(t) = \frac{c_0 G(t)}{4\pi f_l \left\|\vec{\mathbf{R}}(t) + \vec{\mathbf{r}_n}(t)\right\|^2} \sqrt{\frac{1}{4\pi}}. \tag{7.9}$$

The monostatic antenna gain G in the direction of point scatterer is also changing over time due to antenna polarization and directivity. An example can be found in Fig. 7.1 where the n-th point scatterer is in a circular rotation about an axis in an arbitrary direction of $\hat{\mathbf{n}}$. The angle of antenna looking at the point scatterer also has a sinusoidal pattern. In message signal $m_{n,2}(t)$, the phase ψ_n is several orders smaller than the microwave frequency f_l, so its impact on the phase of carrier signal can be ignored.

Suppose the radar transmit signal at frequency f_l is in the form of

$$s_l(t) = A_l \cos(2\pi f_l t),$$

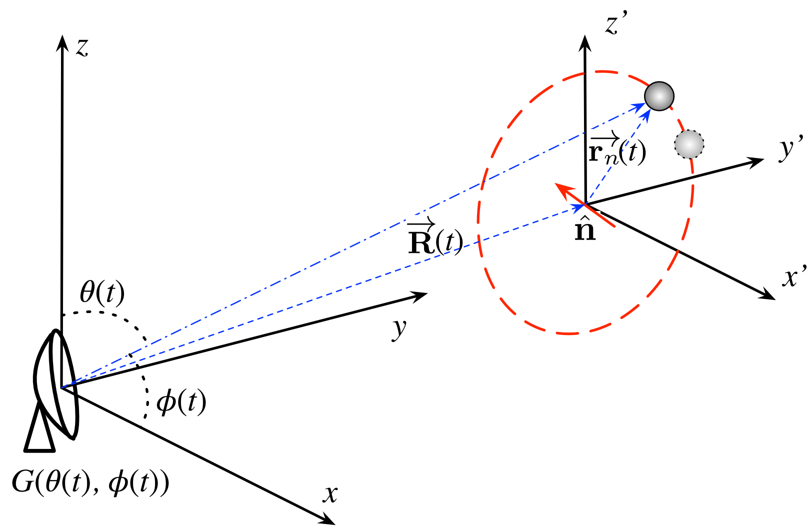

Figure 7.1: A point scatterer rotating about an axis in direction of $\hat{\mathbf{n}}$.

where A_l is the radar carrier signal amplitude, then the received signal backscattered from the n-th point scatterer is

$$r_{n,l}(t) = A_l\ m_{n,1}(t)\ \cos(2\pi f_l t + m_{n,2}(t)). \tag{7.10}$$

Thus, the total backscatter signal received at the radar is

$$\begin{aligned} r_l(t) = \sum_{n=1}^{N} r_{n,l}(t) = \sum_{n=1}^{N} A_l\ m_{n,1}(t)\ \cos(2\pi f_l t + m_{n,2}(t)) \\ = A_l \sum_{n=1}^{N} |\rho_n| \frac{c_0 G(\theta(t), \phi(t))}{4\pi f_l \left\| \overrightarrow{\mathbf{R}}(t) + \overrightarrow{\mathbf{r}_n}(t) \right\|^2} \sqrt{\frac{1}{4\pi}}\ \cos\left(2\pi f_l t - 2\pi f_l \frac{2\left\| \overrightarrow{\mathbf{R}}(t) + \overrightarrow{\mathbf{r}_n}(t) \right\|}{c_0}\right). \end{aligned} \tag{7.11}$$

We can see that the uncooperative target modulates a radar carrier signal in a way that each of its point scatterer has both amplitude and frequency modulations to the carrier signal independent of other point scatterers. And each frequency modulating signal is a function of the motion of the point scatterer, while the amplitude modulating signal is a function of both the motion and the magnitude of reflection coefficient.

If the point scatterers have periodic micro-motions, e.g. rotations (as shown in Fig. 7.1), then $G(\theta(t), \phi(t))$ and $\left\| \overrightarrow{\mathbf{R}}(t) + \overrightarrow{\mathbf{r}_n}(t) \right\|$ both have sinusoidal-like patterns. The analysis of micro-Doppler frequencies of each point scatterer and the envelope in the spectrum can then reference the amplitude-modulated signal in Eq. 7.3 and the angle-modulated signal in Eq. 7.5, that there will be spectral lines around the carrier frequencies with spacing of harmonic rotation frequencies and the magnitude of each spectral line is a multiplication of Bessel function and half of the magnitude of amplitude-modulating signal.

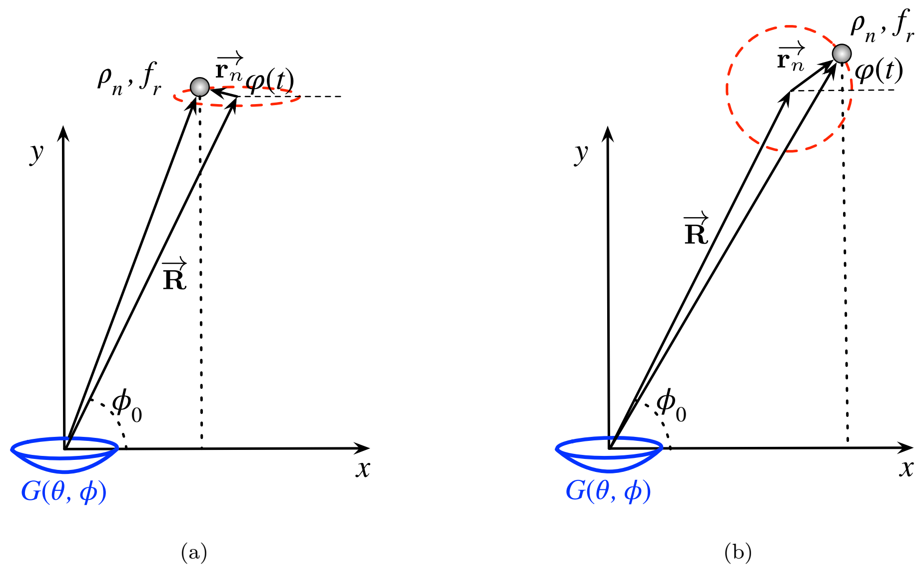

Figure 7.2: Two special cases of rotating point scatterers. In both cases, the rotation centers are stationary and fixed to the same height as the antenna center. (a) The rotation plane is vertical to the ground and parallel to the antenna aperture. (b) The rotation is in a horizontal plane.

7.1.3 Two Special Cases of Rotation

Next we consider two special cases of rotating point scatterers. In the first case, the point scatterer is rotating in a vertical plane parallel to the antenna aperture which resembles our top-view measurements (see Fig. 7.2a). In the second case, a point scatterer is rotating in a horizontal plane (see Fig. 7.2b), as close to the edge-view configuration. In both cases, the rotation centers are stationary and fixed to the same height as the antenna centers. After figuring out the received signals modulated by these two scatterers, more point scatterers with similar behaviors can be used in the modeling of propellers and the resulting micro-Doppler frequency spectra at different rotation rates can be used to correlate with the measurement results.

In these two special cases, the range vector $\vec{\mathbf{R}}$ is not changing over time, and the antenna gain is assumed to be constant when there is only a small change in the spherical angle θ or ϕ. So the received signal backscattered from an arbitrary point scatterer in either case is

$$r_{n,l}(t) = A_l \, |\rho_n| \, \frac{c_0 G(\frac{\pi}{2}, \phi_0)}{4\pi f_l \left\| \vec{\mathbf{R}} + \vec{\mathbf{r}_n}(t) \right\|^2} \sqrt{\frac{1}{4\pi}} \cos\left(2\pi f_l t - 2\pi f_l \frac{2 \left\| \vec{\mathbf{R}} + \vec{\mathbf{r}_n}(t) \right\|}{c_0} \right), \tag{7.12}$$

in which the unknown distance from the antenna phase center to the point scatterer has to be determined.

This distance in top-view configuration can be calculated from the geometry as

$$\begin{aligned}\left\|\vec{\mathbf{R}}+\vec{\mathbf{r}_n}(t)\right\|_{\text{top}} &= \sqrt{(R\cos\phi_0+r_n\cos\varphi(t))^2+(R\sin\phi_0)^2+(r_n\sin\varphi(t))^2}\\ &= \sqrt{R^2+r_n^2+2Rr_n\cos\phi_0\cos\varphi(t)}\\ &\approx \sqrt{R^2+r_n^2}+4r_n\cos\phi_0\cos\varphi(t)\end{aligned} \tag{7.13}$$

and in edge-view

$$\begin{aligned}\left\|\vec{\mathbf{R}}+\vec{\mathbf{r}_n}(t)\right\|_{\text{edge}} &= \sqrt{(R\cos\phi_0+r_n\cos\varphi(t))^2+(R\sin\phi_0+r_n\sin\varphi(t))^2}\\ &= \sqrt{R^2+r_n^2+2Rr_n\cos(\varphi(t)-\phi_0)}\\ &\approx \sqrt{R^2+r_n^2}+2r_n\cos(\varphi(t)-\phi_0)\end{aligned} \tag{7.14}$$

where the rotation angle $\varphi(t)$ is a function of the rotation frequency f_r and starting angle φ_0 as

$$\varphi(t)=2\pi f_r t+\varphi_0. \tag{7.15}$$

It is seen from Eq. 7.13 and Eq. 7.14, if a point scatterer is rotating about a center first in a vertical plane and then in a horizontal plane, then the modulation bandwidth about a high carrier frequency induced by the vertical rotation is smaller by a factor of $2\cos\phi_0$ compared to horizontal rotation (according to Eq. 7.6). This generally explains why the Doppler bandwidth in top-view measurement is much smaller than the same rotation rate in edge-view measurement. When the antenna is directly facing the rotation circle ($\phi_0 = 90°$), there is no angle modulation in the top-view configuration.

With the received signals from an arbitrary point scatterer in the two rotation planes derived above, the next step is to find out how many point scatterers are adequate to represent the propeller and determine their reflection coefficient values.

7.2 *The Nonuniform Distribution of Point Scatterers in a Single Propeller*

In this section, we leverage the same 3-D SAR imaging apparatus at K-Band (15 – 26.5 GHz) as used in the imaging of quadcopter to achieve a 3-D reflectivity profile of a 8045R CCW carbon-fiber propeller.

As shown in Fig. 7.3a, the propeller consists of two blades and a central hub to which the blades are attached. The upper surface ("face") of the blade is curved, while the other surface ("back") is flat. On each blade, the thick edge that cuts and slices into the air as propeller rotates is called a leading edge and the edge adjacent to the hub is the trailing edge. The blade has an angle to the plane normal to rotation axis. This angle is not the same throughout the length of the blade because the various sections of the blade travel at different speeds.

We extract a top-view image of just the CCW propeller from the image of the whole quadcopter in Fig. 6.5c, and display the results in Fig. 7.3b. To fully disclose the point scatterer distribution on both

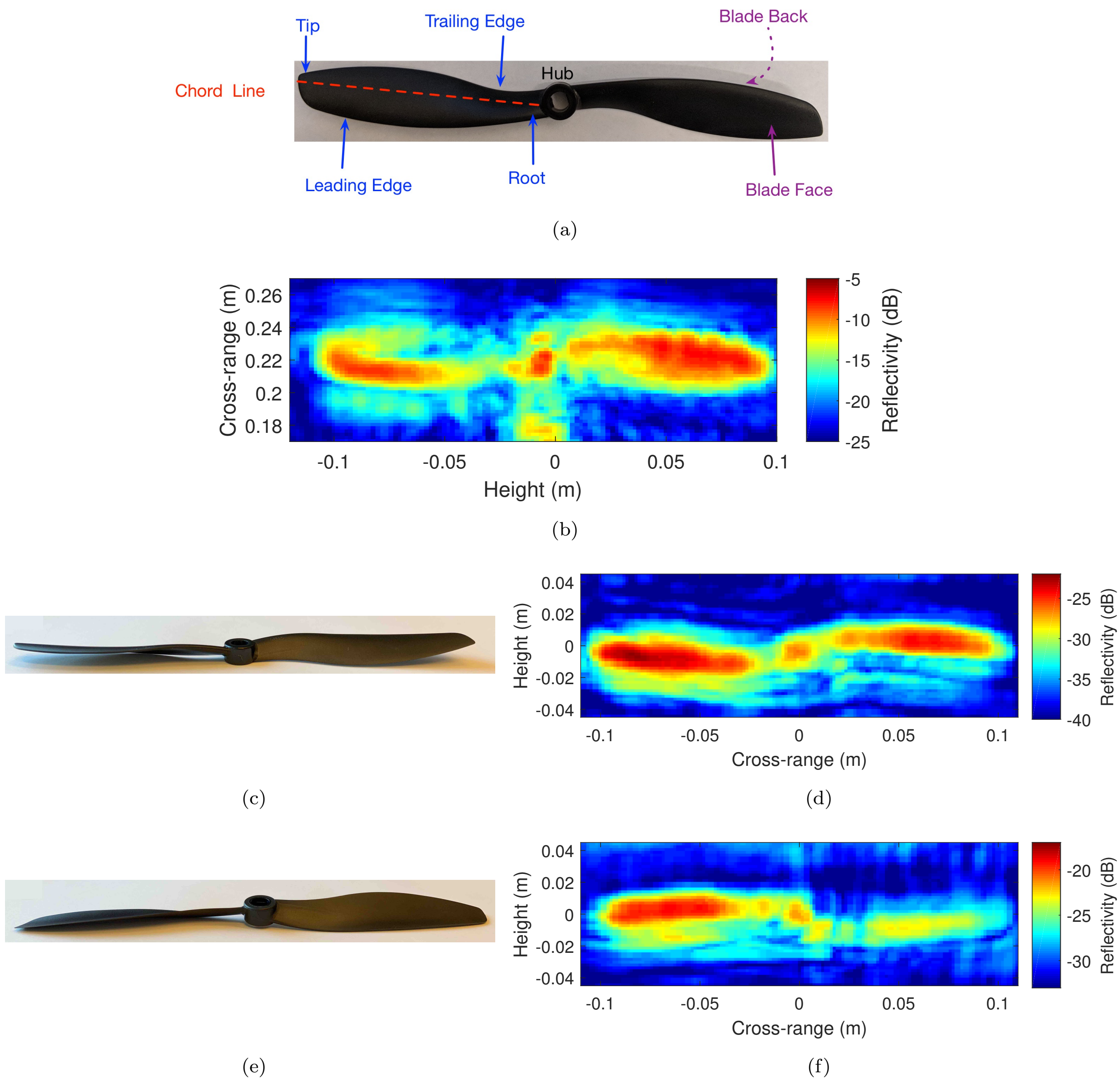

Figure 7.3: (a) The composition of a 8045R CCW propeller. (b) An image of the CCW propeller extracted from the top-view image of the quadcopter. (c) The CCW propeller is placed in a horizontal plane with face side directing upward. The photo is taken from the viewpoint of antenna. (d) A SAR image of the CCW propeller in edge-view configuration when face side is upward. (e) The CCW propeller is placed with the back side directing upward. (f) A SAR image of the upside down propeller. *Courtesy of Dr. Claire M. Watts at University of Washington.*

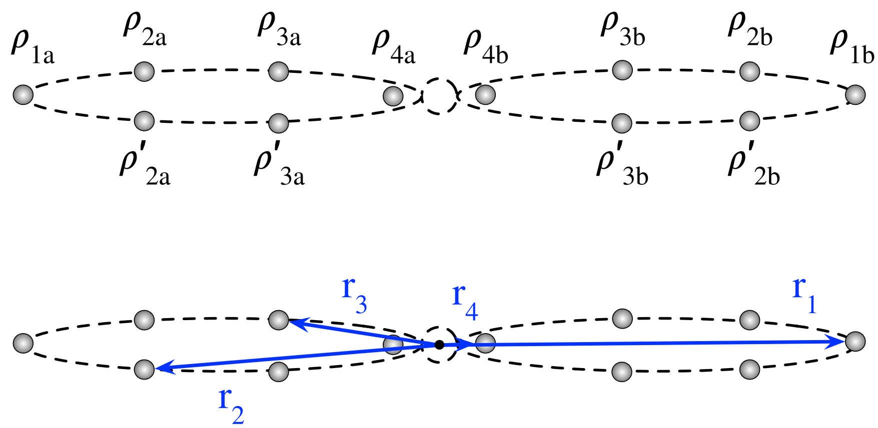

Figure 7.4: The point scatterers selected to represent the CCW propeller.

face side and back side of the blade for edge-view characterization, the CCW propeller is first placed in a horizontal plane with the face directing upward (see Fig. 7.3c), then turned upside down with the back directing upward (see Fig. 7.3e). This agrees with the truth that when a propeller is rotating about a vertical axis, the antenna always look at the face and trailing edge of one blade and the back and leading edge of the other blade.

During the measurement, the antennas look at the propeller in the edge-view perspective and the two blades are in same distance to the horizontal motion stage. By moving the antennas in two directions along the motion stages, 3-D SAR images of the propeller can be reconstructed to show the reflectivity. Averaging the absolute reflectivity values in the range direction gives 2-D overlapping reflectivity profiles as shown in Fig. 7.3d and Fig. 7.3f. As can be seen in the images, there is more scattering from the leading edges of the propeller than from the trailing edges and hub, because that is where many point scatterers are aggregated. The results can be referenced when choosing the number and positions of point scatterers for simulation.

7.3 *The Modeling of Rotating Propellers*

7.3.1 Selection of Point Scatterers

A number of point scatterers are selected to model the micro-Doppler signature of the propeller. Since there are different scatterings when looking at the propeller from different angle and on different surfaces or edges, two point scatterers are chosen to represent the reflectivity of each edge. A point scatterer is also used for each blade tip and root. The placements of the six scatterers on one blade are symmetric to their counterparts on the other blade about the hub center. For an initial modeling, the propeller is considered as a flat surface, so all the point scatterers are in a same vertical or horizontal plane in top-view or edge-view characterization. Their radii and rotation start angles are listed in Table 7.1.

7.3.2 Simulation and Correlation to Measurement Results

To model the micro-Doppler signature of a single propeller with point scatterers, the same parameter values from the measurements are used in simulations for the sampling rate, measurement time, the radar carrier frequency, transmitter output power, antenna gain, range vector from radar antenna to the target, and the calibrated radar receiver conversion gain. A Monte Carlo approach has been applied to the modeling.

In each simulation, the reflection magnitude of each point scatterer is randomly assigned between zero and one. And the sum of received signals from the twelve point scatterers is used to calculate the dynamic RCS in power spectrum and compare with the measurement results. After a number of simulation runs, some combinations of reflectivity values are found to match the trend of the envelope in measured power spectra. Examples of the simulated power spectra in comparison to the measurements at different rotation rates are given in Fig. 7.6 and Fig. 7.8 for the two configurations, and the reflectivity magnitude values used in the one simulation run are shown in Table 7.1. It is seen that the reflectivity values used in top-view simulation to match the measurement results are much higher than the ones used in edge-view configuration. This also proves that the higher dynamic RCS measured in top-view configuration is due to the much higher reflectivity of the blade faces in the top view, compared to the blade edges in edge-view configuration. The maximum RMS error across all harmonic components in top-view configuration is 8 dB, found at 6500 rpm. The maximum error in edge-view configuration is 7 dB at 6500 rpm.

Table 7.1: Starting angle, radius, and reflectivity magnitude of each point scatterer in one simulation run

Reflection Coeffiecient	ρ_{1a}	ρ_{1b}	ρ_{2a}	ρ'_{2a}	ρ_{2b}	ρ'_{2b}
r_n	$r_1 = 0.1$ m		$r_2 = 0.07$ m			
Starting φ	180°	0°	175°	$-175°$	5°	$-5°$
$\|\rho_n\|$ in Top-View	0.2050	0.5203	0.1306	0.9027	0.7290	0.5862
$\|\rho_n\|$ in Edge-View	0.0560	0.0294	0.0397	0.0150	0.0138	0.1497
Reflection Coeffiecient	ρ_{3a}	ρ'_{3a}	ρ_{3b}	ρ'_{3b}	ρ_{4a}	ρ_{4b}
r_n	$r_3 = 0.04$ m				$r_4 = 0.01$ m	
Starting φ	170°	$-170°$	10°	-10°	180°	0°
$\|\rho_n\|$ in Top-View	0.8022	0.9232	0.5770	0.2022	0.6186	0.2024
$\|\rho_n\|$ in Edge-View	0.2719	0.2923	0.2234	0.0288	0.1859	0.0528

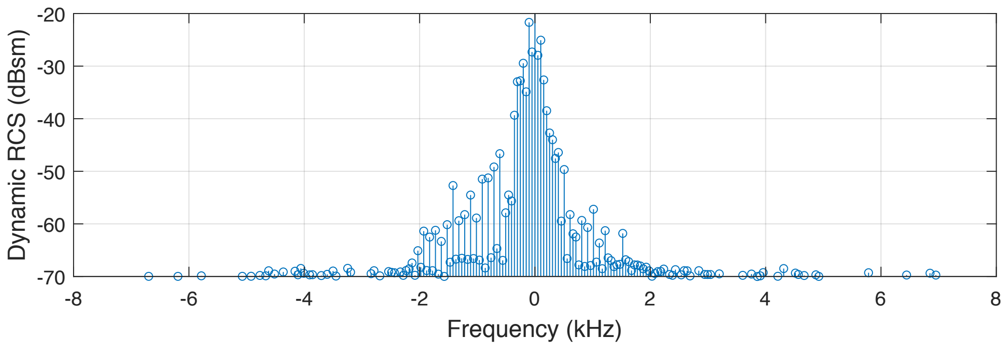

(a)

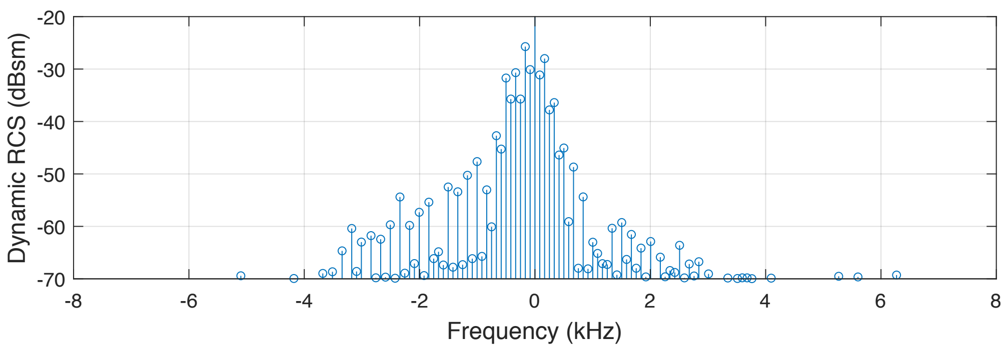

(b)

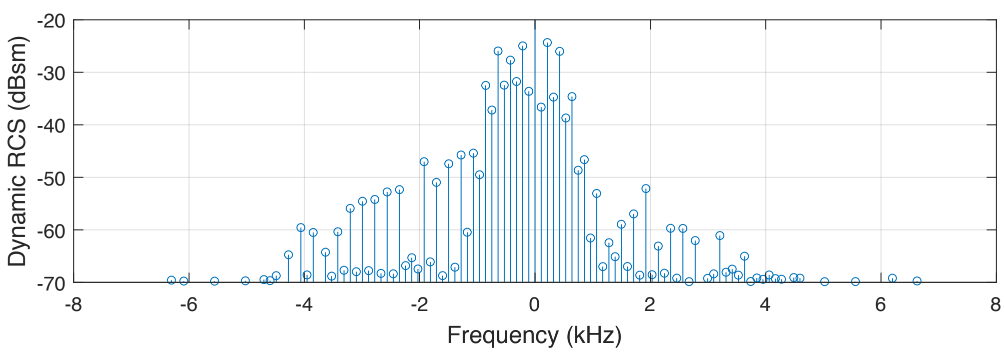

(c)

Figure 7.5: Re-plot the dynamic RCS results of one spinning propeller in top-view configuration to just show the harmonic Doppler frequencies. The rotation rates are: (a) 3000 rpm; (b) 5000 rpm; and (c) 6500 rpm. Both side bands are zoomed to 8 kHz to show the significant spectral lines at harmonic Doppler frequencies.

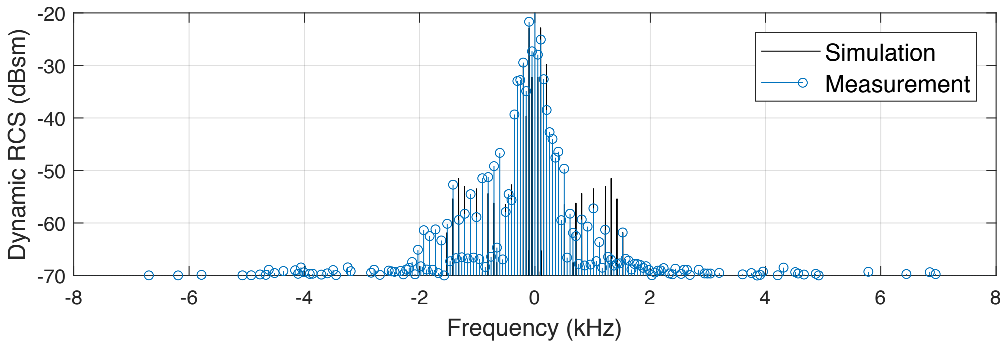

(a)

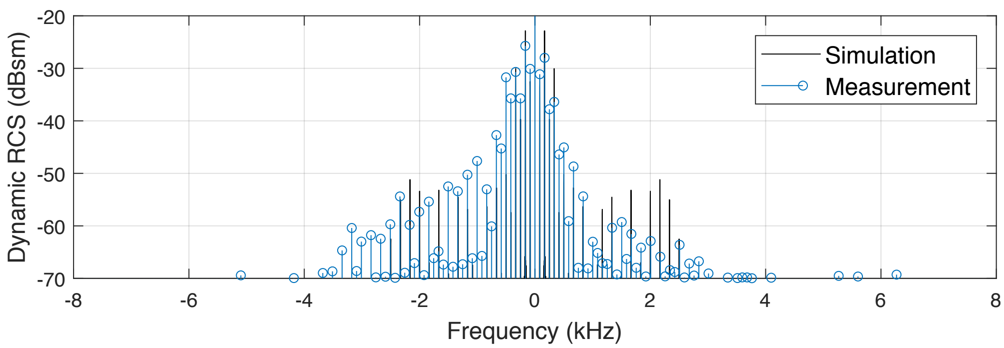

(b)

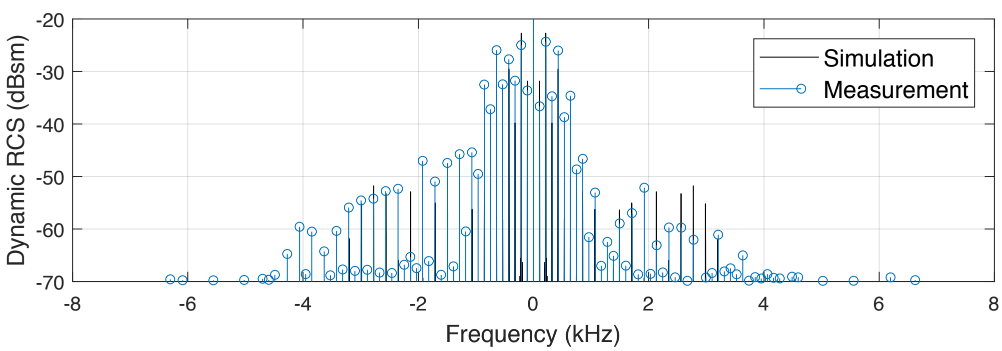

(c)

Figure 7.6: A comparison between simulated and measured dynamic RCS results of one propeller in top-view configuration when the rotation rates are: (a) 3000 rpm; (b) 5000 rpm; and (c) 6500 rpm.

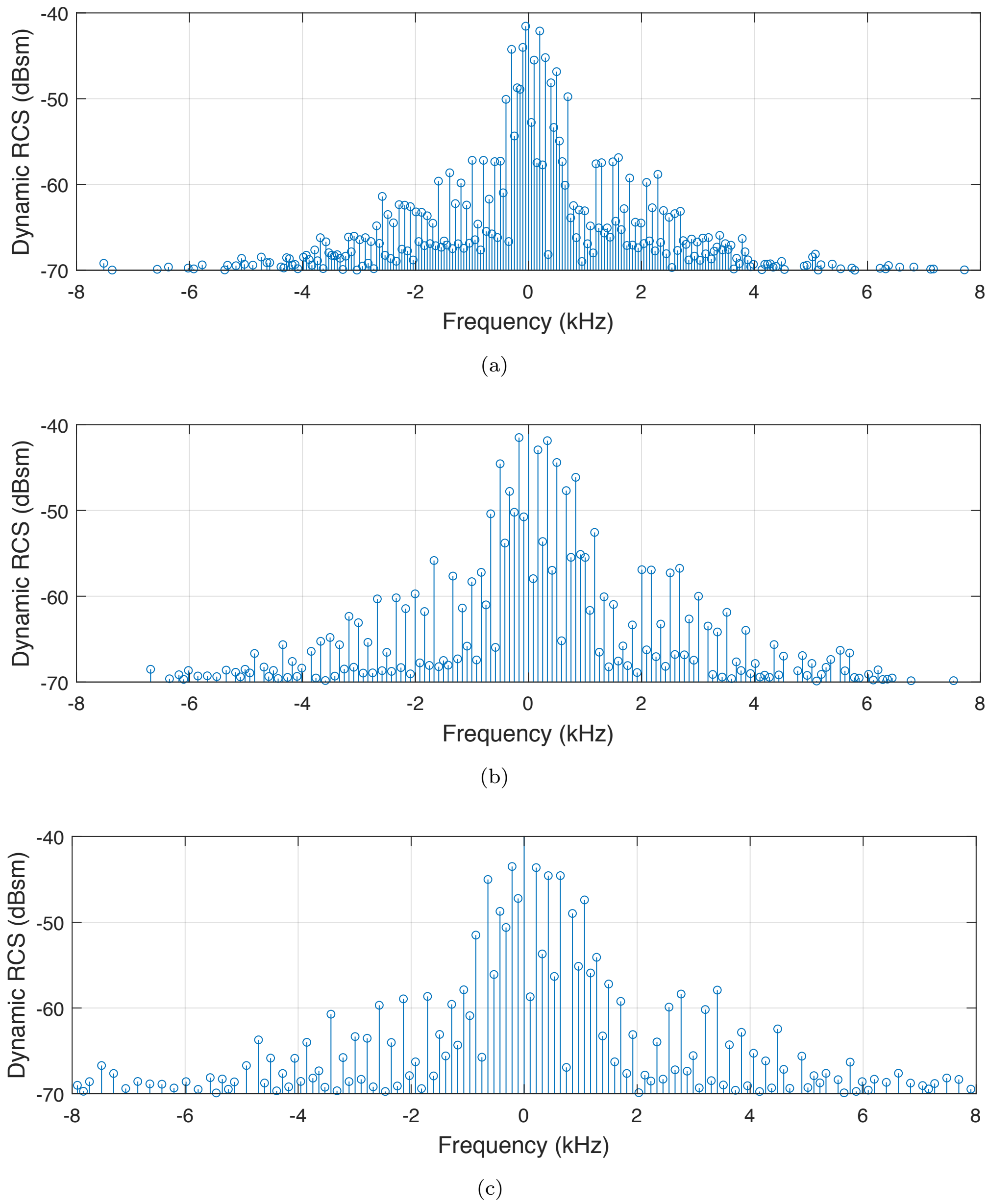

Figure 7.7: Re-plot the dynamic RCS results of one spinning propeller in edge-view configuration to just show the harmonic Doppler frequencies. The rotation rates are: (a) 3000 rpm; (b) 5000 rpm; and (c) 6500 rpm.

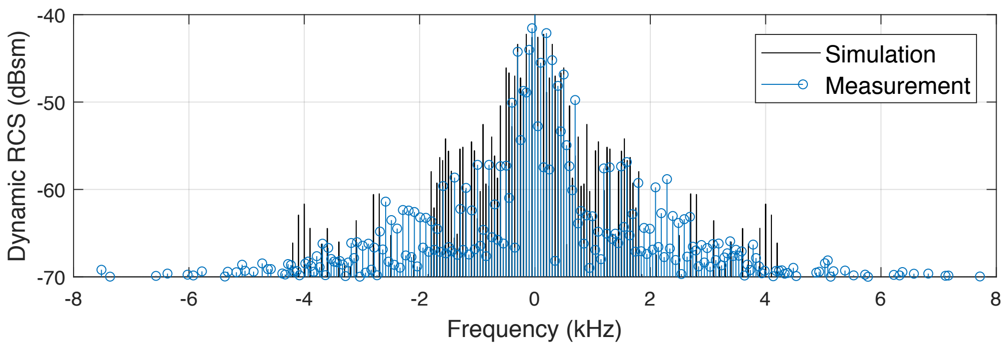

(a)

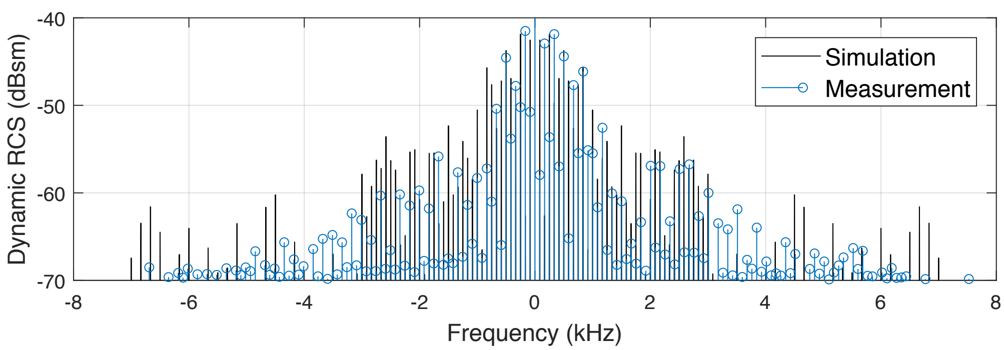

(b)

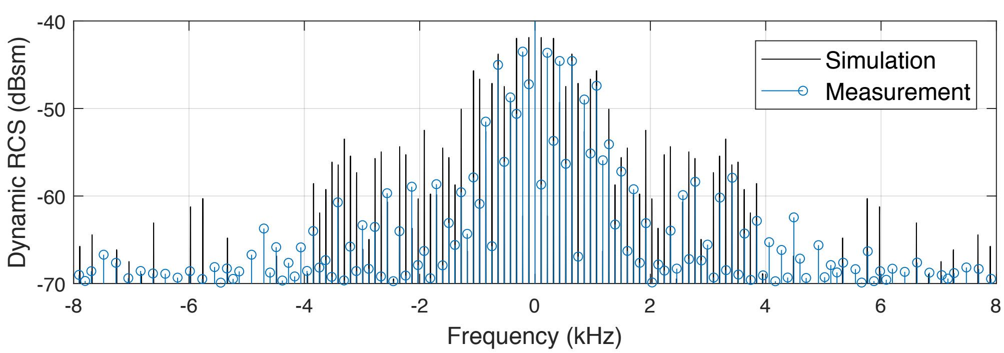

(c)

Figure 7.8: A comparison between simulated and measured dynamic RCS results of one propeller in edge-view configuration when the rotation rates are: (a) 3000 rpm; (b) 5000 rpm; and (c) 6500 rpm.

7.4 Chapter Conclusion

In this Chapter, the research on rotation-induced modulation, which makes a quadcopter an uncooperative target, is carried out by modeling a single propeller as a number of point scatterers. The modulated model for backscatter signals from a propeller rotating in an arbitrary direction is first given to show that the carrier signal is both frequency modulated by the rotation frequency and amplitude modulated by the reflection coefficient values of point scatterers. Then two special cases where propellers rotate in a vertical plane and a horizontal plane to resemble top-view and edge-view measurements are discussed with more details. The differences in bandwidth and magnitude of the received signals collected in top-view and edge-view measurements are explained with fully derived math models for the two cases.

In order to properly model the reflectivity of a propeller and analyze the micro-Doppler signature at different rotation rates and directions, 3-D SAR imaging technologies are leveraged to learn the distribution of point scatterers in a propeller. Six point scatterers are then selected to represent the edges of each blade and are assigned with random reflection coefficient values in Monte Carlo simulations. By correlations between the simulated backscatter signals from these twelve point scatterers and the measured receive signals at different rotation rates and in different directions, several sets of reflection coefficient values are found to model the propeller and reconstruct the measurement results to a maximum RMS error of 8 dB across all harmonic components in the very asymmetric upper and lower sidebands.

The work in Chapter 6 and Chapter 7 combined is a comprehensive characterization of all scattering properties of an uncooperative target from target level to the basic point scatterer level. The frequency response model is found to be very effective and efficient in all the analysis and modeling. The characterization methods applied and important conclusions arrived in these two chapters can be extended to the exploration of many other uncooperative targets.

Chapter 8

CONCLUSION AND FUTURE WORK

8.1 Conclusion

In this thesis, the concept of general modulated targets is proposed to encompass: (1) cooperative modulated target, (2) uncooperative modulated targets, and (3) unmodulated targets in radar and radar imaging applications. This general modulated target can change both the reflection coefficient values and the distribution of its point scatterers, that are either stationary or in motion, to modulate radar signals. On the other hand, the frequency response of a radar system is not only affected by the modulated targets, but also dependent on the location or motion of the transmitter and receiver. By accounting for both target modulation and radar physical configuration or motion, a general frequency response model is proposed based on each point scatterer in the target modulating the radar signal. Thus, backscatter signals from different modulated targets can be modeled and processed using the same framework.

Chapter 2 has a focus on how modulated targets change the frequency response of the system. We developed a first-of-a-kind low-cost X-band backscatter testbed and fabricated sensor tags used as cooperative targets to experiment the radar-target cooperation. The testbed system effectively shows a good agreement between measured and simulated free-space path loss at up to 4.1 m and demonstrates a BPSK backscatter modulation configuration at a rate of 10 Mbps. The work is published in [13].

Chapter 3 explores the impact of radar motion on system frequency response by fitting the model to SAR imaging applications. We present the SAR infrastructure to be used in the following chapters and propose an image reconstruction algorithm to reveal the profile of different targets. Chapter 4 presents a combined application of backscatter communication and SAR techniques to enable simultaneous radar imaging of reflective objects (unmodulated targets), sensor tag (cooperative target) localization, and backscatter-based data uplink (radar-target cooperation) from multiple sensor tags in a cluttered environment. To validate the model, SAR measurements are implemented at $10 - 13$ GHz with unmodulated targets and custom X-band sensor tags that monitor temperature changes and encode data with balanced orthogonal SAR code words in each packet. Resulting images show the existence of all targets with simultaneous tag-vs-clutter and tag-vs-tag discrimination. The point-spread functions (PSFs) of tags at ranges of 4.4 m and 4.7 m demonstrate a range resolution of 4.7 cm, a cross-range resolution of 9.1 cm, and a maximum localization error of 9 mm. The demodulated backscatter data shows that the sensor tags, while being imaged, simultaneously telemeter temperature changes and communicate with the radar. The work is published in [37, 93].

Chapter 5 models the 1-bounce multipath propagation effects in simultaneous radar imaging and localization application with first-order virtual point scatterers. These scatterers are either mirrored virtual scatterers of targets that are generated by large reflective objects or projected virtual scatterers of the mirrored scatterers leaving on the reflective surfaces. The expanded frequency response model, including the multipath components, is verified with SAR measurements in an environment that contains a large reflective plane. By correlating the SAR code words of cooperative targets with multiple SAR measurement samples, we are able to predict specular multipath ghosts that shall appear in the imaging results of all objects and localization results of a single or multiple tags. The predicted positions agree well with the reconstructed multipath ghosts to an error of 1.4 cm in localization and 3.6 cm in imaging scenario.

Chapter 6 comprehensively characterizes the reflectivity, static and dynamic radar cross sections, and the micro-Doppler signatures of a quadcopter UAV, which is illustrated as an uncooperative target, by using different K-band radar prototypes. The exploration of micro-Doppler signatures includes interference analysis between multiple spinning propellers and spectral analysis of Doppler frequencies induced by a single propeller operating at several given rotation rates. This wireless speed control is realized by a custom-designed flight controller unit that uses WiFi UDP connection. It is seen within a whole quadcopter, about 28% of the total backscatter signal power is due to the reflection of motors and carbon fiber propellers. And the radar cross section of this quadcopter is between -20 dBsm to -8 dBsm at K-band, whether it is in operation or not. The magnitude of Doppler frequencies and Doppler bandwidth differ, even for a fixed rotation rate, and depend on the propeller orientations relative to the radar unit.

In Chapter 7, the research on rotation-induced modulation, which makes a quadcopter an uncooperative target, is carried out by modeling a single propeller as a number of point scatterers. Differences in the magnitude of Doppler frequencies and Doppler bandwidths measured from different rotation orientations are explained by correlations between the simulated backscatter signals of point scatterers and the measured receive signals at different rotation rates and in different directions. With only twelve point scatterers modeling the propeller, several sets of reflection coefficient values are found to reconstruct the measurement results with a maximum RMS error of 8 dB across all harmonic components in the asymmetric upper and lower sidebands.

8.2 Future Work

8.2.1 Massive-MIMO Imaging of Modulated Targets

This thesis has explored the impact of bistatic configuration and radar motion on system frequency response, but does not account for the influences of sophisticated radar systems such as MIMO radars. The proposed frequency response model can be easily modified for MIMO radar applications with the index k being the position index of stationary TXs and RXs. In [49], we implemented a massive-MIMO imager prototype that consists of 24 simultaneous TXs and 72 simultaneous RXs operating in the K-band (17.5 GHz to 26.5 GHz). In the same work, we presented an orthogonal coded active illumination (OCAI) approach for massive-MIMO imagers which exploits balanced, binary orthogonal codes to separate TX signals at the receivers, while simultaneously mitigating RX self-jamming and DC offset impairments. The system was planned for personnel screening or weapon detection and has demonstrated images of human-scale mannequins. Two other directions of research based on the hardware and OCAI approach can be the real time imaging of modulated targets and the utilization of modulated targets (fiducials) which are arranged in a special geometry to calibrate each TX-RX channel.

8.2.2 Asymmetry in the Upper and Lower Doppler Sidebands

In Chapter 6, we have shown in Fig. 6.14 and 6.15 that the effective Doppler bandwidth of the same rotation is wider in edge-view configuration and narrower in top-view configuration; the dynamic RCS value, on the contrary, is higher in top-view configuration and lower in edge-view. However, one thing in common for the two configurations is that there is noticeable asymmetry between the upper and lower Doppler sidebands, especially in top-view cases. This could result from the IQ imbalance of the radar system, the anti-symmetric structure of the propeller, or even the polarimetry of antennas. To figure out the reason, more work needs to be done to correct the IQ imbalance of the system. And in the modeling of propeller, angle-variant complex reflection coefficient values can be used to better simulate the real propeller.

BIBLIOGRAPHY

[1] M. Skolnik, *Introduction to Radar Systems.* Electrical engineering series, McGraw-Hill, 2001.

[2] D. Pozar, *Microwave Engineering.* Wiley, 2012.

[3] E. Kampianakis, J. Kimionis, K. Tountas, C. Konstantopoulos, E. Koutroulis, and A. Bletsas, "Wireless environmental sensor networking with analog scatter radio and timer principles," *IEEE Sensors Journal*, vol. 14, pp. 3365–3376, Oct 2014.

[4] V. C. Chen, F. Li, S. . Ho, and H. Wechsler, "Micro-Doppler effect in radar: phenomenon, model, and simulation study," *IEEE Transactions on Aerospace and Electronic Systems*, vol. 42, pp. 2–21, Jan 2006.

[5] V. Chen, *The Micro-Doppler Effect in Radar.* Artech House Remote Sensing Library, Artech House, 2011.

[6] V. C. Chen, "Analysis of radar micro-Doppler with time-frequency transform," in *Proceedings of the Tenth IEEE Workshop on Statistical Signal and Array Processing (Cat. No.00TH8496)*, pp. 463–466, Aug 2000.

[7] J. A. Nanzer, "A review of microwave wireless techniques for human presence detection and classification," *IEEE Transactions on Microwave Theory and Techniques*, vol. 65, pp. 1780–1794, May 2017.

[8] T. Fan, C. Ma, Z. Gu, Q. Lv, J. Chen, D. Ye, J. Huangfu, Y. Sun, C. Li, and L. Ran, "Wireless hand gesture recognition based on continuous-wave Doppler radar sensors," *IEEE Transactions on Microwave Theory and Techniques*, vol. 64, pp. 4012–4020, Nov 2016.

[9] L. Ren, N. Tran, F. Foroughian, K. Naishadham, J. E. Piou, O. Kilic, and A. E. Fathy, "Short-time state-space method for micro-Doppler identification of walking subject using UWB impulse Doppler radar," *IEEE Transactions on Microwave Theory and Techniques*, vol. 66, pp. 3521–3534, July 2018.

[10] Y. Kim and T. Moon, "Human detection and activity classification based on micro-Doppler signatures using deep convolutional neural networks," *IEEE Geoscience and Remote Sensing Letters*, vol. 13, pp. 8–12, Jan 2016.

[11] Y. Kim and H. Ling, "Human activity classification based on micro-Doppler signatures using a support vector machine," *IEEE Transactions on Geoscience and Remote Sensing*, vol. 47, pp. 1328–1337, May 2009.

[12] Y. Ding and J. Tang, "Micro-Doppler trajectory estimation of pedestrians using a continuous-wave radar," *IEEE Transactions on Geoscience and Remote Sensing*, vol. 52, pp. 5807–5819, Sep. 2014.

[13] X. Fu, A. Sharma, E. Kampianakis, *et al.*, "A low cost 10.0-11.1 GHz X-band microwave backscatter communication testbed with integrated planar wideband antennas," in *Proc. IEEE International Conference on RFID*, (Orlando, USA), pp. 1–4, May 2016.

[14] H. Stockman, "Communication by means of reflected power," *Proceedings of the IRE*, vol. 36, pp. 0096–8390, Oct 1948.

[15] R. Want, "An introduction to RFID technology," *IEEE Pervasive Computing*, vol. 5, pp. 25–33, Jan 2006.

[16] L. Yang, A. Rida, R. Vyas, and M. M. Tentzeris, "RFID tag and RF structures on a paper substrate using inkjet-printing technology," *IEEE Transactions on Microwave Theory and Techniques*, vol. 55, pp. 2894–2901, Dec 2007.

[17] S. G. J. R. S. D. W. B. Kellogg, A. Parks, "Wi-Fi backscatter: Internet connectivity for RF-powered devices," *IEEE Transactions on Microwave Theory and Techniques*, vol. 44, pp. 607–618, August 2014.

[18] H. Ishizaki, H. Ikeda, Y. Yoshida, T. Maeda, T. Kuroda, and M. Mizuno, "A battery-less WiFi-BER modulated data transmitter with ambient radio-wave energy harvesting," in *2011 Symposium on VLSI Circuits - Digest of Technical Papers*, pp. 162–163, June 2011.

[19] J. F. Ensworth and M. S. Reynolds, "BLE-backscatter: Ultralow-power IoT nodes compatible with Bluetooth 4.0 low energy (BLE) smartphones and tablets," *IEEE Transactions on Microwave Theory and Techniques*, vol. 65, pp. 3360–3368, Sep. 2017.

[20] J. F. Ensworth and M. S. Reynolds, "Every smart phone is a backscatter reader: Modulated backscatter compatibility with bluetooth 4.0 low energy (BLE) devices," in *2015 IEEE International Conference on RFID (RFID)*, pp. 78–85, April 2015.

[21] A. Sharma, E. Kampianakis, J. Rosenthal, A. Pike, A. Dadkhah, and M. S. Reynolds, "Wideband UHF DQPSK backscatter communication in reverberant cavity animal cage environments," *IEEE Transactions on Antennas and Propagation*, pp. 1–1, 2019.

[22] J. Rosenthal, E. Kampianakis, A. Sharma, and M. S. Reynolds, "A 6.25 Mbps, 12.4 pJ/bit DQPSK backscatter wireless uplink for the NeuroDisc brain-computer interface," in *2018 IEEE Biomedical Circuits and Systems Conference (BioCAS)*, pp. 1–4, Oct 2018.

[23] A. P. Sample, D. J. Yeager, P. S. Powledge, and J. R. Smith, "Design of a passively-powered, programmable sensing platform for UHF RFID systems," in *2007 IEEE International Conference on RFID*, pp. 149–156, March 2007.

[24] Y. Zhao and J. R. Smith, "A battery-free RFID based indoor acoustic localization platform," in *2013 IEEE International Conference on RFID (RFID)*, pp. 110–117, April 2013.

[25] S. Naderiparizi, A. N. Parks, Z. Kapetanovic, B. Ransford, and J. R. Smith, "Wispcam: A battery-free RFID camera," in *2015 IEEE International Conference on RFID (RFID)*, pp. 166–173, April 2015.

[26] I. i. Veen, Q. Liu, P. Pawelczak, A. Parks, and J. R. Smith, "BLISP: Enhancing backscatter radio with active radio for computational RFIDs," in *2016 IEEE International Conference on RFID (RFID)*, pp. 1–4, May 2016.

[27] M. Tabesh, N. Dolatsha, A. Arbabian, and A. Niknejad, "A power-harvesting pad-less millimeter-sized radio," *IEEE Journal of Solid-State Circuits*, vol. 50, pp. 962–977, Mar 2015.

[28] J. Griffin and G. Durgin, "Multipath fading measurements at 5.8 GHz for backscatter tags with multiple antennas," *IEEE Transactions on Antennas and Propagation*, vol. 58, pp. 3693–3700, Aug 2010.

[29] C. Carlowitz, M. Vossiek, A. Strobel, and F. Ellinger, "Precise ranging and simultaneous high speed data transfer using mm-wave regenerative active backscatter tags," *2013 IEEE International Conference on RFID*, pp. 253–260, Apr 2013.

[30] W. Stein, A. Aleksieieva, S. Roehr, and M. Vossiek, "Phase modulated 61 GHz backscatter transponder for FMCW radar-based ranging," *2014 German Microwave Conference (GeMIC)*, pp. 1–4, Mar 2014.

[31] C. Schmid, R. Feger, and A. Stelzer, "Millimeter-wave phase-modulated backscatter transponder for FMCW radar applications," *2011 IEEE MTT-S International Microwave Symposium*, pp. 1–4, Jun 2011.

[32] P. V. Nikitin, K. V. S. Rao, and R. D. Martinez, "Differential RCS of RFID tag," *Electronics Letters*, vol. 43, pp. 431–432, April 2007.

[33] J. Griffin and G. Durgin, "Complete link budgets for backscatter-radio and RFID systems," *IEEE Antennas and Propagation Magazine*, vol. 51, pp. 11–25, Apr 2009.

[34] C. Balanis, *Antenna Theory: Analysis and Design*. Wiley, 2015.

[35] K. Kiminami, A. Hirata, and T. Shiozawa, "Double-sided printed bow-tie antenna for UWB communications," *IEEE Antennas and Wireless Propagation Letters*, vol. 3, pp. 152–153, Dec 2004.

[36] Z. Tao, "Broadband transition design from microstrip to CPW," *IEEE Microwave and Wireless Components Letters*, vol. 25, pp. 712–714, Nov 2015.

[37] X. Fu, A. Pedross-Engel, D. Arnitz, C. M. Watts, A. Sharma, and M. S. Reynolds, "Simultaneous imaging, sensor tag localization, and backscatter uplink via synthetic aperture radar," *IEEE Transactions on Microwave Theory and Techniques*, vol. 66, pp. 1570–1578, March 2018.

[38] I. G. Cumming and F. H. Wong, *Digital Processing of Synthetic Aperture Radar Data*. Norwood, MA: Artech House, 2005.

[39] C. WILEY, "Synthetic aperture radars : A paradigm for technology evolution," *IEEE Transactions on Aerospace and Electronic Systems*, vol. 21, pp. 440–443, 1985.

[40] A. Moreira, P. Prats-Iraola, M. Younis, G. Krieger, I. Hajnsek, and K. P. Papathanassiou, "A tutorial on synthetic aperture radar," *IEEE Geoscience and Remote Sensing Magazine*, vol. 1, pp. 6–43, March 2013.

[41] A. Reigber, R. Scheiber, M. Jager, P. Prats-Iraola, I. Hajnsek, T. Jagdhuber, K. P. Papathanassiou, M. Nannini, E. Aguilera, S. Baumgartner, R. Horn, A. Nottensteiner, and A. Moreira, "Very-high-resolution airborne synthetic aperture radar imaging: Signal processing and applications," *Proceedings of the IEEE*, vol. 101, pp. 759–783, March 2013.

[42] R. Horn, “The DLR airborne SAR project E-SAR,” in *IGARSS ’96. 1996 International Geoscience and Remote Sensing Symposium*, vol. 3, pp. 1624–1628 vol.3, May 1996.

[43] A. L. Gray and P. J. Farris-Manning, “Repeat-pass interferometry with airborne synthetic aperture radar,” *IEEE Transactions on Geoscience and Remote Sensing*, vol. 31, pp. 180–191, Jan 1993.

[44] H. A. Zebker, S. N. Madsen, J. Martin, K. B. Wheeler, T. Miller, Y. Lou, G. Alberti, S. Vetrella, and A. Cucci, “The TOPSAR interferometric radar topographic mapping instrument,” *IEEE Transactions on Geoscience and Remote Sensing*, vol. 30, pp. 933–940, Sep. 1992.

[45] H. Breit, T. Fritz, U. Balss, M. Lachaise, A. Niedermeier, and M. Vonavka, “TerraSAR-X SAR processing and products,” *IEEE Transactions on Geoscience and Remote Sensing*, vol. 48, pp. 727–740, Feb 2010.

[46] G. Krieger, A. Moreira, H. Fiedler, I. Hajnsek, M. Werner, M. Younis, and M. Zink, “TanDEM-X: A satellite formation for high-resolution SAR interferometry,” *IEEE Transactions on Geoscience and Remote Sensing*, vol. 45, pp. 3317–3341, Nov 2007.

[47] D. Cerutti-Maori, I. Sikaneta, and C. H. Gierull, “Optimum SAR/GMTI processing and its application to the radar satellite RADARSAT-2 for traffic monitoring,” *IEEE Transactions on Geoscience and Remote Sensing*, vol. 50, pp. 3868–3881, Oct 2012.

[48] S. Hantscher, B. Schlenther, M. Hagelen, S. A. Lang, H. Essen, A. Tessmann, A. Hulsmann, A. Leuther, and M. Schlechtweg, “Security pre-screening of moving persons using a rotating multichannel W-band radar,” *IEEE Transactions on Microwave Theory and Techniques*, vol. 60, pp. 870–880, March 2012.

[49] A. Pedross-Engel, D. Arnitz, J. N. Gollub, O. Yurduseven, K. P. Trofatter, M. F. Imani, T. Sleasman, M. Boyarsky, X. Fu, D. L. Marks, D. R. Smith, and M. S. Reynolds, “Orthogonal coded active illumination for millimeter wave, massive-MIMO computational imaging with metasurface antennas,” *IEEE Transactions on Computational Imaging*, vol. 4, pp. 184–193, June 2018.

[50] S. Bertl and J. Detlefsen, “Effects of a reflecting background on the results of active MMW SAR imaging of concealed objects,” *IEEE Transactions on Geoscience and Remote Sensing*, vol. 49, pp. 3745–3752, Oct 2011.

[51] D. M. Sheen, D. L. McMakin, and T. E. Hall, “Three-dimensional millimeter-wave imaging for concealed weapon detection,” *IEEE Transactions on Microwave Theory and Techniques*, vol. 49, pp. 1581–1592, Sep. 2001.

[52] F. Ali, G. Bauer, and M. Vossiek, “A rotating synthetic aperture radar imaging concept for robot navigation,” *IEEE Transactions on Microwave Theory and Techniques*, vol. 62, pp. 1545–1553, July 2014.

[53] C. M. Watts, P. Lancaster, A. Pedross-Engel, J. R. Smith, and M. S. Reynolds, “2D and 3D millimeter-wave synthetic aperture radar imaging on a PR2 platform,” in *2016 IEEE/RSJ International Conference on Intelligent Robots and Systems (IROS)*, pp. 4304–4310, Oct 2016.

[54] S. Park, Y. Kim, E. T. Matson, and A. H. Smith, “Accessible synthetic aperture radar system for autonomous vehicle sensing,” in *2016 IEEE Sensors Applications Symposium (SAS)*, pp. 1–6, April 2016.

[55] D. Clarke, D. Andre, and F. Zhang, "Synthetic aperture radar for lane boundary detection in driver assistance systems," in *2016 IEEE International Conference on Multisensor Fusion and Integration for Intelligent Systems (MFI)*, pp. 238–243, Sep. 2016.

[56] M. Younis, C. Fischer, and W. Wiesbeck, "Digital beamforming in SAR systems," *IEEE Transactions on Geoscience and Remote Sensing*, vol. 41, pp. 1735–1739, July 2003.

[57] G. Krieger, "MIMO-SAR: Opportunities and pitfalls," *IEEE Transactions on Geoscience and Remote Sensing*, vol. 52, pp. 2628–2645, May 2014.

[58] R. Miesen, F. Kirsch, and M. Vossiek, "UHF RFID localization based on synthetic apertures," *IEEE Transactions on Automation Science and Engineering*, vol. 10, pp. 807–815, July 2013.

[59] L. Qiu, Z. Huang, N. Wirström, and T. Voigt, "3DinSAR: Object 3D localization for indoor RFID applications," in *Proc. IEEE International Conference on RFID*, (Orlando, USA), pp. 1–8, May 2016.

[60] J. M. Lopez-Sanchez and J. Fortuny-Guasch, "3-D radar imaging using range migration techniques," *IEEE Transactions on Antennas and Propagation*, vol. 48, pp. 728–737, May 2000.

[61] A. Budillon, A. Evangelista, and G. Schirinzi, "Three-dimensional SAR focusing from multipass signals using compressive sampling," *IEEE Transactions on Geoscience and Remote Sensing*, vol. 49, pp. 488–499, Jan 2011.

[62] A. Pedross-Engel, C. M. Watts, D. R. Smith, and M. S. Reynolds, "Enhanced resolution stripmap mode using dynamic metasurface antennas," *IEEE Transactions on Geoscience and Remote Sensing*, vol. 55, pp. 3764–3772, July 2017.

[63] S. Devadithya, A. Pedross-Engel, C. M. Watts, N. I. Landy, T. Driscoll, and M. S. Reynolds, "GPU-accelerated enhanced resolution 3-D sar imaging with dynamic metamaterial antennas," *IEEE Transactions on Microwave Theory and Techniques*, vol. 65, pp. 5096–5103, Dec 2017.

[64] K. Yedavalli and B. Krishnamachari, "Sequence-based localization in wireless sensor networks," *IEEE Transactions on Mobile Computing*, vol. 7, pp. 81–94, Jan 2008.

[65] S. H. Fang and T. N. Lin, "A dynamic system approach for radio location fingerprinting in wireless local area networks," *IEEE Transactions on Communications*, vol. 58, pp. 1020–1025, April 2010.

[66] J. Shirahama and T. Ohtsuki, "RSS-based localization in environments with different path loss exponent for each link," in *VTC Spring 2008 - IEEE Vehicular Technology Conference*, pp. 1509–1513, May 2008.

[67] P. V. Nikitin, R. Martinez, S. Ramamurthy, H. Leland, G. Spiess, and K. V. S. Rao, "Phase based spatial identification of UHF RFID tags," in *2010 IEEE International Conference on RFID*, pp. 102–109, April 2010.

[68] R. Klukas and M. Fattouche, "Line-of-sight angle of arrival estimation in the outdoor multipath environment," *IEEE Transactions on Vehicular Technology*, vol. 47, pp. 342–351, Feb 1998.

[69] Y. T. Chan and K. C. Ho, "A simple and efficient estimator for hyperbolic location," *IEEE Transactions on Signal Processing*, vol. 42, pp. 1905–1915, Aug 1994.

[70] L. Cong and W. Zhuang, "Hybrid TDOA/AOA mobile user location for wideband CDMA cellular systems," *IEEE Transactions on Wireless Communications*, vol. 1, pp. 439–447, Jul 2002.

[71] A. Sharma, A. Pedross-Engel, D. Arnitz, C. M. Watts, D. R. Smith, and M. S. Reynolds, "A K-band backscatter fiducial for continuous calibration in coherent millimeter-wave imaging," *IEEE Transactions on Microwave Theory and Techniques*, vol. PP, no. 99, pp. 1–8, 2017.

[72] P. Setlur, G. Alli, and L. Nuzzo, "Multipath exploitation in through-wall radar imaging via point spread functions," *IEEE Transactions on Image Processing*, vol. 22, pp. 4571–4586, Dec 2013.

[73] P. Setlur, M. Amin, and F. Ahmad, "Multipath model and exploitation in through-the-wall and urban radar sensing," *IEEE Transactions on Geoscience and Remote Sensing*, vol. 49, pp. 4021–4034, Oct 2011.

[74] P. Setlur, T. Negishi, N. Devroye, and D. Erricolo, "Multipath exploitation in Non-LOS urban synthetic aperture radar," *IEEE Journal of Selected Topics in Signal Processing*, vol. 8, pp. 137–152, Feb 2014.

[75] T. Dogaru and C. Le, "SAR images of rooms and buildings based on FDTD computer models," *IEEE Transactions on Geoscience and Remote Sensing*, vol. 47, pp. 1388–1401, May 2009.

[76] J. Liu, L. Kong, X. Yang, and Q. H. Liu, "First-order multipath ghosts' characteristics and suppression in MIMO through-wall imaging," *IEEE Geoscience and Remote Sensing Letters*, vol. 13, pp. 1315–1319, Sep. 2016.

[77] S. Guo, G. Cui, L. Kong, Y. Song, and X. Yang, "Multipath analysis and exploitation for MIMO through-the-wall imaging radar," *IEEE Journal of Selected Topics in Applied Earth Observations and Remote Sensing*, vol. 11, pp. 3721–3731, Oct 2018.

[78] M. Wang, G. Cui, L. Kong, and X. Yang, "First-order rear-wall multipath positioning and suppression for through-wall imaging radar," *IEEE Sensors Journal*, vol. 18, pp. 8261–8274, Oct 2018.

[79] M. Leigsnering, F. Ahmad, M. G. Amin, and A. M. Zoubir, "Compressive sensing-based multipath exploitation for stationary and moving indoor target localization," *IEEE Journal of Selected Topics in Signal Processing*, vol. 9, pp. 1469–1483, Dec 2015.

[80] M. Leigsnering, F. Ahmad, M. Amin, and A. Zoubir, "Multipath exploitation in through-the-wall radar imaging using sparse reconstruction," *IEEE Transactions on Aerospace and Electronic Systems*, vol. 50, pp. 920–939, April 2014.

[81] G. Gennarelli, G. Vivone, P. Braca, F. Soldovieri, and M. G. Amin, "Comparative analysis of two approaches for multipath ghost suppression in radar imaging," *IEEE Geoscience and Remote Sensing Letters*, vol. 13, pp. 1226–1230, Sep. 2016.

[82] H. Sedjelmaci, S. M. Senouci, and N. Ansari, "Intrusion detection and ejection framework against lethal attacks in UAV-aided networks: A Bayesian game-theoretic methodology," *IEEE Transactions on Intelligent Transportation Systems*, vol. 18, pp. 1143–1153, May 2017.

[83] C. Zhao, J. He, and J. Chen, "Resilient consensus with mobile detectors against malicious attacks," *IEEE Transactions on Signal and Information Processing over Networks*, vol. 4, pp. 60–69, March 2018.

[84] C. J. Li and H. Ling, "An investigation on the radar signatures of small consumer drones," *IEEE Antennas and Wireless Propagation Letters*, vol. 16, pp. 649–652, 2017.

[85] W. Lee and K. Song, "Enhanced ISAR imaging for surveillance of multiple drones in urban areas," in *2018 International Conference on Radar (RADAR)*, pp. 1–4, Aug 2018.

[86] P. Tait, "Target classification for air defence radars," in *2006 IET Seminar on High Resolution Imaging and Target Classification*, pp. 3–16, Nov 2006.

[87] A. K. Singh and Y. Kim, "Automatic measurement of blade length and rotation rate of drone using W-band micro-Doppler radar," *IEEE Sensors Journal*, vol. 18, pp. 1895–1902, March 2018.

[88] P. Molchanov, K. Egiazarian, J. Astola, R. I. A. Harmanny, and J. J. M. de Wit, "Classification of small UAVs and birds by micro-Doppler signatures," in *2013 European Radar Conference*, pp. 172–175, Oct 2013.

[89] P. Zhang, L. Yang, G. Chen, and G. Li, "Classification of drones based on micro-Doppler signatures with dual-band radar sensors," in *2017 Progress in Electromagnetics Research Symposium - Fall (PIERS - FALL)*, pp. 638–643, Nov 2017.

[90] B. K. Kim, H. Kang, and S. Park, "Experimental analysis of small drone polarimetry based on Micro-Doppler signature," *IEEE Geoscience and Remote Sensing Letters*, vol. 14, pp. 1670–1674, Oct 2017.

[91] M. Ritchie, F. Fioranelli, H. Borrion, and H. Griffiths, "Multistatic micro-Doppler radar feature extraction for classification of unloaded/loaded micro-drones," *IET Radar, Sonar Navigation*, vol. 11, no. 1, pp. 116–124, 2017.

[92] J. Proakis and M. Salehi, *Fundamentals of Communication Systems.* Pearson Education, 2013.

[93] X. Fu, A. Pedross-Engel, D. Arnitz, and M. S. Reynolds, "Simultaneous sensor localization via synthetic aperture radar (SAR) imaging," in *Proc. IEEE International Conference on Sensors*, (Orlando, USA), pp. 1–3, Oct 2016.